Investigation of Transition Metal Alkyl, Allyl, Hydride, and Borohydride Complexes as Potential Precursors for Atomic Layer Deposition

By

Declan M. DeJordy, H.B.Sc.

A Thesis Submitted to the School of Graduate Studies in Partial Fulfillment of the Requirements for the Degree Master of Science

McMaster University

MASTER OF SCIENCE (2020) McMaster University

(Department of Chemistry and Chemical Biology) Hamilton, Ontario

TITLE: Investigation of Transition Metal Alkyl, Allyl, Hydride, and Borohydride Complexes as Potential Precursors for Atomic Layer Deposition

AUTHOR: Declan M. DeJordy

SUPERVISOR: Prof. David J. H. Emslie

NUMBER OF PAGES: xxii, 131

Abstract

Atomic layer deposition (ALD) is a vapour phase (ultra-)thin film growth technique that yields highly conformal and uniform films and offers exceptional control over film thickness. Given the continual trend of miniaturization in microelectronics, ALD is required to support the precision demands of next-generation devices.[1]

Deposition is achieved through repeated surface-based reactions between a volatile precursor molecule and co-reactant, which are delivered sequentially in the gas phase. Careful design of these reactions ensures that only volatile by-products are formed, which are then removed during an inert gas purge step, which follows each precursor and co-reactant pulse, along with any excess precursor or co-reactant.[2] The film thickness therefore depends only on the number of precursor/purge/co-reactant/purge cycles.[3]

The essential physical and chemical properties of metal ALD precursors are: (1) volatility, so that the compound may be delivered at a temperature below that of the substrate, (2a) thermal stability on a long timescale (weeks to months), to prevent decomposition at the temperature of the delivery bubbler, (2b) thermal stability on a short timescale (seconds or minutes), to prevent parasitic CVD at the temperature of the substrate, and (3) reactivity, which occurs rapidly at the substrate temperature and leads to the desired material and only volatile by-products.[2] Precursor selection typically requires a compromise of volatility, thermal stability, and reactivity.

The bulk of this work focuses on the syntheses of various transition metal complexes bearing alkyl, allyl, hydride, and borohydride ligands, as well as the evaluation

of these complexes as potential new chemical precursors for the ALD of mainly electropositive transition metals.

The compounds bearing alkyl ligands which were investigated are $[Cr(CH_2SiMe_3)_4]$ **(1)**, $[Cr(CH_2CMe_3)_4]$ **(2)**, $[V(CH_2SiMe_3)_4]$ **(3)**, $[W_2(CH_2SiMe_3)_6]$ **(5)**, $[Mo_2(CH_2SiMe_3)_6]$ **(6)**, and $[Cr(dmpe)_2(Me)_2]$ **(7)**. Syntheses for complexes **1**–**3** and **5**–**7** have previously been published, but this work will introduce alternate or slightly modified procedures, as well as the description of the solid-state structure of **3**. Each complex was shown to sublime without decomposition. Thermal stability studies revealed that the complexes lacked the thermal stability on a long timescale to be effective as ALD precursors in a typical ALD reactor, assuming that a delivery temperature 40 °C higher than the sublimation temperature at 5 mTorr will be required. The vanadium containing complex $[\{V(CH_2SiMe_3)_3O\}_2Mg(dme)_2]$ **(4)** was isolated as an intermediate during the synthesis of **3** and structurally characterized by single crystal X-ray diffraction.

Additionally, homoleptic allyl complexes $[M\{1,3\text{-bis(trimethylsilyl)allyl}\}_2]$ M = Ni **(8)**, Cr **(9)**, Co **(10)** were investigated. The solution state reactivity of each complex towards the potential co-reactants $AlEt_3$, BEt_3, and $PhSiH_3$ was examined. Promising reactivity was observed between complex **8** and $AlEt_3$, as well as complex **10** and $AlEt_3$ or complex **10** and $PhSiH_3$. However, subsequent study of the thermal stability of each complex revealed decomposition of each complex 40 °C above the sublimation temperature. Nickel complex **8** thermally decomposed to yield nickel metal (as analyzed by powder X-ray diffraction), and as such is suggested as a candidate for nickel metal

chemical vapour deposition, contingent upon characterization of the minor unidentified reflection observed during powder X-ray diffraction.

Borohydride complex $[(dmpe)_2Mn(\mu\text{-}H)_2BH_2]$ **(11)** was obtained through the reaction of $[(dmpe)MnH(C_2H_4)]$ with $BH_3(NMe_3)$. The complex sublimes without decomposition at 80 °C, but was shown to undergo thermal decomposition after being heated to 120 °C, lacking the desired thermal stability for ALD use. Complexes $[\{(dmpe)_2MnH\}_2(\mu\text{-dmpe})]$ **(12)** and $[(dmpe)_2MnH(\kappa^1\text{-dmpe})]$ **(13)** were identified in crude reaction mixtures during the synthesis of **11**, and were subsequently synthesized independently. The synthetic scheme for **13** was extended to $[(dmpe)_2MnH(PMe_3)]$ **(14)**, and both complexes were crystallographically characterized. Compounds **12**–**14** exist in solution as isomers with *cis*- or *trans*- disposed hydride and $\kappa^1\text{-}PR_3$ ligands. For each complex, isomerization from *trans*- to *cis*- was shown to be photochemically induced, while the reverse isomerization will take place either slowly (days) in the absence of light, or quickly (hours) through heating. Manganese compound **14** was shown to be volatile at 60 °C and to only undergo moderate decomposition after being heated to 100 °C.

Acknowledgements

First and foremost, I must thank my supervisor Professor David J. H. Emslie for sharing with me his knowledge, support, and the occasional IPA. The excitement you have for each and every one of our projects is wonderful. It was a pleasure working for you, and with you.

To all my lab mates whom I can now call friends: Dr. Jeffrey Price, Aathith (Sonny) Vasanthakumar, Dr. Kevin (Ya-Dong) Yu, Dr. Blossom Yan, Katarina Paskaruk, Majeda Al Hareri, Novan Gray, Kasuni Wedisinghe, Nick Hoffman, and Maia Murphy, thank you all for your willingness to help with anything both inside and outside of the lab. It was a ton of fun working with you all, we have such a unique and diverse group which meshes so well. I will miss playing Sporkle over lunch, but I will not miss overseeing typing (or geography).

Dr. Kylie Luska, it was a blast sharing in the championship run with you. Thank you for all of your excellent advice and support.

Dr. James Britten, thank you for always being available to lend help and share your knowledge along the way. Vicky Jarvis, thanks for always letting me throw on a sample ahead of you and for keeping me optimistic afterwards when things did not work out as I had hoped.

Mom and Dad thank you for being there every step of the way and shaping me into the person I am today. Lindsay, you have listened to more complaints than I hope to ever subject you to again, thank you for your patience.

"There is no point in using the word 'impossible' to describe something that has clearly happened."

-Douglas Adams

Table of Contents

List of Figures

List of Schemes

List of Tables

Synthesized Complexes

Chapter 2

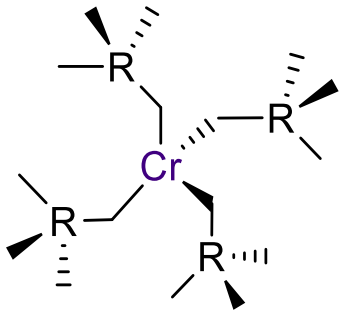

R = Si (1)
R = C (2)

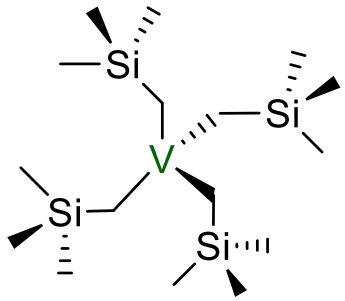

(3)

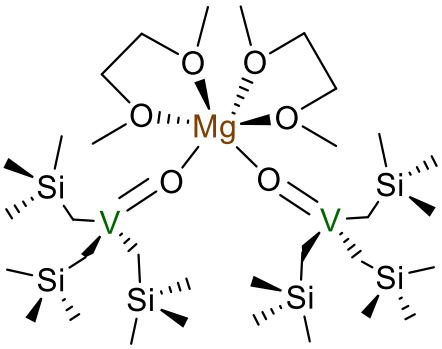

(4)

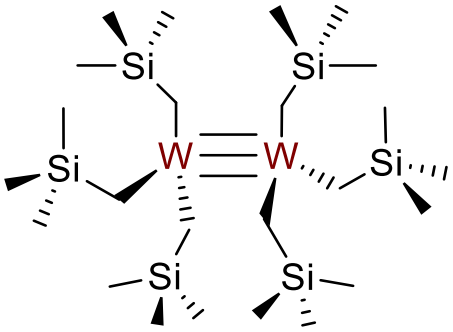

(5)

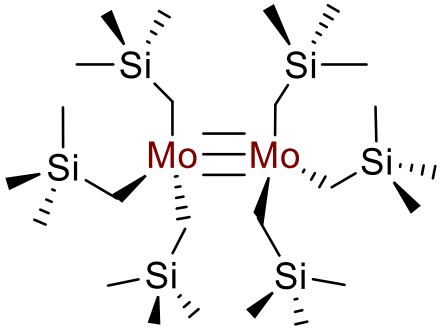

(6)

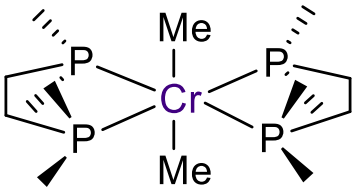

(7)

Chapter 3

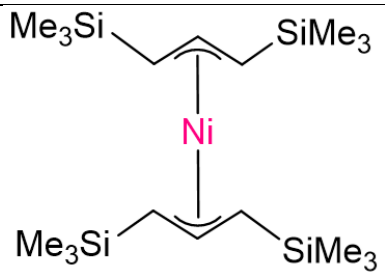

(8)

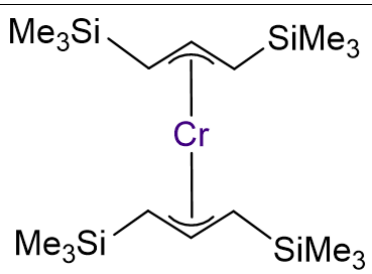

(9)

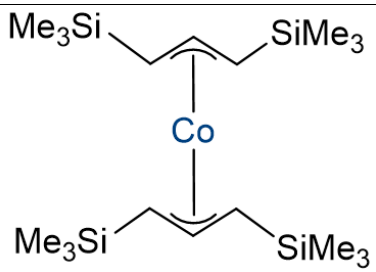

(10)

Chapter 4

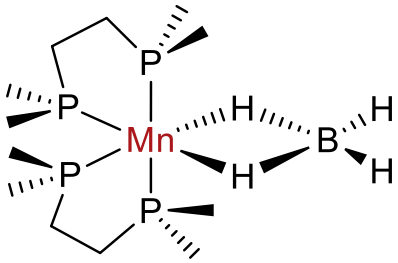

(11)

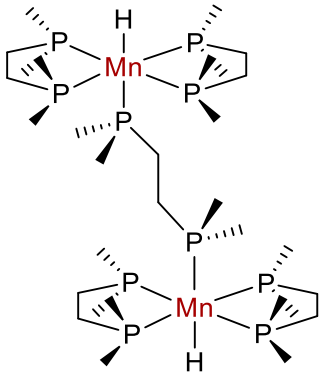

(12)

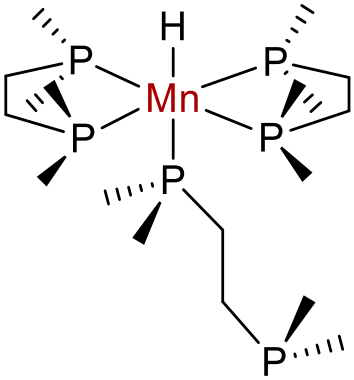

(13)

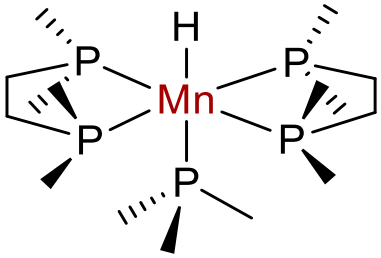

(14)

List of Abbreviations, Acronyms, and Symbols

General (Acronyms)

BEOL – Back end of line

CMOS – Complementary metal-oxide semiconductor

DRAM – Dynamic random-access memory

ITO – Indium tin oxide

IRDS – International Roadmap for Devices and Systems

MOSFET – Metal-oxide-semiconductor field-effect transistor

T – Temperature

TCF – Transparent conducting films

UHV – Ultra high vacuum

General (symbols)

μ_n – Bridging ligand

κ^n – Denticity

η^n – Hapticity

% – Percent

Units

Å – Angstrom

Atm – Standard atmosphere

°C – Degrees Celsius

d – Days

g – Gram

h – Hour

Hz (MHz) – Hertz (megahertz)

J (kJ) – Joule (kilojoule)

L (mL) – Litre (millilitre)

m (nm, μm) – Metre (nanometre, micrometre)

mol (mmol) – Mole (millimole)

M – Molarity

Ppm – Parts per million

Torr (mTorr) – Torr (millitorr)

V (kV) – Volts (kilovolts)

Equipment and Techniques (abbreviations, and acronyms)

ALD – Atomic layer deposition

Anal. – Combustion elemental analysis results

AFM – Atomic force microscopy

AES – Auger electron spectroscopy

CVD – Chemical vapour deposition

DFT – Density functional theory

EPR – Electron paramagnetic resonance (spectroscopy)

FT-IR – Fourier-transform infrared (spectroscopy)

IR – Infrared (spectroscopy)

NMR – Nuclear magnetic resonance (spectroscopy)

PEALD – Plasma enhanced atomic layer deposition

PVD – Physical vapour deposition

PXRD – Powder X-ray diffraction

QMS – Quadrupole mass spectrometry

QCM – Quartz crystal microbalance

SCXRD – Single crystal X-ray diffraction

TGA – Thermogravimetric analysis

XPS – X-ray photoelectron spectroscopy

Chemical species (compounds, ligands, and substituents)

acac – Acetylacetonate

amd – Amidinate

Bu – Butyl

^{s}Bu – *sec*-Butyl

^{n}Bu – *n*-Butyl (*n* = normal)

^{t}Bu – *tert*-Butyl

Cp – Cyclopentadienyl

^{Et}Cp – C_5H_4Et

^{Me}Cp – C_5H_4Me

dpm (a.k.a tmhd) – 2,2,6,6-tetramethyl-3,5-heptanedionate

Et – Ethyl

fod – 6,6,7,7,8,8,8-heptafluoro-2,2-dimethyl-3,5-octanedionate

hfac – Hexafluoroacetylacetonate

Im – Imidazolyl

Me – Methyl

Ph – Phenyl

Pr – Propyl

^{i}Pr – *iso*-propyl

^{n}Pr – *n*-propyl (*n* = normal)

Pyr – Pyridinyl

R – General alkyl or silyl substituent

THF – Tetrahydrofuran

tmhd (a.k.a dpm) – 2,2,6,6-tetramethyl-3,5-heptanedionate

Declaration of Academic Achievement

Dr. James Britten (of the McMaster Analytical X-ray Diffraction Facility) was responsible for the XRD refinement and structure solution for [V(CH_2SiMe_3)$_4$] **(3)** and [(dmpe)$_2$MnH(κ^1-dmpe)] **(13)**. Dr. Jeffrey S. Price, as a Ph.D. student, was responsible for the synthesis of the dialkyl magnesium Grignard reagent, Mg(CH_2CMe_3)$_2$, as well as the initial synthesis and characterization of [(dmpe)$_2$Mn(μ-H)$_2$BH$_2$] **(11)**, [{(dmpe)$_2$MnH}$_2$(μ-dmpe)] **(12)**, and [(dmpe)$_2$MnH(κ^1-dmpe)] **(13)**, excluding the X-ray crystal structure of **13**. Declan M. DeJordy was responsible for the improved and thereafter reported syntheses of complexes **11**, **12**, and **13**. Dr. Jeffrey S. Price performed the *trans*- to *cis*- isomerization monitoring experiments for [(dmpe)$_2$MnH(κ^1-dmpe)] **(13)**, as described in Chapter 4. All other results were obtained by Declan M. DeJordy.

Chapter 1 – Introduction

1.1 Miniaturization of Microelectronic Devices

The transistor was developed in 1947 and remains the most fundamental component of modern electronics. In 1965, Gordon E. Moore, the co-founder of Intel Corporation, postulated that the number of transistors on an integrated circuit would double every 18–24 months.[4] This idea, which came to be known as "Moore's Law", has tracked the exponential growth of transistor density in microelectronic design and fabrication. Devices continue to evolve and become smaller, faster, and more power efficient. As of 2018, the International Roadmap for Devices and Systems (IRDS) defines the 7 nm process as the metal-oxide-semiconductor field-effect transistor (MOSFET) technology node, which followed the 10 nm node in 2016.[5] Considering silicon's atomic size of approximately 0.2 nm, a space containing a mere 35 Si atoms exists between the source and drain.[6] 5 nm nodes, which were once assumed by experts to be the end of Moore's law (since transistors smaller than 7 nm will experience quantum tunnelling through the gate oxide layer), are planned to begin mass production in 2020.[7] Industry leaders have announced plans to put 3 nm semiconductor nodes into commercial production as soon as 2021.[8]

The continuation of this trend presents enormous challenges. The growth of thin films with absolute thickness control in very high aspect ratio features is limited by traditional deposition methods. To support further device miniaturization, more 3-dimensional device architectures are likely to be required, therefore new deposition processes and chemical precursors must be developed.

1.2 Materials Containing Metal Thin Films

A thin film is a layer of material ranging from a monolayer to several micrometers in thickness. Metal thin films are ubiquitous in nanotechnology, finding usage in numerous magnetic, catalytic, optical, and electrical applications. The most established application of thin films is in microelectronics (microprocessors, memory devices) made from semiconductor materials.[2] Metallic films are used in microelectronic devices as conductors (transistor gates, electrodes, interconnects) and seed/capping layers, while high-κ dielectrics and diffusion barriers are typically made up of metal oxides and nitrides. With the continual down-scaling of semiconductor devices, the need for nanotechnology has increased exponentially.[9] In nanoscale devices, each layer of material is required to be as thin and as perfect as is possible.

At their simplest, semiconducting devices work as either amplifiers or switches. Modern processors utilize billions of transistors as electrically driven switches for parallel computation. MOSFET's are the most widely used semiconductor device worldwide (accounting for 99.9% of all transistors) as well as the most widely manufactured device in history.[10] The MOSFET is manufactured upon a silicon substrate, where conductivity can be tuned via the controlled addition of impurity atoms which support the presence of charged particles.[11] These impurities, known as dopants, can be n-type (negative, electrons) or p-type (positive, holes). Manufacturing of discrete n-type and p-type regions isolates domains of negative and positive charges through the formation of barriers that prevent the flow of current.[11] The gate is made of highly conductive material, which is separated from the semiconductor by a dielectric.[11] When the appropriate voltage is applied at the gate, it

attracts electrical charge from the source, lowering the barrier and allowing the formation of a conductive channel between the source and drain (Figure 1.1).[11] Complementary Metal Oxide Semiconductor (CMOS) technology utilizes both N-channel and P-channel MOSFETs, to behave as a pair of switches working in complementary fashion.[12] As the distance between the source and drain is reduced, an effect known as quantum tunneling prevents sufficient charge separation. Replacement of traditional SiO_2-based dielectrics with materials more resilient to leakage current (e.g. TiO_2, HfO_2, and ZrO_2) can help with this problem.[13]

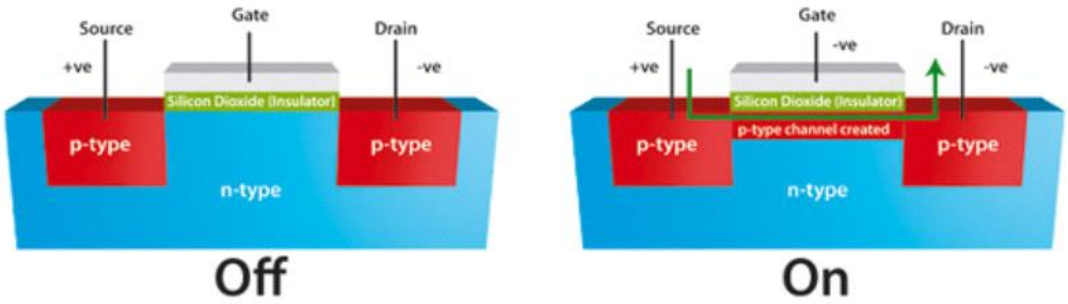

Figure 1.1: P-channel MOSFET structure, without applied voltage (channel closed; left) and with appropriate applied voltage (channel open; right).[14]

The back end of line (BEOL) is the second portion of semiconductor device fabrication, wherein the individual devices (transistors, capacitors, resistors, etc.) are interconnected with wiring on the wafer.[12] BEOL begins when the first layer of metal is deposited on the wafer.[12] Due to its comparatively low resistivity and relative resistance to electromigration, copper has replaced aluminum as the preferred material for conductive interconnect structures.[15] BEOL interconnects are widely viewed as the main driving force

for the development of Cu atomic layer deposition (ALD) processes.[16] These interconnect structures are hierarchically organized layers of metal wires which are connected to each other with Cu vias (electrical connections between layers in a physical electronic circuit, going through the plane of one or more adjacent layers).[16]

One disadvantage of Cu is that it demonstrates poor nucleation upon insulating substrates, preventing the formation of a continuous seed layer. Metals such as Cr, Co, and Ru have been used as seed layers to enhance Cu nucleation.[17] Copper will sometimes diffuse into silicon and SiO_2 substrates at elevated temperatures during device manufacturing. Metallization barriers are used to prevent interdiffusion.[18] Future liners will likely require amorphous layers of only 1–3 atoms with sub monolayer control,[19] so very thin films ($\leq$ 5 nm) of Mn, Cr, and Ru have been suggested as potential Cu diffusion barrier materials.[20] Pt, Ru, and Ir electrode materials have also been proposed as diffusion barriers for metallization in nanocapacitors.[21]

Another area for the application of thin films is heterogeneous catalysis. Typically, solid catalysts consist of nanoparticles on a support. This support is often porous to provide enhanced surface area. Since activity and selectivity of catalysts depend strongly on the particle loading and particle size distribution, the highest quality and most conformal coatings make for overall better catalysts.[22] Dendooven *et al*. compared the deposits and corresponding catalytic activities of two different metal deposition methods.[23] The higher quality film (in terms of uniformity/conformality) had much better electrocatalytic activity than the coarse, non-conformal films with large island formations.[23] Noble metal thin film

deposition is of interest for catalysts within fuel cells,[24] gas sensors, and hydrogen permselective membranes.[25]

1.3 Deposition Methods

Improving electronic device complexity while simultaneously lowering manufacturing costs requires an increase in the quantity and efficiency of transistors on an integrated circuit. This progress has been the motivation behind the development of new thin film deposition processes. Physical vapour deposition (PVD)[26] and chemical vapour deposition (CVD)[27] are well established methods, but struggle to produce uniformly thick ultra-thin films, especially within nano-scale high aspect ratio features.[15] Atomic layer deposition can offer sub-nm thickness control of conformal films, even in high aspect ratio features and upon 3D architectures (Figure 1.2b). Step coverage is a measure of the ability to deposit uniform films within these features. ALD offers vastly improved step coverage when compared to CVD/PVD.

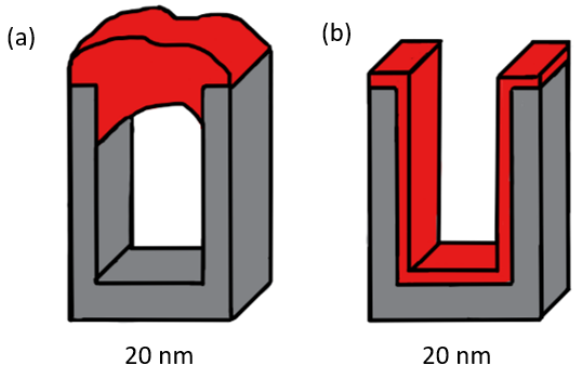

Figure 1.2: Comparison of film coverage and conformality by (a) CVD/PVD (b) ALD within a 20 nm wide trench feature. Deposited material is coloured red, substrate grey.

1.3.1 Physical Vapour Deposition

PVD is broadly comprised of numerous different techniques including laser-ablation deposition, vacuum arc-based deposition, evaporation, and sputter deposition.[26] Each of these methods involve the removal of atoms from a source material prior to deposition on a substrate. This is accomplished by either evaporation or high energy particle bombardment (by photons, electrons, atoms, ions, or molecules) in a vacuum system.[26] For evaporative deposition, atoms are thermally emitted from a source material by heating beyond its vapourization point, while the substrate is placed in the direct line-of-sight to the source (Figure 1.3a). The deposition rate is inversely related to the distance between the sample and the source, which is typically 10–100 cm.[26] Evaporative PVD affords very high deposition rates, oftentimes reaching 100 nm/min.[26] However, evaporated materials will attack the substrate from a mostly single direction, so protruding structures on surfaces will block the material from reaching some areas, limiting the effectiveness of the technique.

Sputter deposition uses energetic particles (50–2000 eV) to bombard a surface which is known as a target.[26] This bombardment dislodges surface atoms with enough energy to overcome surface binding energies and to be emitted from the target (Figure 1.3b). Similar to evaporative PVD, one of the biggest disadvantages with sputtering is its directional nature, which restricts the numbers of atoms entering a trench or via. Generally, atoms deposited by sputtering become effectively restricted from reaching trenches or vias at aspect ratios > 5:1.[18]

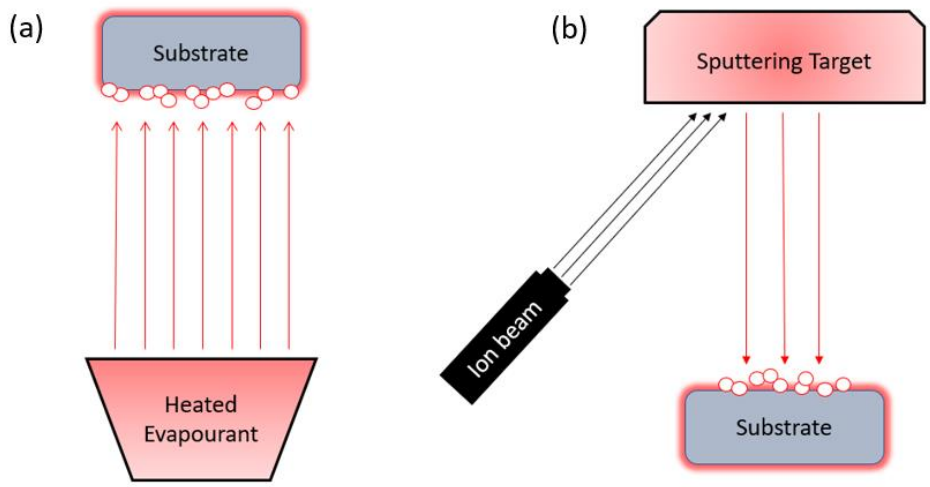

Figure 1.3: Film growth by (a) evaporative PVD, (b) sputter PVD.

1.3.2 Chemical Vapour Deposition

CVD is a technique whereby a substrate is exposed to one or more gaseous chemical precursors simultaneously, in a heated vacuum chamber.[28] A carrier gas (inert, or reactive) is used to introduce the precursor into the reactor chamber, as well as remove any volatile by-products. Film growth results either from the decomposition of a volatile precursor's vapours at the surface of the heated substrate (Figure 1.4a), or through gas-phase reactions between the precursor and reactive carrier gas close to the surface of the heated substrate (Figure 1.4b). In most cases, a large excess of precursor is allowed to flow continually over the substrate surface, so that film thickness is a direct result of exposure time. CVD is typically used to deposit films 0.1–10 μm in thickness, wherein thickness can be controlled via vapour pressure, deposition temperature, gas-flow rate, and duration of exposure.[29]

Some of the advantages of CVD over PVD include the ability to produce films of greater density, uniformity, and reproducibility of thickness. CVD avoids the step coverage

limitations of PVD at feature sizes < 0.25 μm.[30] Gas-phase reactions often lead to particle formation that results in non-conformal and granular films, but this effect can be diminished by reducing the pressure in the reaction chamber, resulting in fewer collisions between gaseous precursors.[31] For this reason, the most common operating conditions of CVD are below atmospheric pressure (Low-pressure CVD; LPCVD) and under ultrahigh vacuum (10^{-8} Torr, Ultrahigh vacuum CVD; UHVCVD). One disadvantage of CVD is that unplanned thermal decomposition of precursors oftentimes results in uncontrolled growth and impurity incorporation in the film. The high temperature conditions of CVD can also be a significant limitation, since it requires long preheating and cool-down times that are incompatible with some polymer based low-κ dielectrics, which are often limited to temperatures < 200 °C.[26]

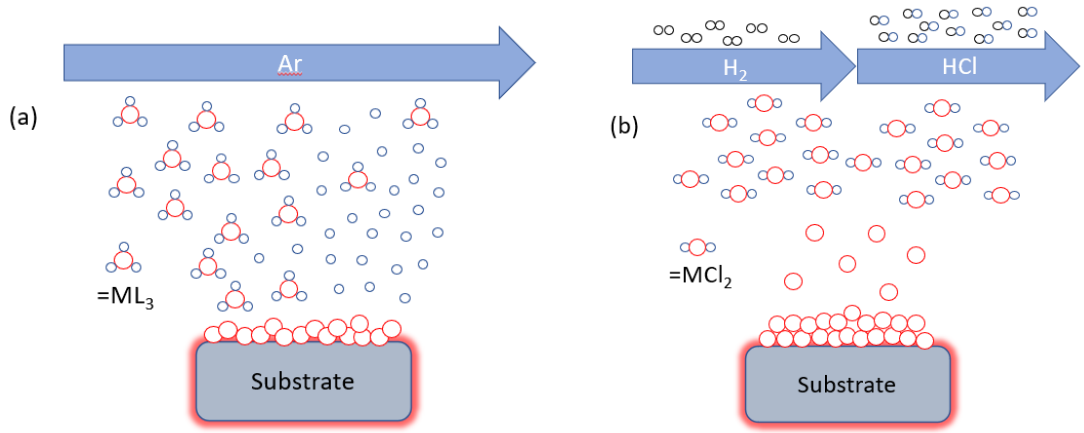

Figure 1.4: (a) Film growth by CVD via decomposition of precursor vapours at the surface of the heated substrate. (b) Film growth by CVD utilizing a generic metal halide precursor and a reactive H_2 carrier gas. The overall reaction scheme can be depicted as $MCl_2 + H_2 \rightarrow M_{(s)} + 2HCl$.

1.3.3 Atomic Layer Deposition

ALD was first proposed in 1952, in the Ph.D. thesis of V. B. Aleskovskii.[32] Tuomo Suntola later developed the technology while working on the manufacture of thin film electroluminescent flat-panel displays in Finland during the mid-1970s.[33] In 1989 the most widely studied ALD process to date was discovered: Al_2O_3 films from the combination of a trimethylaluminum metal precursor and water co-reactant.[34]

The miniaturization of semiconductor devices has led to the introduction of more complex 3D geometries with increasingly high aspect ratios.[1] Due to its self-limiting nature, ALD is exceptionally effective at depositing thin coatings onto such structures. Excellent step coverage through ALD has allowed for the assembly of devices with nanoscale diffusion barriers, electrodes, and insulators for metal-insulator-metal capacitors.[35] ALD supports the precision demands required of next-generational devices, and consequently, interest in ALD continues to rise (Figure 1.5).

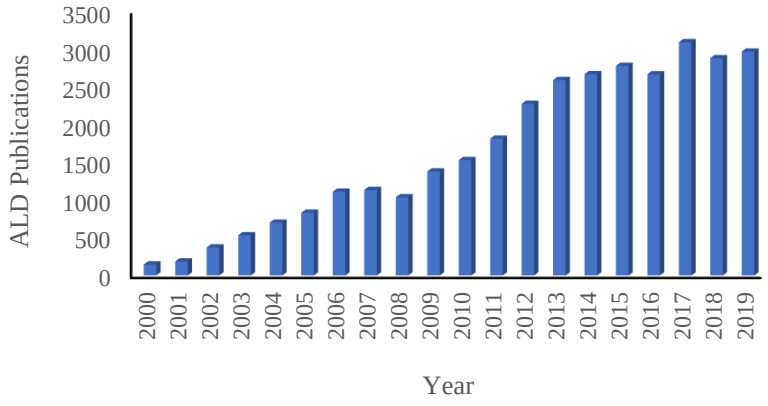

Figure 1.5: Number of ALD publications per year from 2000–2019, via SciFinder.

At its core, ALD is an advanced variant of CVD. Similar to CVD, a volatile metal precursor is employed. However, in ALD both the substrate temperature and precursor thermal stability are finely tuned, preventing thermal decomposition of the precursor upon contact with the substrate.[2] Instead, deposition occurs through the repeated and alternating self-terminated surface-based reactions between the metal precursor and co-reactant (at least one of which is adsorbed on the substrate surface), which are delivered sequentially in the gas phase (Figure 1.6).[2] Careful design of these reactions ensures that only volatile by-products are formed, which are then removed during an inert gas purge step, which follows each precursor and co-reactant pulse, along with any excess metal precursor or co-reactant.[2] Film thickness therefore depends only on the number of precursor/purge/co-reactant/purge cycles.[3] This self-limiting behaviour is integral to the definition of ALD, and without it, the deposition process is known as pulsed-CVD.[2]

There are two major types of ALD processes: thermal and plasma enhanced (PEALD). In thermal ALD, all precursors are molecular species (i.e. plasma is not used). In PEALD, the co-reactant is a plasma, such as O_2 plasma. PEALD requires considerably more complex and expensive hardware, and the surface chemistry for the process is not nearly as straightforward. Plasma based reactions lead to a multitude of reactive gas-phase and surface species, making it difficult to identify the single reactant species responsible for the surface chemistry of interest.[36] Volatile products from the ALD reaction can be ionized as they are leaving the surface, further complicating the overall chemistry.[36] However, many more film options become available, as precursors which are unreactive

towards molecular co-reactants can be considered. Unless otherwise stated, ALD processes described in this thesis will refer to thermal ALD.

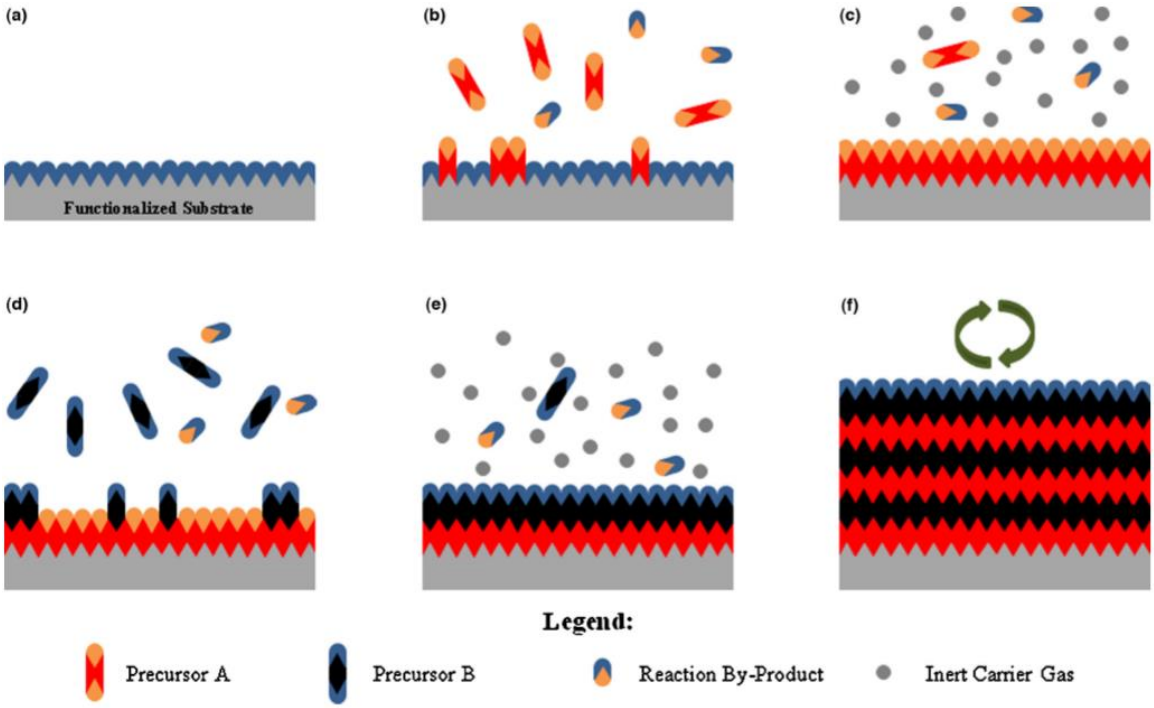

Figure 1.6: Schematic for the ALD process. (a) The substrate surface is either naturally functionalized or is functionalized independently. (b) Precursor A is pulsed and reacts/chemisorbs with the surface. (c) Purge with inert carrier gas removes any excess precursor and reaction by-products. (d) Co-reactant B is pulsed and reacts with precursor A on the surface of the substrate. (e) Purge with inert carrier gas removes any excess co-reactant B and reaction by-products. (f) Steps b–e are repeated until the desired film thickness is achieved. Reproduced with permission from Johnson, R. W.; Hultqvist, A.; Bent, S. F. A Brief Review of Atomic Layer Deposition: From Fundamentals to Applications. *Mater. Today* **2014**, *17*, 236–246.

While PVD and CVD offer higher growth rates, the level of control offered by ALD is unrivaled. The hallmark of an ALD process is a region of constant growth on a plot of growth rate versus precursor pulse length (Figure 1.7). The self-limited mechanism prevents additional growth beyond the minimum saturating dose. Plotting film thickness versus the number of cycles should be linear when saturative precursor doses are applied. The slope of this line indicates the saturative growth rate, while an extrapolated y-intercept can provide insight into potential nucleation issues. Materials are typically deposited by ALD at a rate of 0.1–3.0 Å/cycle.[37]

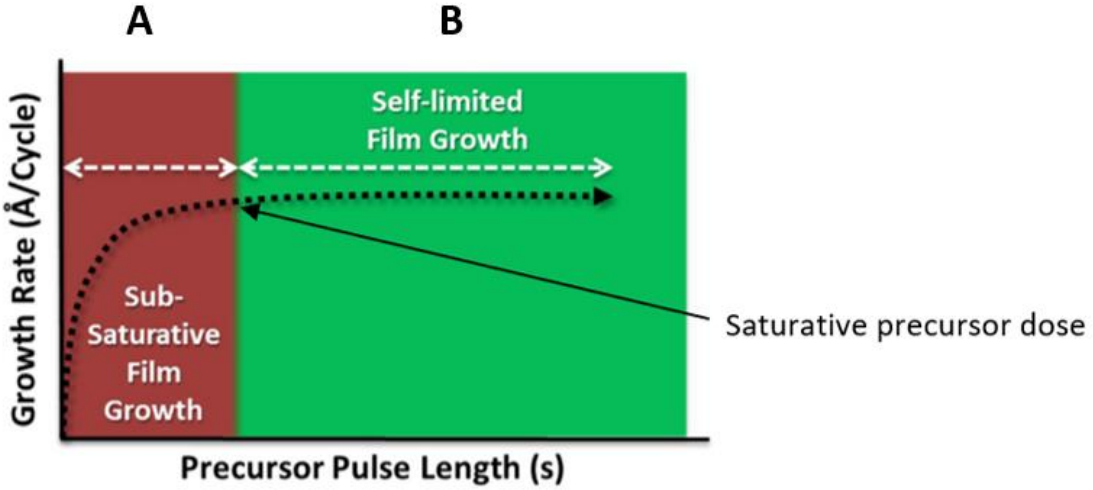

Figure 1.7: Growth rate versus precursor pulse length. Region **A** (red) indicates sub-saturative growth and region **B** (green) indicates saturative growth. Reproduced with permission from Knisley, T. J.; Kalutarage, L. C.; Winter, C. H. Precursors and Chemistry for the Atomic Layer Deposition of Metallic First Row Transition Metal Films. *Coord. Chem. Rev.* **2013**, *257*, 3222–3231.

The thermal behaviour of an ALD process is reported as the dependence of growth rate on deposition temperature. The region where self limiting growth of the target material can be achieved is called the "ALD window".[37] The window itself depends on the physical properties of the precursor and co-reactant and the nature of the chemistry between them. In theory, growth rate should be constant regardless of temperature within the ALD window (since self limiting growth is being demonstrated). However, even for Al_2O_3 ALD (the most widely studied ALD process), this is not true. Al_2O_3 films grown at 33, 125, and 177 °C displayed growth rates of 1.11, 1.34, and 1.25 Å/cycle, respectively.[38] Outside of the ALD window, growth rates can increase due to precursor condensation or thermal decomposition upon the surface of the substrate. Temperature dependant decreases in growth rate can result from insufficient precursor reactivity or desorption of the substrate-bound precursor (Figure 1.8).

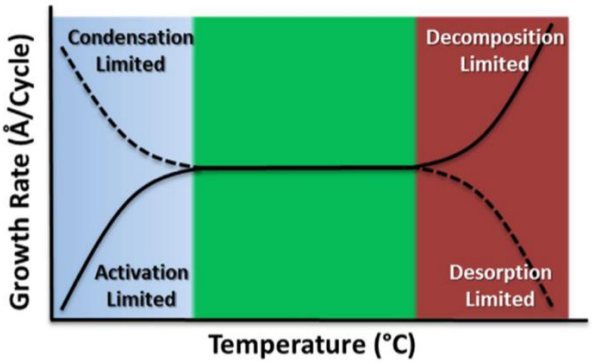

Figure 1.8: Effects of deposition temperature on ALD growth rates. Reproduced with permission from Knisley, T. J.; Kalutarage, L. C.; Winter, C. H. Precursors and Chemistry for the Atomic Layer Deposition of Metallic First Row Transition Metal Films. *Coord. Chem. Rev.* **2013**, *257*, 3222–3231.

1.4 ALD Precursor Fundamentals

The essential physical and chemical properties of metal precursors are: (1) volatility, so that the compound may be delivered at a temperature below that of the substrate, (2) thermal stability, on a long timescale (weeks to months) at the temperature of the delivery bubbler, and a short timescale (seconds or minutes) at the substrate temperature, to allow for ALD without decomposition in the bubbler or parasitic CVD on the substrate, and (3) reactivity, which occurs rapidly at the substrate temperature and leads to the desired material and only volatile by-products.[2] Precursor selection typically requires a compromise of volatility, thermal stability, and reactivity (Figure 1.9).

Adequate thermal stability of the precursor is required to prevent the incorporation of contaminating elements into the film by decomposition, as well as loss of self-limiting growth. Complexes with chelating anionic ligands generally have high thermal stabilities, while complexes with neutral ligands typically have lower thermal stabilities, since loss of a neutral ligand provides a low temperature decomposition pathway. Ligands lacking β-hydrogen atoms are desirable, due to the absence of β-hydrogen elimination pathways.

When comparing precursors, greater volatility (which can enable lower temperature ALD provided that reactivity between precursor, coreactant, and substrate is allowed) is always favourable. Precursors will ideally have vapour pressures at the delivery temperature ranging from 0.01 to 10 Torr, preferably at least 0.1 Torr.[29] Highly volatile precursors are typically monomers comprised of low molecular weight ligands. The steric and electronic properties of the ligands can also affect the volatility of the metal precursor. For example, molecules containing NMe_2 groups have been shown to sublime at lower

temperatures than those with *tert*-butyl groups in analogous positions due to intermolecular repulsions of the nitrogen lone pairs.[39] Ligands containing aromatic moieties are typically poor choices as they may sublime at higher temperatures due to π-stacking interactions in the solid state. Generally, the steric bulk of the ligands should also be kept to a minimum to maximize the density of precursor molecules adsorbed to the substrate.

Liquid precursors are preferred over solids because they have a constant high vapour pressure, while the sublimation rate of a solid depends on its particle size. Utilization of liquid precursors helps to avoid particle incorporation and ensure uniformity in the amount of precursor and co-reactant material delivered in each pulse. However, use of liquid precursors is less important for ALD than CVD because the film thickness depends only on the number of reaction cycles, so long as sufficient minimum saturative dose sizes are achieved during each cycle.

Precursors must demonstrate sufficient adsorption or reaction with surface sites, as well as reactivity toward co-reactants. Two important characteristics of an ALD process are the growth rate and deposition temperature.[2] If growth rate is too low, the process may never effectively translate into manufacturing on an industrial scale. If the deposition temperature is too high, it may not be compatible with certain materials or substrates. It follows that high growth rates and low deposition temperatures are both beneficial for an ALD process to be successful. The overarching chemistry to support the process is ideally also non-toxic, scalable, and cost-effective (simple, high-yield syntheses) for use in high-volume manufacturing.

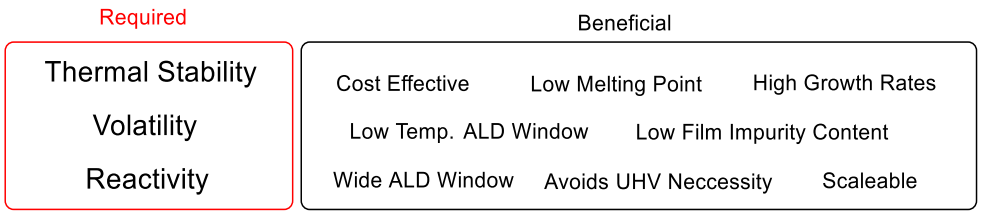

Figure 1.9: Required and beneficial physical and chemical properties of metal precursors.

1.5 Atomic Layer Deposition – Challenges

Metal ALD is best developed for Mo, W, Cu, and the noble metals. The positive or near-zero reduction potentials of these metal ions allows for the reduction of M^X (X = II, III, VI) precursors to the zero valent state by low-temperature (80–160 °C) ALD processes.[40] On the contrary, cations of electropositive metals have negative reduction potentials, and thus typically require the use of plasma to facilitate film growth. Generally, the more positive the reduction potential, the lower the barrier to metal deposition.

The standard reduction potential of Cu^{2+} is +0.34 V, while V^{2+} has a significantly lower value of −1.18 V (Table 1.1).[41] This is reflected by the fact that there are several copper metal ALD processes, while there are currently none for vanadium. Deposition of more electropositive metals often results in the unwanted incorporation of C, N, and O impurities from the coordination spheres of the complexes, or from the co-reactants used during deposition. Naturally, an appealing goal in this field is the development of suitable precursor-co-reactant pairs for metals not yet deposited by ALD (Figure 1.10). Until recently, a lack of strongly reducing co-reactants has greatly limited the ALD of electropositive metal films.

Table 1.1: Standard reduction potentials of first row group 4–11 metals.[41]

$M^{2+} + 2e^- \longleftrightarrow M$	E° (V)
Cu	+0.349
Ni	–0.257
Co	–0.280
Fe	–0.447
Mn	–1.185
Cr	–0.913
V	–1.175
Ti	–1.630

										Al 1.61
Sc 1.36	Ti 1.54	V 1.63	Cr 1.66	Mn 1.55	Fe 1.83	Co 1.88	Ni 1.91	Cu 1.90	Zn 1.65	Ga 1.81
Y 1.22	Zr 1.33	Nb 1.6	Mo 2.16	Tc 1.9	Ru 2.2	Rh 2.28	Pd 2.20	Ag 1.93	Cd 1.69	In 1.78
Lu 1.27	Hf 1.3	Ta 1.5	W 2.36	Re 1.9	Os 2.2	Ir 2.20	Pt 2.28	Au 2.54	Hg 2.00	Tl 2.04

Figure 1.10: Cut-out of the periodic table, showing the first 3 rows of transition metals and the group 13 metals. Films of the metals highlighted in red have been grown by thermal ALD, while those in blue have been reported as ALD-like deposition (*vide infra*).[42] Pauling electronegativities are shown for each element (for values with two decimal places, the oxidation state is: I for group 11, II for groups 4–10 and 12, and III for groups 3 and 13).[43,44]

1.6 Solution-state Reactivity Screening

The fundamental reaction steps of metal ALD processes typically exhibit both similarities and differences to solution conditions.[2] Many of the same steps which take place during solution state reactions may also happen on the surface of a growing metal film, through heterogeneous solid-gas (instead of solid-liquid) interface surface reactions.[2] More overlap will be observed with ALD reactions which occur at low temperature, given that solution reactions are typically carried out below 150 °C.[45]

Winter *et al.* used the observation that an aqueous solution of copper(II) formate undergoes rapid reduction to copper metal upon treatment with hydrazine hydrate[46] to design a three-step ALD process entailing [$Cu(OCHMeCH_2NMe_2)_2$], formic acid, and hydrazine.[47] The copper precursor is initially unreactive towards hydrazine, but once transformed to copper(II) formate during the formic acid pulse, will be readily reduced to copper metal by the subsequent hydrazine pulse.[47] Self-limiting ALD growth was achieved at 120 °C, with a growth rate of 0.50 Å/cycle.[47] The resultant films were reasonably pure, containing 0.1–1.2% carbon, 0.5–1.0% oxygen, and < 2.0% hydrogen.[47]

The compatibility of M(II) (M = Ni, Co, Mn) complexes containing α-Imino alkoxide ligands with $BH_3(NHMe_2)$ was also evaluated by solution screening.[42] Metallic black powders were produced at room temperature (in the case of Ni and Co) or upon reflux (in the case of Mn), and were characterized by PXRD as the corresponding crystalline metal in each case.[42] These results were translated to ALD, but while self-limiting behaviour was observed, film growth only occurred on Ru(5 nm)/SiO_2(100 nm)/Si substrates (*vide infra*).[42]

Solution screening reactions have been used to successfully evaluate the effectiveness of potential co-reactants such as $ZnEt_2$, $AlMe_3$, BEt_3, B_2Pin_2, Sn_2Me_6, and Si_2Me_6 towards copper[3] and nickel precursors (Figure 1.11).[48] The trend of co-reactant reactivity towards both the copper and nickel precursors was $ZnEt_2 > AlMe_3 >> BEt_3 \approx B_2Pin_2 > Sn_2Me_6 > Si_2Me_6$.[48] The nickel precursors required higher reaction temperatures to proceed than the copper analogues, as would be expected given their difference in standard reduction potentials (*vide supra*). Copper (containing ≥ 10% Zn or Al) pulsed-CVD was achieved using $ZnEt_2$ and $AlMe_3$ but not BEt_3, reflective of the solution state observations regarding the reducing potential.[3] Nickel metal film growth did not take place with either $ZnEt_2$ or $AlMe_3$ at the temperatures used for the analogous copper precursors.[48]

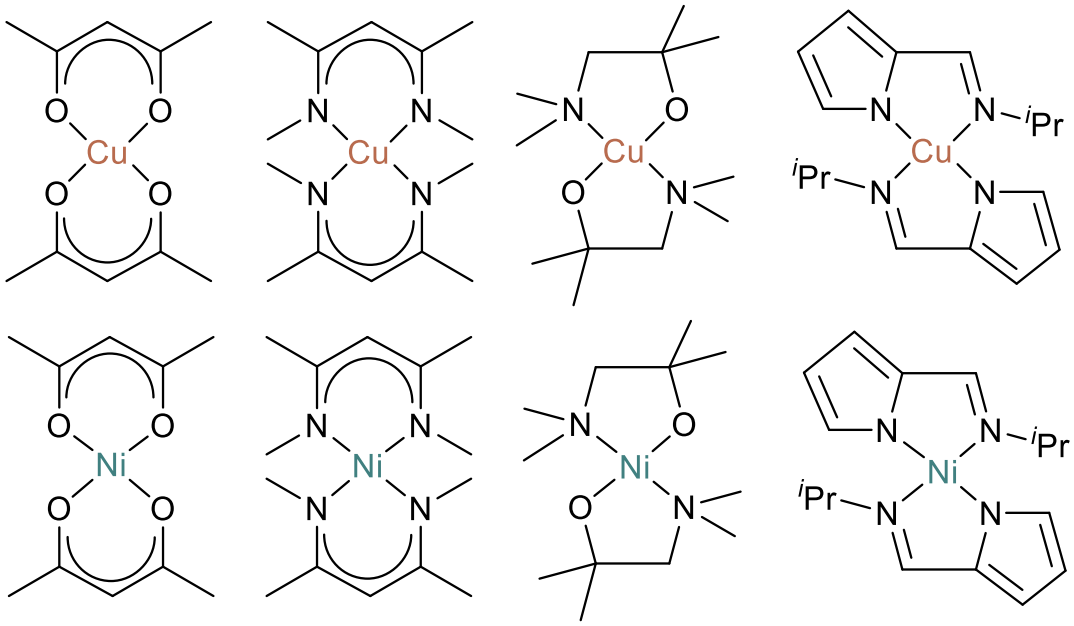

Figure 1.11: Copper(II) and nickel(II) complexes used in solution screening reactions with $ZnEt_2$, $AlMe_3$, BEt_3, B_2Pin_2, Sn_2Me_6, and Si_2Me_6.

These results effectively combine to provide support for the usefulness of solution studies in the identification of new ALD reactivity. This can be very valuable given how resource and time demanding extensive ALD reactor studies can be. It must be noted that the morphologies of films deposited from solution versus ALD can not be expected to correlate. Solution screening studies can be used primarily as a guide to whether certain reduction chemistry is accessible at certain temperatures, and to assess the relative reactivities of new precursors and/or co-reactants.

1.7 ALD Co-reactants

Oxidized metals found in organometallic or inorganic precursor complexes must be reduced to the metallic state to achieve metal film deposition. Molecular H_2 is regarded as the simplest reducing agent available and has been widely used for the ALD of Cu.[16] However, the reactivity of molecular H_2 is limited and not an option for many coordination complexes of metals which are more electropositive than copper. Therefore, chemists have turned to other possible reductants to use as co-reactants (Table 1.2). When imagining potential new co-reactants, it is important to note that the limitations and requirements of precursor molecules (volatility, thermal stability, and reactivity which affords only volatile by-products) still apply.

The following sub-sections will describe the usage of these co-reactants, focusing on mechanistic insights during the reduction and subsequent deposition of their metal precursor pairs.

Table 1.2: Co-reactants for metal ALD, and select metals deposited with those co-reactants.

Class	Co-reactant	Metal(s) deposited
Oxidizers	O_2	Ru[49], Os[50], Rh[51], Ir[52]
	O_3	Ir[53], Pt[54]
$C_xH_yO_z$	Formalin†	Pd[55], Cu[56]
Dihydrogen	H_2	Fe[57], Ru[58], Co[59], Ni[59], Cu[60]
Main group Hydrides	Et_2SiH_2	Cu[61]
	Si_2H_6	Mo[62], W[63]
	SiH_4	W[64]
	$AlH_3(NMe_3)$	Ti-Al‡[65]
	B_2H_6	W[66]
Metal Alkyls	$ZnEt_2$	Cu[67]
Hydrazines	N_2H_4	Ni[68]
	$N_2{}^tBuH_3$	Cu[69]
	$N_2Me_2H_2$	Co[70]

†Formalin is a solution of formaldehyde in water, which often contains a stabilization agent such as methanol to prevent polymerization.[2]

‡UHV-CVD, not ALD. Titanium-aluminum alloy deposited.

1.7.1 Oxidizers

The use of strong oxidizing agents such as O_2 or O_3 to promote metal reduction may seem counter intuitive. The goal of these co-reactants is to oxidize the ligands of the complexes, typically through combustion to release H_2O, and CO or CO_2.[2] Molecular O_2 can reversibly adsorb and dissociate on the surfaces of noble metals to provide access to reactive oxo-species.[71] The resistance of noble metals to bulk oxidation is what allows these co-reactants to be feasibly used.

Iridium metal ALD has been reported using the precursor [Ir(acac)$_3$] with air or O_2 as co-reactants from 225–375 °C.[52] Mechanistic insights for Ir ALD using [Ir(acac)$_3$] and O_2 at 300 °C were gathered using a quartz crystal microbalance (QCM) and Quadrupole mass spectrometry (QMS).[52] The proposed mechanism follows: (1) reaction of [Ir(acac)$_3$] with adsorbed oxygen species on the growing ALD iridium surface, releasing 1–2 acac ligands as acetylacetone and approximately 0.1 ligand through combustion,[52] (2) the remaining acetylacetonate ligands are released by combustion during the following O_2 exposure, which also repopulates the iridium surface with oxygen species.[52]

1.7.2 Formalin

Formalin is used as a reducing agent in late transition metal electroless deposition.[2] ALD of palladium on an alumina substrate with [Pd(hfac)$_2$] and formalin has been extensively studied using QCM[55] and infrared (IR)[72] spectroscopy. The proposed reaction steps are as follows (Scheme 1.1):

$$\text{*Al—OH} + \text{Pd(hfac)}_2 \longrightarrow \text{*Al—O—Pd(hfac)} + \text{H(hfac)} \quad (1)$$

$$\text{*Al—OH} + \text{H(hfac)} \longrightarrow \text{*Al—hfac} + \text{H}_2\text{O} \quad (2)$$

$$\text{2Al*—O—Pd(hfac)} + \text{H}_2\text{C=O} \longrightarrow \text{2Al*—O—Pd—H} + \text{2H(hfac)} + \text{CO} \quad (3)$$

$$\text{*Pd—H} + \text{Pd(hfac)}_2 \longrightarrow \text{*Pd—Pd(hfac)} + \text{H(hfac)} \quad (4)$$

$$\text{*Pd—Pd(hfac)} + \text{H}_2\text{C=O} \longrightarrow \text{*Pd—Pd—H} + \text{H(hfac)} + \text{CO} \quad (5)$$

Scheme 1.1: Overall reaction scheme for the deposition of Pd metal using a [Pd(hfac)$_2$] precursor and formalin co-reactant. Reactions above the line represent nucleation on alumina, while those below involve deposition upon the growing palladium film. Asterisks refer to surface bound species.

The formaldehyde co-reactant appears to form palladium-bound atomic hydrogen, based on QCM measurements which were identical for formaldehyde and H_2. During later stages of deposition (now depositing on palladium, not Al–OH), the reactivity remains the same. The long nucleation period for palladium ALD on Al_2O_3 is attributed to the Al*–hfac species which are formed in reaction (2).

1.7.3 Dihydrogen

Hydrogen is an attractive choice as a co-reactant for metal ALD given its reducing nature. The reactivity involved in copper metal deposition using [$Cu_2(amd^{sBu})_2$] and H_2 was extensively studied using X-ray photoelectron spectroscopy (XPS) and infrared (IR) spectroscopy.[73] Initial reactivity involves the copper precursor and surface OH groups forming Si–O–Cu bonds which results in the release of one equivalent of H(amd^{sBu}) for each [$Cu_2(amd^{sBu})_2$] precursor molecule (Figure 1.12). Once the H_2 co-reactant is

introduced, it reacts with the precursor to release the remaining amidinate ligands as H(amd^{sBu}), yielding copper atoms which can then migrate and agglomerate to form copper particles.[73] While expected, no Cu–H bonds were detected *en route* to copper metal, but this can be reasonably attributed to a low IR absorption cross section or short lifetime.[73]

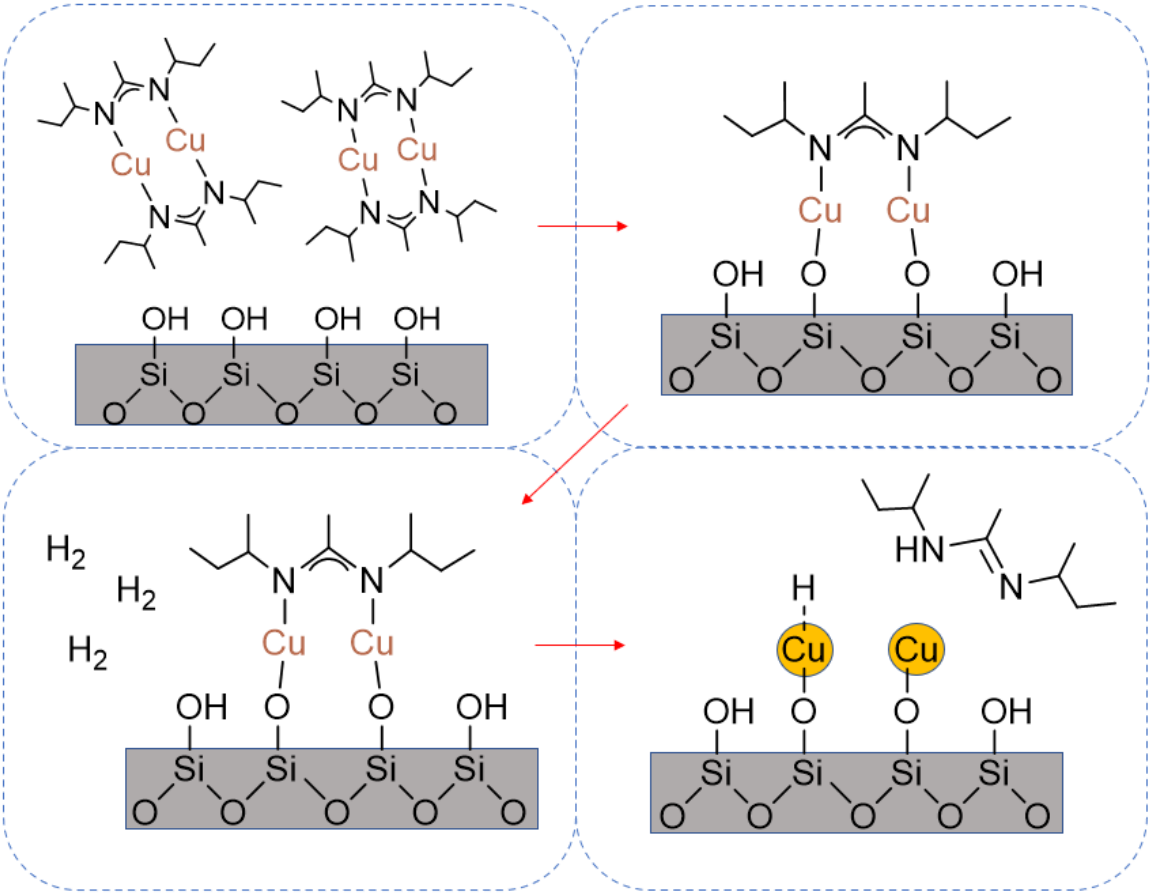

Figure 1.12: Proposed reaction diagram for the deposition of Cu metal from a [Cu_2(amd^{sBu})$_2$] precursor and H_2 co-reactant. Reproduced with permission from Dai, M.; Kwon, J.; Halls, M. D.; Gordon, R. G.; Chabal, Y. J. *Langmuir*. 2010, 26, 3911–3917.

1.7.4 Main-group hydrides

Hydrosilanes such as Et_2SiH_2 and $PhSiH_3$ are valuable reagents used in solution-phase organometallic chemistry for the conversion of metal alkyl (and rarely, metal amido[74]) complexes to metal hydrides.[75] The basis of this reactivity lies within the elementary reactions of either σ-bond metathesis or oxidative addition followed by reductive elimination. These reactions can generate unstable metal hydrides which may undergo further decomposition to generate zero-valent metals. In 2005, Park demonstrated the potential utility of diethylsilane as a reducing agent in ALD, through the deposition of copper films on SiO_2 in combination with a Cu(II) unsymmetrical 1,3-Diketiminate precursor.[76] However, the experimental details described in the paper suggest a technique which cannot truly be termed ALD, and more closely resembles pulsed-CVD.[76]

The CVD of titanium/aluminum alloy films was achieved using $TiCl_4$ and the aluminum hydride reagent $AlH_3(NMe_3)$ at 65−127 °C, but the films were alloyed with aluminum due to the thermal decomposition of $AlH_3(NMe_3)$ to aluminum metal.[65] A new aluminum hydride reducing co-reactant, $[H_2Al(^tBuNCH_2CH_2NMe_2)]$, was used for the growth of aluminum films with an $AlCl_3$[77] precursor, and will be discussed at length in section **1.8.7**.

Borane dimethylamine has been used as a reducing co-reactant to grow films of Ni, Mn, Co, Fe, and Cr, but growth could only be observed on Ru substrates, and ceased after ~1000 cycles (see section **1.8.3**).[42] $BH_3(NHMe_2)$ was recently used as the co-reactant for the deposition of silver metal films from $[Ag(fod)(PEt_3)]$.[78] While self-limiting growth behaviour was observed, the typical linear increase of film thickness as a function of cycles

was unconfirmed.[78] The authors speculated that the $BH_3(NHMe_2)$ reacted on the growing silver surface to form a more strongly reducing species than $BH_3(NHMe_2)$ itself.[78] That is to say, the silver surface catalytically enhanced the growth of silver onto itself.

1.7.5 Diethylzinc

The first reported usage of diethylzinc as an ALD co-reactant was in 2009 by Sung and Fischer.[79] The authors were able to deposit copper metal films at 100−120 °C using $[Cu(OCHMeCH_2NMe_2)_2]$ as the metal precursor.[79] While the mechanism of copper metal ALD using $ZnEt_2$ has not been directly investigated, a detailed study of the solution-state reactions between $[Cu(PyrIm^{iPr})_2]$ and $ZnEt_2$ has been reported.[67] The reactions were primarily monitored by solution NMR spectroscopy, with reaction by-products and intermediates being independently synthesized for conclusive identification. The reaction proceeds as follows: (1) ligand transfer between the copper precursor and $ZnEt_2$, (2) rapid consumption of the resultant copper(II) alkyl complex by either reaction with remaining CuL_2, reaction with another molecule of LCuEt, or reaction with a second molecule of $ZnEt_2$, (3) formation of CuEt via reaction of Cu_2L_2 from the previous step with $ZnEt_2$, (4) decomposition of the highly thermally unstable ethyl copper species to copper metal via β-hydride elimination and reductive elimination (Figure 1.13).[67]

Use of diethylzinc should be restricted to precursors which can be delivered at temperatures below 120 °C, so that substrate temperatures can be set below 130 °C. Substrate temperatures are kept higher than delivery line temperatures to prevent condensation of precursor vapours upon the substrate. $ZnEt_2$ will begin to thermally

decompose above this temperature, causing a parasitic zinc CVD contribution to the deposition which can lead to significant amounts (> 10%) of zinc incorporation in the resultant films.[80]

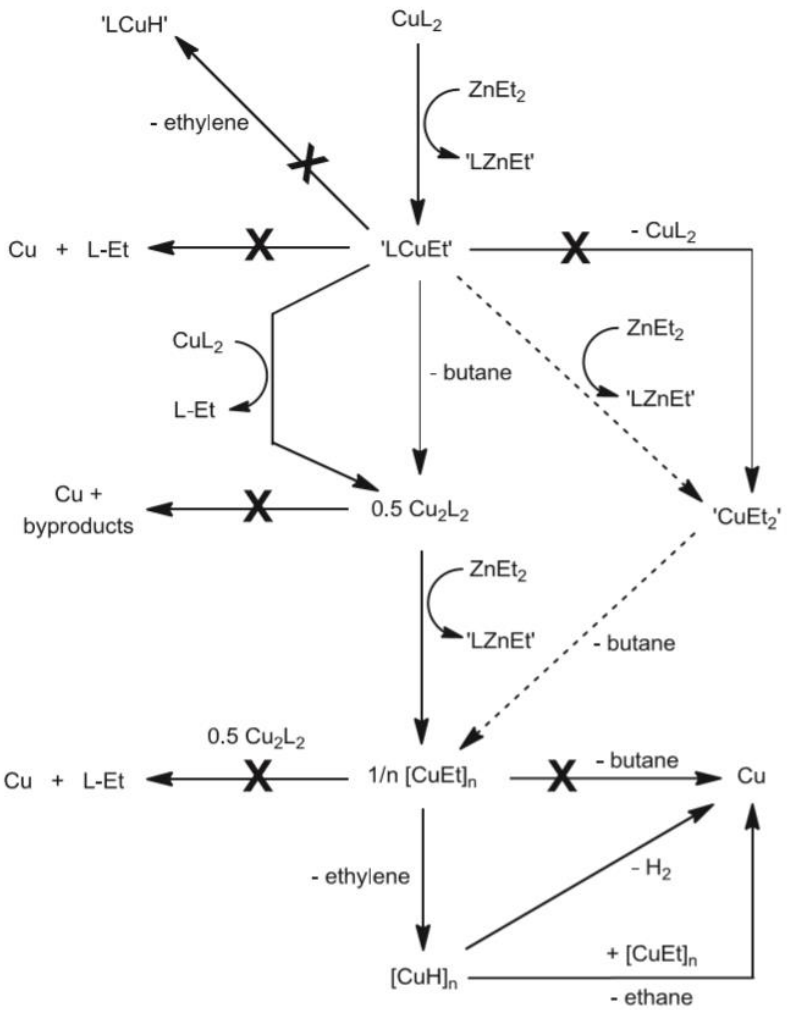

Figure 1.13: Reaction pathways for room temperature copper metal deposition from $[Cu(PyrIm^{i}Pr)_2]$ with $ZnEt_2$. Reproduced with permission from Emslie, D. J. H.; Chadha, P.; Price, J. S. Metal ALD and Pulsed CVD: Fundamental Reactions and Links with Solution Chemistry. *Coord. Chem. Rev.* **2013**, *257*, 3282–3296.

1.7.6 Hydrazines

Cobalt metal ALD is possible at the low temperature of 140 °C using [(allyl$^{t\mathrm{Bu}}$)Co(CO)$_3$] and dimethylhydrazine.[70] The unique nucleation sequence involved in this process will be discussed in detail in a later section (**3.2**). Once the nucleation has completed, the surface-bound cobalt allyl species likely reacts with dimethylhydrazine to form a surface-bound cobalt hydrazide species. This 1,2-dimethylhydrazide complex may undergo β-hydride elimination to provide a pathway to an unstable metal hydride, which can decompose further to metallic cobalt.[81]

Deposition of copper metal using [Cu(OCHMeCH$_2$NMe$_2$)$_2$] with formic acid and hydrazine was discussed earlier (**1.6**), and analogous chemistry was used to deposit nickel metal films using [Ni(OCHMeCH$_2$NMe$_2$)$_2$] and the same co-reactants at 175 °C.[68]

1.8 Electropositive Metal ALD Processes

With methodical design, inorganic and organometallic complexes can meet the three major chemical and physical requirements of effective ALD precursors. The following subsections will focus on precursor design features, co-reactant selections, and metal precursor reactivity at the surface, with subsections arranged by metal.

1.8.1 Titanium

Titanium metal thin films are well suited for a variety of important applications in semiconductor device technologies.[65] Ultra-thin Ti adhesion layers are used in current integrated circuits, while titanium/aluminum alloy liners have been proposed for advanced

transistor structures.[82] Due to its very negative electrochemical potential (Ti(II) → Ti(0), E = −1.631 V)[41] there are limited reports of titanium metal film growth from chemical precursors.

A rare thermal ALD process using $TiCl_4$ as the metal precursor and 2-methyl-1,4-bis(trimethylsilyl)-2,5-cyclohexadiene or 1,4-bis(trimethylsilyl)-1,4-dihydropyrazine as the co-reactant was reported in 2015 by the Winter group.[83] Design of the process arose from the observation that the co-reactants were able to successfully reduce early transition metal halide complexes from their highest to lower oxidation states, as reported in a series of papers by Mashima and co-workers.[84] Both co-reactants react with metal halides to eliminate $ClSiMe_3$ (Scheme 1.2). It is proposed that intermediate complexes 2-methyl 1,4-cyclohexadienyl or 1,4-dihydropyrazinyl are formed, which then eliminate aromatic toluene or pyrazine, reducing the metal center by two electrons per ligand.[83] The co-reactants sublime at 70 and 80 °C, respectively, whereas decomposition takes place at > 300 and > 265 °C, providing sufficient volatility and thermal stability for ALD.[83]

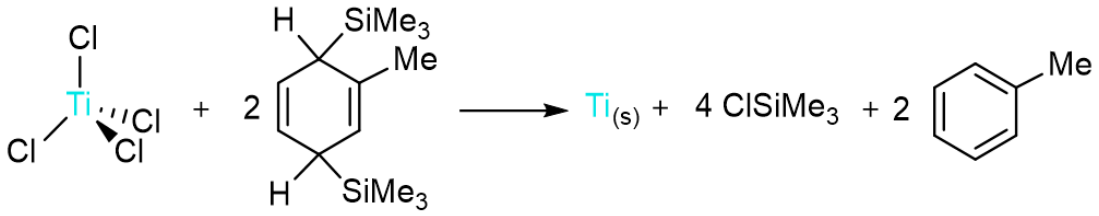

Scheme 1.2: Reaction between precursor and co-reactant for the deposition of titanium metal employing titanium tetrachloride and 2-methyl-1,4-bis(trimethylsilyl)-2,5-cyclohexadiene.

Plotting growth rate versus $TiCl_4$ pulse length reveals a growth plateau at > 0.2 s pulse lengths, with a saturative growth rate of 0.06 Å/cycle (Figure 1.14).[83] Experiments involving pulses of $TiCl_4$ and nitrogen (instead of 2-methyl-1,4-bis(trimethylsilyl)-2,5-cyclohexadiene) or 2-methyl-1,4-bis(trimethylsilyl)-2,5-cyclohexadiene and nitrogen (instead of $TiCl_4$) lead to no observable film growth, demonstrating that growth requires both precursor and co-reactant and does not occur via decomposition of either.[83]

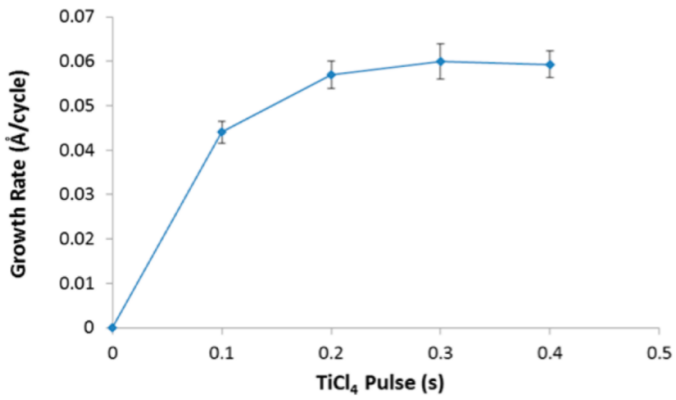

Figure 1.14: Growth rate versus $TiCl_4$ pulse length. Reproduced with permission from Klesko, J. P.; Thrush, C. M.; Winter, C. H. Thermal Atomic Layer Deposition of Titanium Films Using Titanium Tetrachloride and 2-Methyl-1,4-Bis(Trimethylsilyl)-2,5-Cyclohexadiene or 1,4-Bis(Trimethylsilyl)-1,4-Dihydropyrazine. *Chem. Mater.* **2015**, *27*, 4918–4921.

Films grown on Si(100) wafers containing native oxide at 140 and 180 °C were analyzed.[83] The films were exposed to ambient atmosphere prior to analyses, leading to oxidation of the surface. X-ray diffraction spectra of the films showed no reflections, which suggests either amorphous character or oxidation of the titanium.[83] The films were electrically nonconductive, again consistent with rapid oxidation of the surface. XPS

revealed major ionizations matching TiO_2 ($3p_{3/2}$ 459.2 eV) as well as minor ionizations matching Ti_2O_3 ($2p_{3/2}$ 457.4 eV) and TiO ($2p_{3/2}$ 455.4 eV),[85] while no titanium metal was observed ($2p_{3/2}$ 453.8 eV).[86] However, upon sputtering with 3 keV argon ions for > 70 min, the $2p_{3/2}$ ionizations exactly matched titanium metal (453.8 eV).[83] Argon sputtering will progressively reduce TiO_2 to Ti_2O_3 and then TiO, but never completely to titanium metal.[85] Further XPS depth profiling revealed the bulk of the film to be comprised of Ti(0) with low carbon (2.9–3.0%), nitrogen (< 0.5%), silicon (0.8–2.2%), and chlorine (1.8–2.3%) impurities.[83]

A full ALD study of $TiCl_4$ with 1,4-bis(trimethylsilyl)-1,4-dihydropyrazine lead to the following observations. Saturative growth was achieved for both $TiCl_4$ and 1,4-bis(trimethylsilyl)-1,4-dihydropyrazine, with a growth rate of 0.10–0.12 Å/cycle within an ALD window of 90–100 °C.[83] Once again, X-ray diffraction spectra did not show any reflections, but XPS analyses revealed titanium metal 2p ionizations upon sputtering.[83] XPS depth profiling revealed significant carbon (9–16%) and nitrogen (5–7%) impurities, meaning these films were much less pure than those grown with 2-methyl-1,4-bis(trimethylsilyl)-2,5-cyclohexadiene.[83]

1.8.2 Vanadium

Vanadium oxide undergoes a metal to insulator transition at 68 °C, corresponding to significant changes in the electrical conductivity and optical properties.[87] Thin films of vanadium oxide can have potential application as smart window coatings,[88] infrared

modulators,[89] catalysts,[90] and gas sensors.[91] Also, vanadium oxide has been widely studied in the context of lithium-ion batteries.[92]

Various CVD precursors (Figure 1.15) are available for the deposition of vanadium oxides, including vanadium chlorides ([VCl_4][93] and [$VOCl_3$][94]), vanadium alkoxides ([$VO(O^iPr)_3$],[95] [$VO(OC_2H_5)_3$],[96] and [$V(OCMe_2CH_2OMe)_3$][97]), vanadium β-diketonates ([$V(acac)_3$],[98] [$VO(acac)_2$],[99] [$VO(tmhd)_2$],[100] and [$VO(hfod)_2$][100]), as well as nitrogen-containing compounds ([$V(NMe_2)_4$][101] and [$VO(NO_3)_3$][95]).

Films of VO_x have been grown by ALD using [$V(NEtMe)_4$][102] or [$V(NMe_2)_4$][103] and either water or ozone as co-reactants. Thin films that span the common oxidation states of vanadium oxides (V_2O_3, VO_2, and V_2O_5) have also been grown using vanadium (III) *tris*(*N*,*N*'-diisopropylacetamidinate), with either O_3, H_2O_2, H_2O/O_2, or H_2O_2/H_2.[104] As yet, vanadium metal film growth has not been reported by CVD or ALD.

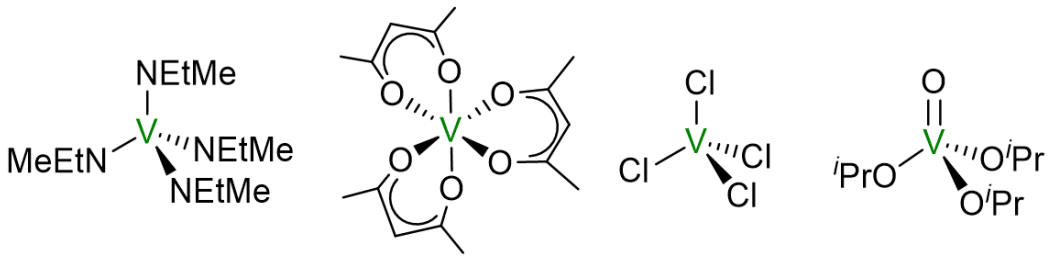

Figure 1.15: CVD precursors for the deposition of vanadium oxide.

1.8.3 Chromium

Thin films of chromium metal have many applications, such as layers for improved adhesion to transparent substrates,[105] and transparent electrodes.[106] Transparent conducting films (TCFs) are thin films of optically transparent and electrically conductive material.

TCFs are important components in liquid-crystal displays, OLEDs, touchscreens and photovoltaics.[107] Most TCFs are made of indium tin oxide (ITO), but ultrathin transparent chromium metal contacts provide some advantages over common conductive transparent metal oxides such as ITO.[108] Chromium thin films possess optical transparency close to ITO in the visible and near-infrared range (0.4–2.5 μm), while the ultraviolet (175–400 nm) and mid-infrared (2.5–25 μm) regions can have optical transparency which is significantly higher.[109]

The only report of Cr metal ALD utilized $Cr(Me^tBuCOCN^tBu)_2$ as the metal precursor and $BH_3(NHMe_2)$ as the reducing co-reactant (Scheme 1.3). The chromium complex sublimes at 115 °C, melts at 175 °C, and decomposes at 230 °C. The process demonstrated a growth rate of 0.08 Å/cycle within the 170–185 °C ALD window.[42]

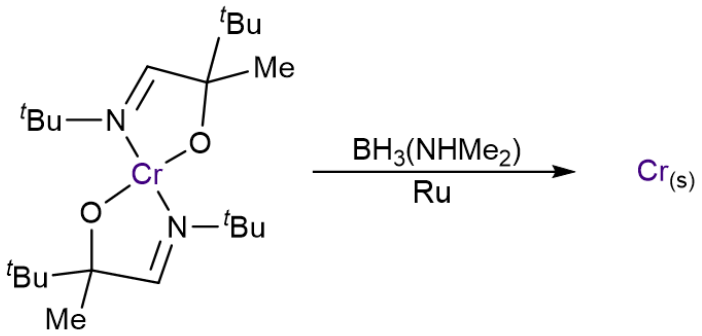

Scheme 1.3: Overall reaction for the deposition of chromium metal employing $Cr(Me^tBuCOCN^tBu)_2$ and $BH_3(NHMe_2)$.

Film growth only occurred on a Ru(5 nm)/SiO_2(100 nm)/Si substrate, and required a 50 cycle nucleation process consisting of 20 s pulses of the precursor, 1 s pulses of $BH_3(NHMe_2)$, and purge times of 5 and 10 s after the precursor and co-reactant pulses,

respectively.[42] Saturative growth occurred at 180 °C with pulse lengths of > 4.0 s for $Cr(Me^tBuCOCN^tBu)_2$ and > 1.0 s for $BH_3(NHMe_2)$.[42] Plotting thickness versus number of cycles reveals linear growth up to 1000 cycles but plateauing of film thickness beyond that (Figure 1.16). The cause of this strange effect is not entirely clear but has been attributed to catalytic activation of $BH_3(NHMe_2)$ by the ruthenium substrate.[42] Once the growing metal layer blocks all of the available Ru sites, deposition ceases. Testing this idea, Mäkelä *et al.* sought to investigate the effect of Ru activation during a silver metal ALD process using $Ag(fod)(PEt_3)$ and $BH_3(NHMe_2)$.[78] Catalytic Ru surfaces were placed inside their ALD reactor and $BH_3(NHMe_2)$ would be activated before entering the reaction chamber.[78] The ruthenium plate was separated from the precursor delivery lines in order to ensure contact only with the $BH_3(NHMe_2)$ co-reactant. The Ru was shown to enhance the growth of silver metal thin films by raising the growth rate from 0.3 Å/cycle to 0.33–0.35 Å/cycle.[78] The authors were not able to conclusively identify what species were formed on contact with the Ru surface, but they hypothesized about the formation of $(Me_2N–BH_2)_2$.[78]

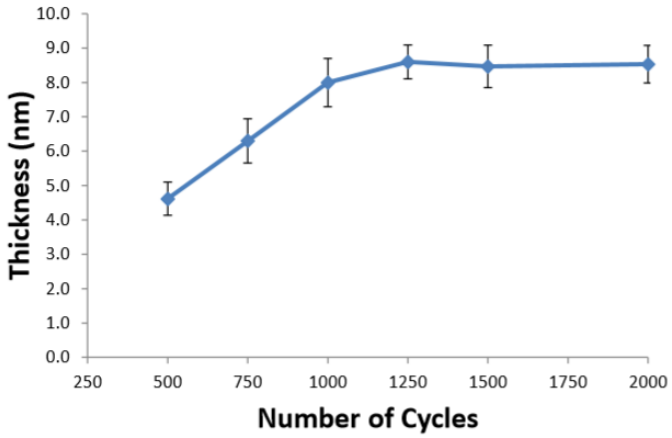

Figure 1.16: Cr film thickness as a function of the number of deposition cycles at a deposition temperature of 180 °C. Thickness has a linear relationship with the number of cycles (indicative of ALD-type growth) up to 1000 cycles. Reproduced with permission from Kalutarage, L. C.; Martin, P. D.; Heeg, M. J.; Winter, C. H. Volatile and Thermally Stable Mid to Late Transition Metal Complexes Containing α-Imino Alkoxide Ligands, a New Strongly Reducing Coreagent, and Thermal Atomic Layer Deposition of Ni, Co, Fe, and Cr Metal Films. *J. Am. Chem. Soc.* **2013**, *135*, 12588–12591.

Atomic force microscopy (AFM) images of films grown at 170 and 180 °C had root mean squared surface roughness of 0.37–0.59 nm, indicating smooth surfaces. XPS spectra of a Cr film grown at 170 °C showed Cr 2p binding energies matching Cr_2O_3.[42] After argon ion sputtering for 60–90 s Cr 2p binding energies matching Cr metal were revealed.[42] This result is again consistent with the surface of the films being oxidized upon exposure to air.

1.8.4 Tungsten

Tungsten ALD from WF_6 and Si_2H_6 has been extensively studied by QCM, IR spectroscopy, mass spectrometry, auger electron spectroscopy (AES) and XPS.[110,111] The overall chemistry is based on fluorosilane elimination reactions, with the driving force being the formation of very stable Si–F bonds through highly exothermic reactions.[28]

In situ FTIR studies observed absorbances from Si–H and W–F stretching vibrations on surface species during the WF_6 and Si_2H_6 exposures.[63] WF_6 pulses caused Si–H stretching vibration absorbances to decrease and W–F stretching vibration absorbances to increase. Conversely, upon Si_2H_6 pulses, Si–H stretching vibration absorbances increase with a concurrent decrease in W–F stretching vibrations absorbances. Tungsten metal film growth is linearly proportional to the number of AB cycles (Scheme 1.4). QCM studies measured tungsten film growth at a rate of 4–7 Å/cycle, varying across surface temperatures from 177–325 °C and Si_2H_6 exposures from $\sim 10^4$ to 10^6 Langmuirs.[111] This growth rate per cycle is greater than the unit cell length of tungsten.[112] The increase in growth rate depending on surface temperature and/or Si_2H_6 exposure has been attributed to Si_2H_6 insertion into Si−H bonds.[113] This insertion mechanism leads to a parasitic Si CVD contribution to the W ALD growth. The extra silicon sites can result in additional W deposition during the subsequent WF_6 pulses, further perpetuating the large growth rates. Additional Si–H bond insertion and Si_2H_6 decomposition contributions are more significant at higher temperatures and longer Si_2H_6 exposure times.[62]

$$WSiHFSiH_3^* + 2WF_6 \longrightarrow WWWF_4^* + 2SiF_4 + 1.5H_2 + HF \qquad (A)$$

$$WF_4^* + Si_2H_6 \longrightarrow WSiH_2F^* + SiHF_3 + 1.5H_2 \qquad (B1)$$

$$WSiH_2F^* + 0.5Si_2H_6 \longrightarrow WSiHFSiH_3^* + 0.5H_2 \qquad (B2)$$

Scheme 1.4: Overall reaction scheme for the deposition of W metal from WF_6 and Si_2H_6. (A) Half reaction during WF_6 pulse, (B1) & (B2) Half reactions during the Si_2H_6 pulse. Asterisks refer to surface bound species.

1.8.5 Molybdenum

Molybdenum has similar physical and chemical properties to tungsten. Mo ALD was investigated using an analogous precursor/co-reactant system (MoF_6 and Si_2H_6).[62] The overall reaction scheme can be described in the same way as above (Scheme 1.3), with a heat of reaction of $\Delta H = -221$ kcal. Mo ALD from MoF_6, like W ALD from WF_6, has rapid nucleation and large growth rates per cycle (6.0 Å/cycle, much greater than the lattice constant of 3.15 Å for the body-centered cubic unit cell of Mo[114]). One important observation which distinguishes the MoF_6 process from the WF_6 process is mass loss during Si_2H_6 exposure (contrary to mass gain in tungsten ALD).[62] This rejects insertion of Si_2H_6 into Si–H bonds or Si_2H_6 decomposition as explanations for the high growth rate. The following half reactions can be used to explain the high growth rate (Scheme 1.5):

$$MoF_5^* + Si_2H_6 \longrightarrow MoSiH_xF_{3-x}^* + SiH_{2-x}F_{2+x} + 2H_2 \quad (B)$$

$$MoSiH_xF_{3-x}^* + MoF_6 \longrightarrow MoMoF_5^* + SiH_xF_{4-x} \quad (A1)$$

$$MoMoF_5^* + MoF_6 \longrightarrow MoMoMoF_5^* + 3F_2 \quad (A2)$$

Scheme 1.5: Half reactions for the MoF_6 (A1 & A2) and Si_2H_6 (B) pulses during Mo metal ALD. Valid for x = 0, 1, and 2, for x = 3, the gas phase reaction products are SiF_4 + HF + H_2.[62] Asterisks refer to surface bound species.

The high exothermicity of the Mo ALD reaction facilitates additional Mo deposition through the decomposition of MoF_6 into metallic molybdenum and fluorine gas during MoF_6 exposures.[62] This decomposition is endothermic with a heat of reaction of ΔH = +372 kcal. It is proposed that the highly exothermic Mo ALD reaction is coupled with the endothermic MoF_6 decomposition reaction. Coupling of endothermic and exothermic reactions is a common technique in heterogenous catalysis.[115] Films grown in a high vacuum chamber using lower pressure and longer co-reactant pulse lengths had no Si impurities, while those grown in a viscous flow reactor had Si impurities up to 16 at%.[62] The authors hypothesized that silicon impurities likely resulted from the high exothermicity of the Mo ALD reaction which causes decomposition of Si_2H_6 during periods of higher reaction rates.[62]

1.8.6 Manganese

The most crucial application for thin films of metallic manganese are self-forming $MnSi_xO_y$ diffusion barriers between copper interconnect wiring and dielectric materials containing silicon and oxygen.[116] In 1997, [$^{Me}CpMn(CO)_3$] was shown to deposit films of elemental $Mn_{(s)}$ by CVD.[76] These films could be grown either in the presence or absence of H_2.[117] Other CVD precursors which have been used to successfully deposit elemental $Mn_{(s)}$ films (Figure 1.17) include [$Mn\{(^iPrN)_2C^nBu\}_2$],[118] [bis[1-(tertbutylamide)-2-dimethylaminoethane-N,N′]manganese],[119] and [$^{Et}Cp_2Mn$],[120] each of which requiring H_2 as a reactive carrier gas. CVD in the absence of H_2 was also successful using [$Mn\{(RN)_2CR'\}_2$][121] precursors.

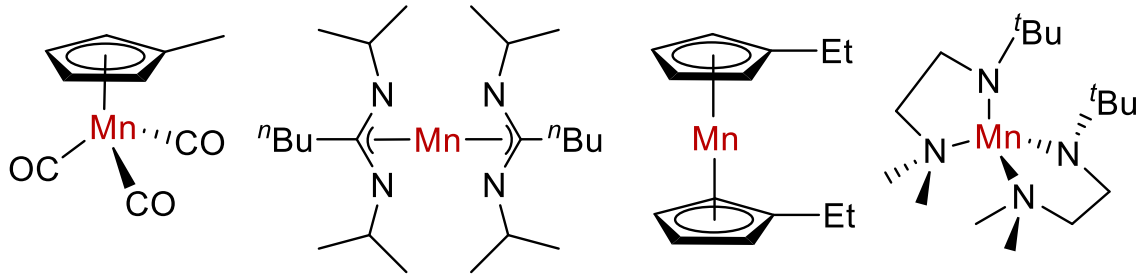

Figure 1.17: CVD precursors for the deposition of elemental manganese.

The most prevalent manganese-containing thin films grown by ALD are films of manganese oxide. In 2003, The first reported ALD process for manganese oxide films used a [$Mn(dpm)_3$] metal precursor and ozone co-reactant.[122] This combination has remained the popular choice for the majority of reports on manganese oxide ALD.

There are limited articles regarding ALD processes for manganese-containing films which are not oxides. The Winter group has reported deposition of a Mn/Cu alloy through

a 3 step method which uses the combination of [$Mn_2(^tBuNCHC(^tBu)(Me)O)_4$] and [$Cu(OCHMeCH_2NMe_2)_2$] metal precursors with $BH_3(NHMe_2)$.[123] The Cu:Mn ratios of the films were approximately 70:30 and could be controlled by varying the number of Cu and Mn precursor cycles.[123] Deposition was observed at a rate of 0.09 Å/cycle and films were deposited on Pd and Pt substrates, as well as Ru.[123]

Winter *et al.* have also reported Mn metal ALD using the same Mn(II) α-imino alkoxide dimer [$Mn_2(^tBuNCHC(^tBu)(Me)O)_4$] and $BH_3(NHMe_2)$ (Scheme 1.6), chemistry which is analogous to the Cr process discussed previously (*vide supra*).[42] A manganese oxide film was produced, but authors interject that this was due to initial deposition of Mn metal followed by oxidation after exposure to air.[42] Once again, deposition was only observed on Ru substrates, wherein film growth stopped after complete coverage of the substrate.[42]

The Zaera group have claimed metallic $Mn_{(s)}$ ALD should be possible using [$^{Me}CpMn(CO)_3$] and H_2.[124] During their ALD experiment they observed the deposition of manganese silicide and manganese oxide films through 3 ALD cycles upon a Si/SiO_2 substrate.[124] Mn atoms have been shown to diffuse into silica,[121] so if elemental manganese was in fact deposited, the conversion of Mn(0) to manganese silicide and manganese oxide is not an unexpected result. The authors suggest that $Mn_{(s)}$ deposition should be possible on an alternative substrate, or through the use of an alternative reducing agent.[124]

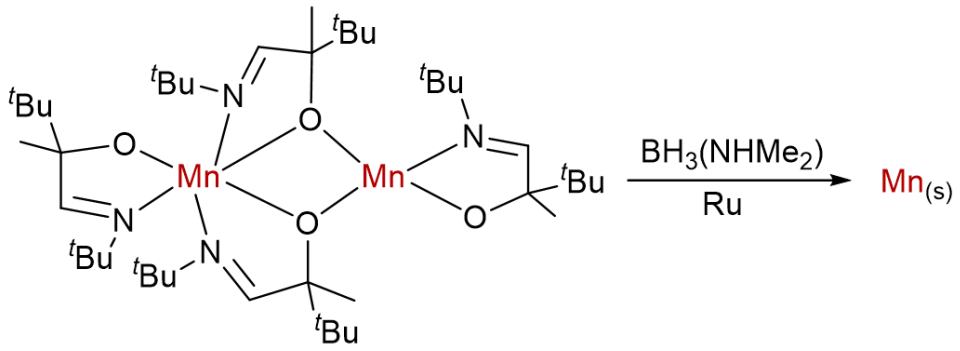

Scheme 1.6: Potential ALD process for elemental manganese deposition.[42]

1.8.7 Aluminum

Nanoscale films of aluminum metal are desired for uses in microelectronics,[125] energetic materials,[126] hydrogen storage,[127] and plasmonics.[128] Thermal ALD using a $AlCl_3$ metal precursor and the amido-amine stabilized Al dihydride [$H_2Al(^tBuNCH_2CH_2NMe_2)$] as the reducing co-reactant has been reported by Blackeney and Winter (Scheme 1.7).[77] With an electrochemical potential of –1.676V ($Al^{3+} \leftrightarrow Al^0$),[129] this technique marks the deposition of the most electropositive metal by thermal ALD to date.

Aluminum-hydrides are typically non-volatile, though some volatile examples do exist. $AlH_3(NMe_3)_2$ has been used for the CVD of Al,[130] but lacks the thermal stability for ALD. [$H_2Al(^tBuNCH_2CH_2NMe_2)$] was designed to be monomeric and have a high thermal stability.[77] These characteristics are based on the chelate effect, a saturated carbon backbone, reasonably high steric bulk, and the strong electron donating ability of the *tert*-butylamido group.[77] The complex is a colourless crystalline solid with a melting point of 31–32 °C. As per thermogravimetric analysis (TGA), the new co-reactant sublimes without decomposition at 70 °C and has a vapour pressure of 0.75 Torr at the same temperature.

ALD experiments between $AlCl_3$ and $H_2Al(^tBuNCH_2CH_2NMe_2)$ were undertaken upon several different substrates (Si, SiO_2, Pt, Cu, TiN).[77] Deposition was successful on all substrates, but TiN was chosen for a complete ALD study due to its large resistivity difference compared to Al.[77] To rule out CVD-type growth and prove self-limiting ALD behaviour, the pulse lengths of both precursor and co-reactant were varied at 140 °C. Results conclusively showed a saturated growth rate of 3.5 Å/cycle during pulse lengths ≥ 1.0 s for both precursor and co-reactant after 200 cycles.[77] A growth rate of 3.5 Å/cycle is significantly higher than most other ALD processes, but not unheard of (ALD of W metal films from WF_6 can achieve growth rates up to 6.7 Å/cycle,[63] *vide supra*). The authors suggested that the high growth rates may be due to the adsorption of more than one monolayer of $AlCl_3$, or surface oxidation (due to exposure to air prior to analysis) which complicates the quantification of total film thickness measurements.[77]

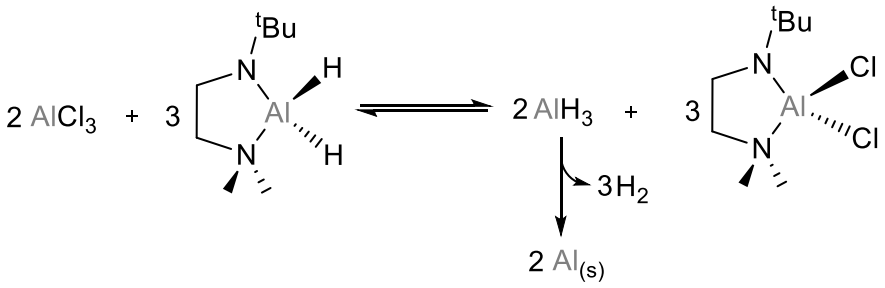

Scheme 1.7: Proposed reaction between $AlCl_3$ and $[H_2Al(^tBuNCH_2CH_2NMe_2)]$ leading to Al metal film deposition.

At temperatures of 160 and 180 °C, film growth was characterized by higher surface roughness resulting from increased agglomeration of Al particles.[77] Growth rate also decreased steeply at 180 °C, likely due to the thermal decomposition of

[$H_2Al(^tBuNCH_2CH_2NMe_2)$].[77] When less than 100 deposition cycles were used, the resulting films were nonconductive due to discontinuous particle formation; a minimum of 200 cycles were necessary for the Al islands to coalesce forming nearly continuous films.[77] The films were very high in purity, with C and Cl impurities below the detection limit of XPS survey scans. This is a significant improvement over a previously reported PE-ALD process using $AlMe_3$ and H_2 plasma, wherein C impurities were found to be 3%.[131] Nitrogen impurities were present at 1–2%, and can be attributed to either incorporation of the amido-amine ligand or the TiN substrate itself.

1.9 Thesis Goals

This work details the development and evaluation of potential novel metal precursor and co-reactant combinations for the ALD of mainly electropositive transition metals (Cr, V, Mo, and W). The research is primarily investigative in nature, closely examining the three necessary properties of metal ALD precursors: volatility, thermal stability, and reactivity. Many of the complexes discussed are homoleptic, bearing either alkyl or allyl ligands.

Work involving the chemistry of novel Mn compounds which was carried out at the start of my graduate research will also be discussed.

Table 1.3: Metal precursor/co-reactant combinations for the ALD of electropositive transition metals.

Metal	Precursor	Co-reactant	ALD Window (°C)	Substrate
Titanium	$TiCl_4$[83]	2-methyl-1,4-bis(trimethylsilyl)-2,5-cyclohexadiene	110-240	Si(100)
	$TiCl_4$[83]	1,4-bis(trimethylsilyl)-1,4-dihydropyrazine	90-100	Si(100)
Chromium	$Cr(Me^tBuCOCN^tBu)_2$[42]	$BH_3(NHMe_2)$	170-185	$Ru/SiO_2/Si^\dagger$
Manganese	$Mn(Me^tBuCOCN^tBu)_2$[42]	$BH_3(NHMe_2)$	225	$Ru/SiO_2/Si^\dagger$
Aluminum	$AlCl_3$[77]	$H_2Al(^tBuNCH_2CH_2NMe_2)$	100-160	TiN
Tungsten	WF_6[63]	Si_2H_6	177-325	Si(100)
Molybdenum	MoF_6[62]	Si_2H_6	90-150	Si(100)

†Growth was only observed on a Ru substrate and ceased after 1000 cycles

Chapter 2 – Homoleptic Transition Metal Alkyl Complexes

2.1 Introduction to Homoleptic Transition Metal Alkyl Complexes

$W(CH_3)_6$ and $Ti(CH_3)_4$ were two of the first transition metal alkyl complexes to be discovered, in the early 20th century.[132] At the time, the consensus amongst organometallic chemists was that metal-carbon bonds were weak in general, causing a roadblock in the syntheses of many imagined complexes.[133] Studies later revealed that poor choice of alkyl ligands was the cause of failure in isolating many imagined metal complexes.[134] Sterically bulky alkyl ligands were shown to kinetically stabilize their associated complexes relative to less bulky analogues. Alkyl complexes with ligands bearing β-hydrogens are typically unstable, being subject to decomposition via β-hydride elimination (Scheme 2.1). This issue can be avoided by substituting β-hydrogen substituents with alkyl groups. The introduction of alkyl groups that were both bulky and lacking β-hydrogens (especially Me_3SiCH_2, $(Me_3Si)_2CH$, and Me_3CCH_2) significantly broadened the scope of transition metal alkyl chemistry.[135] Aside from β-hydride elimination, other possible routes for decomposition of alkyl complexes include α-hydride elimination, oxidative addition of a γ–C–H bond, reductive elimination, bi-nuclear reductive elimination, and M–C bond homolysis (Scheme 2.1).

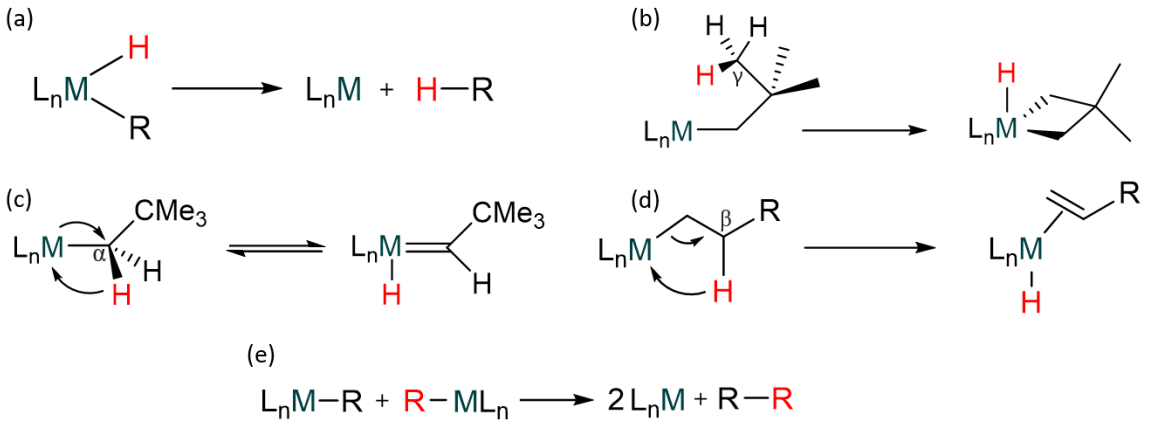

Scheme 2.1: (a) reductive elimination, (b) oxidative addition of a γ–C–H bond, (c) α-hydride elimination, (d) β-hydride elimination, (e) bi-nuclear reductive elimination.

During reductive elimination, the alkyl ligand forms a bond with a second X-type ligand on the metal, reducing the metal oxidation state by two units, and decreasing the total electron count by two units (Figure 2.1a). When ligand X is a hydride, reductive elimination is often both kinetically and thermodynamically favourable. Bi-nuclear elimination is a type of reductive elimination which involves two metal centers (separate complexes or a bimetallic compound). Here, alkyl ligands bound to two different metal centers will couple with one another, reducing the metal oxidation state by two units, and decreasing the total electron count by two units (Figure 2.1e). In γ–C–H bond oxidative addition, concerted oxidative addition results in the formation of a hydride ligand and a metallocycle. For this reason, γ–C–H bond oxidative addition is often referred to as cyclometallation (Figure 2.1b). When the hydride located on the alpha position of the alkyl ligand is transferred to the metal center, resulting in the formation of a carbene, the process is termed α-hydride elimination (Figure 2.1c). For β-hydride elimination, the hydride

located on the beta position of the alkyl ligand is transferred to the metal center, leading to the formation of an alkene, which will subsequently dissociate in the case of a d^0 metal centre (Figure 2.1d).

Given the wide array of available decomposition routes, it is difficult to give an invariant order to the relative stability of metal alkyl complexes as a function of the alkyl ligand. However, broadly speaking, stability typically follows: 1-norbornyl > $PhCH_2$ > Me_3SiCH_2 ≅ Me_3CCH_2 > Me_3SnCH_2 > Ph > Me >> Et > *sec*- or *tert*-butyl.[135] Though, these comparisons are only useful when comparing complexes of the same metal with the same oxidation state and co-ligands (analogous complexes with the exception of the alkyl groups).

Formally, metal-carbon bond breaking may be uni- or bimolecular. Migration of a substituent from the ligand to the metal (α-hydride elimination, β-hydride elimination, oxidative addition of a γ–C–H bond, reductive elimination) or M–C bond homolysis are typically unimolecular processes. Bond homolysis is relatively uncommon amongst transition metal alkyl complexes, requiring relatively higher activation energy and only occurring when other processes are hindered or blocked completely.[135] Bond homolysis is more common for first row transition metals, since it results in a change of one unit in the oxidation state of the metal (1st row transition metals more commonly undergo 1-electron redox processes).

The occupancy of many coordination sites enhances stability even with small ligands, as displayed in the synthesis of stable hexamethyl tungsten.[136] The bulk imposed

by neopentyl and related ligands causes metal coordination numbers to be lower than would otherwise be expected, influenced primarily by the nature of the ligand rather than the oxidation state and electronic configuration of the metal. For example, there is an extensive series of four-coordinate $[M(CH_2SiMe_3)_4]$ (M = Ti,[137] Zr,[137] Hf,[137] V[134] or Cr[134]) complexes. Furthermore, when the bulkier $CH(SiMe_3)_2$ ligand is employed, MR_4 complexes become sterically inaccessible, leading to MR_3 complexes for metals with a readily accessible 3+ oxidation state $[M\{CH(SiMe_3)_2\}_3]$ (M = Ti,[138] V,[138] Cr[138]).

In most homoleptic transition metal alkyl complexes, the alkyl ligands are terminally bound to the metal via a two-center two-electron bond (e.g.; $[Ti(CH_2SiMe_3)_4]$ and $[Zr(CH_2CMe_3)_4]$). However, alkyl ligands may also bridge between two metal atoms, as seen in $[Cu_4(CH_2SiMe_3)_4]$,[139] where the Cu atoms are arranged in a plane with the methylene carbon atoms in the same plane as the Cu_4 square.

Homoleptic transition metal alkyl complexes are most often prepared via halogen-alkyl exchange, utilizing either an organolithium or Grignard reagent. Both reducing power and alkylating ability follow the order RLi > RMgCl > R_2Mg.[135] Therefore, when choosing an appropriate reagent, the superior reactivity of organolithium reagents must be weighed against the potential for undesirable reduction of the metal center. One such example is during the synthesis of $[Ti(CH_2SiMe_3)_4]$, which undergoes extensive reduction when the lithium alkylating reagent $LiCH_2SiMe_3$ is used, in diethyl ether.[139] Alternatively, a product with a higher oxidation state than the starting material metal halide can be formed, when alkylation is accompanied by disproportionation. Some examples include the Cr^{IV}

complexes [$Cr(CH_2SiMe_3)_4$] and [$Cr(norb)_4$] which are both accessible from Cr^{III} chlorides.[140]

2.2 Transition Metal Alkyl Complexes as ALD Precursors

Examples of homoleptic transition metal alkyl complexes as ALD precursors for elemental metal deposition are very limited. [$Ti(CH_2CMe_3)_4$] and H_2 plasma have been studied as precursor and coreactant respectively, but TiC_x films were obtained instead of elemental Ti.[141] Experiments using molecular H_2 as opposed to plasma also resulted in the growth of TiC_x films.[141] Girolami has conducted extensive mechanistic studies to gather insight into the thermal instability of [$Ti(CH_2CMe_3)_4$] and the formation of titanium carbide under CVD conditions.[142] In solution, the titanium complex is observed to thermolyze and eliminate 2.1 equivalents of neopentane as the principal organic product.[142] Deuteration of the alkyl groups at the α positions reveals a deuterium kinetic isotope effect which provides clear evidence that the thermolysis is initiated by α-hydrogen abstraction to form neopentane.[142] The resultant product is a titanium alkylidene, which activates C–H bonds of saturated and unsaturated hydrocarbon solvents.[142] A γ-hydrogen activation pathway can also be detected under special circumstances, but this pathway is approximately 25 times slower than the α-hydrogen abstraction process previously mentioned.[142]

While homoleptic examples are rare, there are instances of metal ALD precursors which contain some alkyl ligands in their coordination sphere. PEALD processes have been investigated by Kim[143] and Hong[144] with Ta(V)-tri(neopentyl)-dichloride and hydrogen

plasma. Both authors observed the deposition of TaC_x films instead of the targeted elemental metal deposition, but self-limiting growth was achieved.

The first successful Au ALD process was reported by Griffiths *et al.* in 2016.[145] Authors reported the use of [$AuMe_3(PMe_3)$] and oxygen plasma, at a deposition temperature of 120 °C.[145] Molecular hydrogen, hydrogen plasma, and molecular oxygen were all unable to grow any type of films at this temperature.[145] The films contained high levels of oxygen and phosphorous impurities which were attributed to the formation of P_2O_5.[145] When water was added as a second co-reactant to convert P_2O_5 to volatile phosphoric acid, phosphorous impurities fell below the detection limit of XPS and oxygen content decreased sharply, to 1.8%.[145]

Mäkelä *et al.* reported the first thermal Au ALD process in 2017.[146] They used [$Me_2Au(S_2CNEt_2)$] and O_3 as precursor and coreactant respectively to obtain metallic gold films from 120–200 °C with a growth per cycle that increased relative to temperature from 0.4 to 1.1 Å/cycle.[146]

The suitability of transition metal alkyl complexes with dative 1,2-bis(dimethylphosphino)ethane (dmpe) and bis-(dimethylphosphino)methane (dmpm) has been investigated within the Emslie group by Price and coworkers.[147] Bis(trimethylsilylmethyl)- and dineopentyl-Mn(II) complexes react with dmpe and dmpm to yield monomeric [$Mn(dmpe)(CH_2SiMe_3)_2$] and dimeric [$\{(\mu\text{-dmpe})Mn(CH_2CMe_3)_2\}_2$] respectively.[147] [$Mn(dmpe)(CH_2SiMe_3)_2$] is especially well suited for ALD, thermally decomposing very little over 24 hours at 120 °C, and subliming at 60 °C (5 mTorr).[147]

Reaction of the Mn(II) complexes with molecular H_2 in solution resulted in the liberation of $SiMe_4$ or CMe_4 and dmpe, as well as the deposition of Mn metal.[147] Solution state reactions with $ZnEt_2$ resulted in the formation of MnZn alloys and release of ethane, ethylene, and $ZnX(CH_2EMe_3)$ (X = Et and CH_2EMe_3; E = Si, C).[147]

2.3 Rationale for Thermal Stability Test Conditions in the Thesis

The concepts of viscous and molecular flow dictate the transport of volatilized precursors through delivery lines in an ALD reactor. During viscous flow, there are frequent collisions between gas molecules, but far less frequent collisions with walls of carrier channels (Figure 2.1a).[148] Under high vacuum conditions, molecular flow results in practically no molecular interactions but far more collisions with walls of the carrier channels (Figure 2.1b).[148] During ALD experiments, viscous flow is desirable to help molecules travel along delivery lines, as well as into and out of the reaction chamber. This reduces purge times between precursor pulses and prevents precursors from traveling up other delivery lines, potentially condensing in unheated sections. Viscous flow is achieved within an ALD reactor by having a flow of inert gas accompanying the vacuum. This results in a much higher pressure (often ~1 Torr) than the absolute pressure of the vacuum (often 5–20 mTorr), requiring higher precursor bubbler temperatures to ensure precursor volatility and subsequent delivery. Within this thesis, long time scale (to replicate ALD delivery bubbler conditions) thermal stability studies are carried out at a temperature which is 40 °C higher than the sublimation temperature of the complex at 5 mTorr. Thermal stability studies in this work are also assessed on samples in the solid state (unless otherwise noted),

again replicating ALD delivery bubbler conditions where precursors are held as neat (solvent-free) compounds. Precursors which can be sublimed without decomposition at 5 mTorr, but are unstable at a temperature 40 °C higher than the sublimation temperature, are less likely to be viable as ALD precursors. However, they may be useful as CVD precursors since CVD reactors are more easily operated under high vacuum (e.g. 1–20 mTorr).

Figure 2.1: Viscous vs. molecular flow; molecular movement represented by arrows.

2.4 Homoleptic Transition Metal Alkyl Complexes

In the introduction to this chapter, it was discussed that reductive elimination is a common decomposition pathway for transition metal alkyl complexes, and that when one of the ligands is a hydride, reductive elimination is often both kinetically and thermodynamically favourable. This favourable reactivity may be harnessed to overcome the energy barrier in the reduction of highly electropositive transition metal complexes (Scheme 2.2). With this reactivity in mind we set out to uncover volatile and thermally stable homoleptic transition metal alkyl complexes, for use as novel ALD precursors.

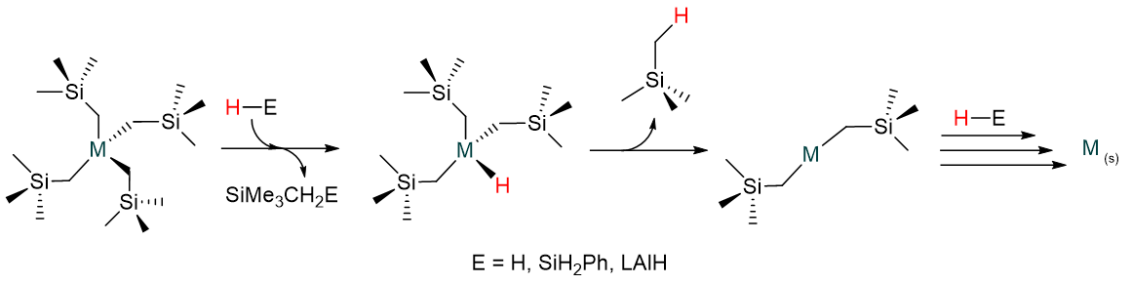

Scheme 2.2: Envisioned reactivity between a homoleptic metal alkyl complex and an aluminum hydride compound, phenylsilane, or molecular hydrogen. The alkyl hydride complex formed after initial metathesis can undergo reductive elimination to reduce the metal oxidation state by 2 units, eventually yielding M^0.

2.4.1 Synthesis and Investigation of $[Cr(CH_2SiMe_3)_4]$ (1) and $[Cr(CH_2CMe_3)_4]$ (2)

$[Cr(CH_2SiMe_3)_4]$ **(1)** and $[Cr(CH_2CMe_3)_4]$ **(2)** were originally prepared by Wilkinson *et al.* from 1972–1973, through the reaction of $CrCl_3{\cdot}3THF$ with the Grignard reagents Me_3SiCH_2MgCl or Me_3CCH_2MgCl.[134,149] The formation of tetravalent **1** and **2** from a trivalent starting material can principally be explained by a disproportionation reaction of an unstable R_3Cr intermediate. Compounds **1** and **2** were synthesized via slightly modified literature procedures, where the dialkyl magnesium compounds $Mg(CH_2SiMe_3)_2$ and $Mg(CH_2CMe_3)_2$ were used in place of the traditional Grignard reagents. The dialkyl magnesium reagents were collected through the application of the Schlenk equilibrium, which can be represented as follows: $2\ RMgX \rightleftharpoons MgX_2 + MgR_2$. Addition of dioxane to a solution of a Grignard reagent leads to the precipitation of MgX_2(dioxane). The removal of this product drives the equilibrium almost completely to

the right hand side of the equation, allowing for the collection of the dialkyl magnesium reagent.[150]

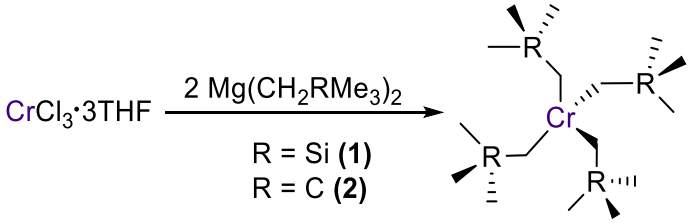

Scheme 2.3: Synthesis of $[Cr(CH_2SiMe_3)_4]$ **(1)** and $[Cr(CH_2CMe_3)_4]$ **(2).**

Complexes **1** and **2** were obtained in 29% and 43% yields, respectively (Scheme 2.3). Complex **1** is a deep purple solid which melts at temperatures as low at 40 °C and can be sublimed at room temperature (5 mTorr), while complex **2** is a purple-brown solid which can be sublimed at 40 °C (5 mTorr). Compounds **1** and **2** are both paramagnetic Cr(IV) complexes. While unsuitable for complete characterization, the ^{1}H NMR spectra provide a fingerprint which allows the thermal stability to be assessed.[a] Negligible decomposition took place upon heating a solid sample of complex **1** at 60 °C for 24 hours. However, if the sample was heated for a longer period (up to 3 days) severe decomposition was observed, judged by ^{1}H NMR spectroscopy and the production of tetramethylsilane (TMS) (Figure 2.2). After heating complex **2** at 80 °C for 36 hours, the sample had completely decomposed, and neopentane was the sole species observable by ^{1}H NMR spectroscopy. To rule out the possibility of light sensitivity being a factor in the decomposition, tests were repeated in the absence of light, but identical results were observed.

[a]In an NMR tube fitted with a J. Young valve, a 'before' NMR is taken of the compound in question. NMR solvent is removed *in vacuo* and the solid is heated for the desired duration, under an argon atmosphere. Once complete, an 'after' NMR is taken.

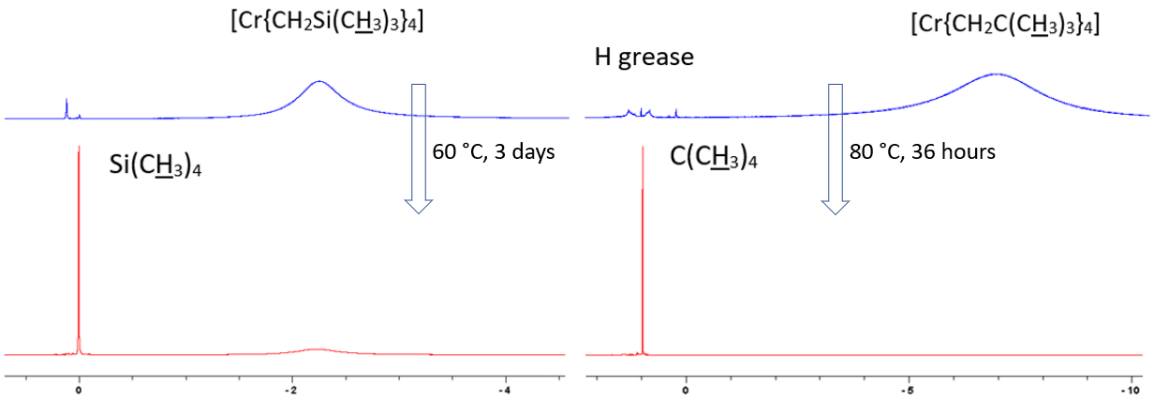

Figure 2.2: Left: ^{1}H NMR spectra (C_6D_6, 600 MHz) of [Cr(CH_2SiMe_3)$_4$] **(1)** before heating (top, blue) and after heating at 60 °C for 3 days (bottom, red). Right: ^{1}H NMR spectra (C_6D_6, 600 MHz) of [Cr(CH_2CMe_3)$_4$] **(2)** before heating (top, blue) and after heating at 80 °C for 36 hours (bottom, red).

Solution state reactivity studies of complex **2** towards H_2 and were performed. 15 mg of complex **2** was dissolved in 10 mL of toluene and sealed in a 50 mL flask, which was then filled with approximately 2 atm of H_2. There were no observable changes after heating the solution at 50 °C for 24 hours. The temperature was increased to 70 °C, and after 48 hours the solution had progressed from maroon to colourless, with signs of a feint metallic (in appearance) film coating the glassware as well as an insoluble black precipitate. The precipitate was collected and dried *in vacuo*, then packed into a capillary which was sealed under an inert argon atmosphere for powder X-ray diffraction (PXRD) analysis. The material was judged to be amorphous by PXRD. Due to the harsh conditions required (70 °C, 48 hrs), thermal decomposition likely played a major role in the observed changes, as opposed to reactivity with hydrogen. An NMR scale test reaction of complex **1** and 5 equiv. of phenylsilane displayed no reactivity, even upon heating to 60 °C for 24 hours.

While a crystal structure for complex **2** had been published previously,[140] single crystal X-ray diffraction analysis was performed as part of a graduate course which yielded interesting results. Compound **2** was originally reported to crystallize in the space group *Pbca*, with a unit cell containing one highly disordered molecule. We were able to solve the crystal structure in the $Pca2_1$ space group, which revealed two molecules in the asymmetric unit displaying no disorder (Figure 2.3). The previously published structure was collected at 183 K, while the structure which we acquired was collected at 100 K. To ensure that this new solution was not a result of the difference in collection temperatures, data collection was repeated on the same crystal at 183 K, and resulted in the new solution once again.

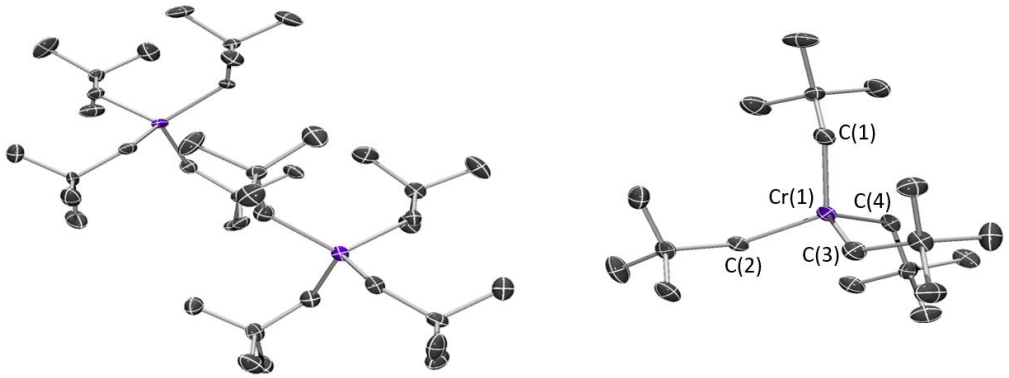

Figure 2.3: X-ray crystal structure of $[Cr(CH_2CMe_3)_4]$ **(2)** with ellipsoids drawn at 50% probability. Hydrogen atoms omitted for clarity. Space group $Pca2_1$, R_1 = 8.69. One molecule of the asymmetric unit shown on right. Bond distances (Å) and angles (°): Cr(1)–C(1) 2.029(16), Cr(1)–C(2) 2.025(16), Cr(1)–C(3) 2.017(14), Cr(1)–C(4) 2.012(15), C(1)–Cr(1)–C(2) 115.9(6), C(1)–Cr(1)–C(3) 106.6(6), C(1)–Cr(1)–C(4) 106.3(4), C(3)–Cr(1)–C(2) 107.2(5), C(4)–Cr(1)–C(2) 105.6(4), C(4)–Cr(1)–C(3) 115.3(4).

Table 2.1: Selected bond distances and angles for $[Cr(CH_2CMe_3)_4]$, obtained by Gamboratta *et al.* and reported in 2002, contrasted with selected bond distances and angles for $[Cr(CH_2CMe_3)_4]$ **(2)** as obtained at 100 K.

	This work	Gamboratta *et al.*
Equivalent Atom Labels	$[Cr(CH_2CMe_3)_4]$ **(2)**	$[Cr(CH_2CMe_3)_4]$[9]
Cr(1)–Cr(1)	2.029(16)	2.016(12)
Cr(1)–Cr(2)	2.025(16)	1.986(12)
Cr(1)–Cr(3)	2.017(14)	1.996(13)
Cr(1)–Cr(4)	2.012(15)	2.002(13)
C(1)–Cr(1)–C(2)	115.9(6)	113.6(5)
C(1)–Cr(1)–C(3)	106.6(6)	106.6(5)
C(1)–Cr(1)–C(4)	106.3(4)	108.1(5)
C(3)–Cr(1)–C(2)	107.2(5)	107.0(5)
C(4)–Cr(1)–C(2)	105.6(4)	106.1(5)
C(4)–Cr(1)–C(3)	115.3(4)	115.5(5)

2.4.2 Synthesis and Investigation of $[V(CH_2SiMe_3)_4]$ (3)

$[V(CH_2SiMe_3)_4]$ **(3)** was first prepared by Wilkinson *et al.* in 1972, through the reactions of either VCl_4 or $VOCl_3$ with the Grignard reagent Me_3SiCH_2MgCl (Scheme 2.3).[134] Compound **3** was independently synthesized in an 18% yield starting from $VOCl_3$,

with modifications to the procedure. Initial attempts at synthesis were complicated through use of the dialkylmagnesium reagent instead of the traditional Grignard reagent. The reported procedure uses a large excess of the Grignard reagent (6 equiv.) and purifies the crude product by recrystallization, after removal of insoluble salts by filtration. The high solubility of $Mg(CH_2SiMe_3)_2$ in diethyl ether and slight solubility in hexanes prevented its removal by filtration as described. This led to a significant amount of large $Mg(CH_2SiMe_3)_2$ crystals growing from the recrystallization. To avoid this problem, the crude product was instead purified via sublimation. Similar to compound **1**, compound **3** is very volatile and can be sublimed at room temperature (5 mTorr).

During the addition of $VOCl_3$ to $Mg(CH_2SiMe_3)_2$, the reaction mixture appears to proceed through a blue intermediate prior to turning green upon reaction completion. During an attempted synthesis of **3**, $[\{V(CH_2SiMe_3)_3O\}_2Mg(dme)_2]$ (dme = 1,2-dimethoxyethane) **(4)** was isolated by filtering the crude reaction mixture, removing the solvent *in vacuo* and recrystallizing the blue-green residue from dme (Scheme 2.4). Compound **4** was crystallographically characterized, and while the quality of the data is poor, it is useful for showing connectivity of the atoms (Figure 2.4). The complex is the sole example of a first-row transition metal oxo complex featuring a bridging Mg atom and alkyl ligands on the transition metal. The crystal structure also provides some insight into the reaction mechanism for the synthesis of **3**. From this V^{IV} intermediate, an additional equivalent of the Grignard reagent could substitute the oxo group bound to the metal center, eliminating MgO. Similar Mg bridged oxo complexes have been observed during the

reactions of 2nd or 3rd row transition metal oxychlorides and Grignard reagents, including $[(Me_4ReO)_2Mg(thf)_4]$,[151] $[(Me_4WO)_2Mg(thf)_4]$,[152] and $[(Me_4MoO)_2Mg(thf)_4]$.[153]

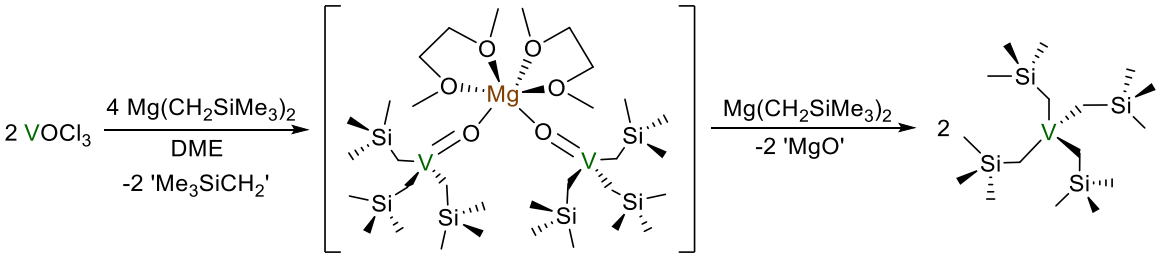

Scheme 2.4: Synthesis of $[\{V(CH_2SiMe_3)_3O\}_2Mg(dme)_2]$ **(4)** and $[V(CH_2SiMe_3)_4]$ **(3).**

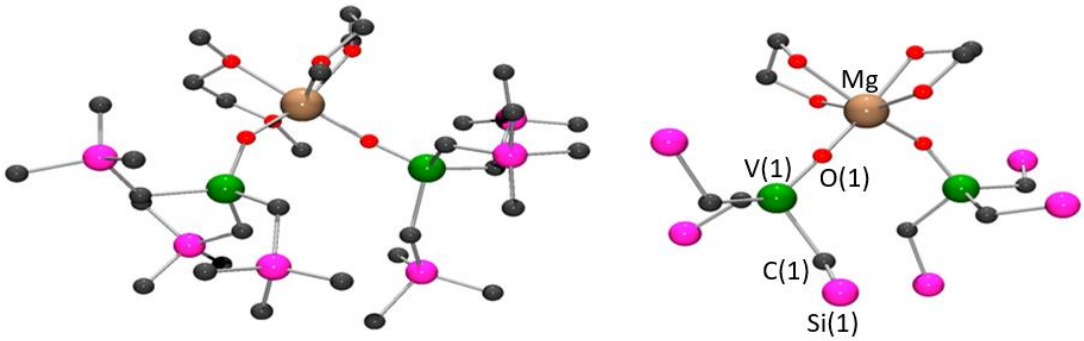

Figure 2.4: Ball and stick crystal structure for $[\{V(CH_2SiMe_3)_3O\}_2Mg(dme)_2]$. Left view: hydrogen atoms omitted for clarity. Right view: hydrogen atoms and methyl groups omitted. Bond lengths and angles are not provided since the structure is only of sufficient quality to establish connectivity.

Complex **3** had previously been characterized by elemental analysis (EA) and electron paramagnetic resonance (EPR) spectroscopy. It is an oil at room temperature, making crystallographic characterization a challenge. Crystals of **3** were obtained from a concentrated solution of hexamethyldisiloxane at –30 °C. The crystals were coated in paratone oil which had been cooled in a –30 °C freezer for 1 hour and transferred to a petri

dish which was cooled in the same fashion. The dish was kept cold within a bucket of dry ice while being transported to the McMaster Analytical X-Ray Diffraction Facility (MAX). A crystal was then selected at low temp and transferred within seconds to the 100 K N_2 cold stream of the X-ray diffractometer. An X-ray crystal structure of **3** has now been obtained (Figure 2.5). The structure consists of a V(IV) metal center with four trimethylsilylmethyl ligands arranged in a tetrahedral fashion. The crystal was twinned, and exhibited whole molecule disorder with approximately 15% of molecules being flipped and shifted half a unit cell along the b axis.

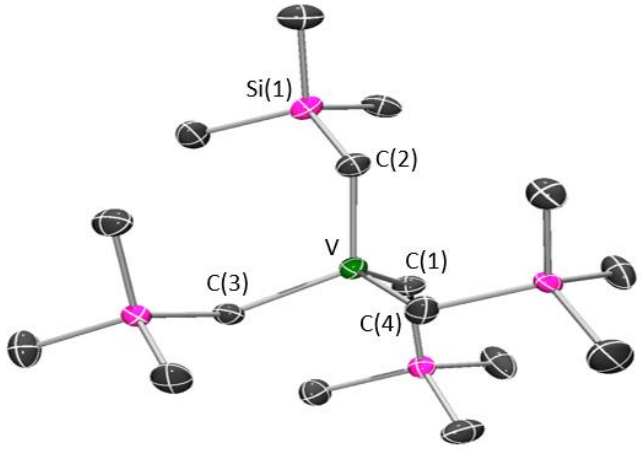

Figure 2.5: X-ray crystal structure of $[V(CH_2CMe_3)_4]$ **(3)** with ellipsoids drawn at 50% probability. Hydrogen atoms are omitted for clarity. Space group *Cc* R_1 = 7.26%. The diagram shows one out of two possible orientations for the structural unit. Bond distances (Å) and angles (°): V–C(1) 2.032(14), V–C(2) 2.011(11), V–C(3) 2.033(11), V–C(4) 2.015(12), C(1)–V–C(2) 116.3(5), C(1)–V–C(3) 105.2(6), C(1)–V–C(4) 106.5(5), C(2)–V–C(3) 106.6(4), C(2)–V–C(4) 106.7(1), C(3)–V–C(4) 115.8(6).

Table 2.2: Selected bond distances and angles for $[Cr(CH_2SiMe_3)_4]$, obtained by Gamboratta *et al.* and reported in 2002 (selected angles combined from two disordered models for CH_2 groups), and selected bond distances and angles for $[V(CH_2SiMe_3)_4]$ **(3)** as obtained at 100 K.

	This work	Gamboratta *et al.*
Equivalent Atom Labels	$[V(CH_2SiMe_3)_4]$ **(3)**	$[Cr(CH_2SiMe_3)_4]$[9]
V–C(1) or Cr–C(1)	2.032(14)	1.983(14)
V–C(2) or Cr–C(2)	2.011(11)	1.954(14)
V–C(3) or Cr–C(3)	2.033(11)	1.958(16)
V–C(4) or Cr–C(4)	2.015(12)	1.972(14)
C(1)–V–C(2) or C(1)–Cr–C(2)	116.3(5)	113.7(6)
C(1)–V–C(3) or C(1)–Cr–C(3)	105.2(6)	107.4(7)
C(1)–V–C(4) or C(1)–Cr–C(4)	106.5(5)	107.3(6)
C(2)–V–C(3) or C(2)–Cr–C(3)	106.6(4)	108.1(7)
C(2)–V–C(4) or C(2)–Cr–C(4)	106.7(1)	108.9(6)
C(3)–V–C(4) or C(3)–Cr–C(4)	115.8(6)	111.6(6)

Complex **3** is extremely air and moisture sensitive, undergoing minor decomposition upon contact with NMR glassware. Thermal stability tests for complex **3** yielded negative results. After heating at 60 °C for 24 hours, solid complex **3** had completely decomposed to a brown oil which mainly consisted of TMS judged by ^1H NMR spectroscopy (Figure 2.6).

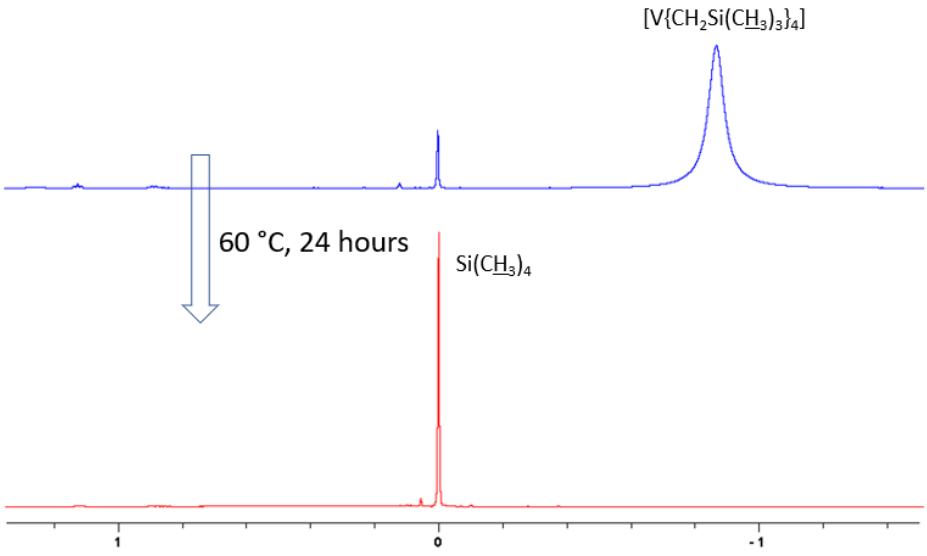

Figure 2.6: ^{1}H NMR spectra (C_6D_6, 600 MHz) of [V(CH_2SiMe_3)$_4$] **(3)** before heating (top, blue) and after heating at 60 °C for 24 hours (bottom, red).

2.4.3 Synthesis and Investigation of [$W_2(CH_2SiMe_3)_6$] (5) and [$Mo_2(CH_2SiMe_3)_6$] (6)

Diamagnetic complexes **(5)** and **(6)** were first prepared by Wilkinson *et al.* in 1972, through the reactions of WCl_5 and $MoCl_5$ with the Grignard reagent Me_3SiCH_2MgCl (Scheme 2.5). In the current work, complexes **5** and **6** were synthesized via modified literature procedures and obtained in 18 and 13% yields, respectively. In the reported procedure the crude products are purified via column chromatography using cellulose (for **5**) or alumina (for **6**) stationary phases, with the type of alumina (neutral, basic, acidic) not specified. Purification of **6** using a basic alumina column was first attempted, on a microscale. Due to a significant difference in retention factors between the product (an orange band which elutes first) and impurities (a brown band which elutes last), a basic alumina plug was used for the purification of the bulk sample. Compound **5** was purified

in the same manner. Both complexes required no further purification upon passing through the alumina plug. Volatility was not investigated since both compounds are reported to sublime at 120 °C (5 mTorr).

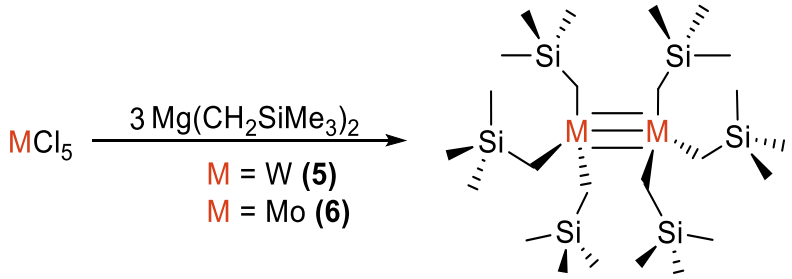

Scheme 2.5: Synthesis of $[W_2(CH_2SiMe_3)_6]$ **(5)** and $[Mo_2(CH_2SiMe_3)_6]$ **(6).**

Heating both **5** and **6** at 150 °C resulted in the orange solids turning brown within 2 hours. ^{1}H NMR spectroscopy revealed that both complexes had completely decomposed to yield free TMS (Figure 2.7).

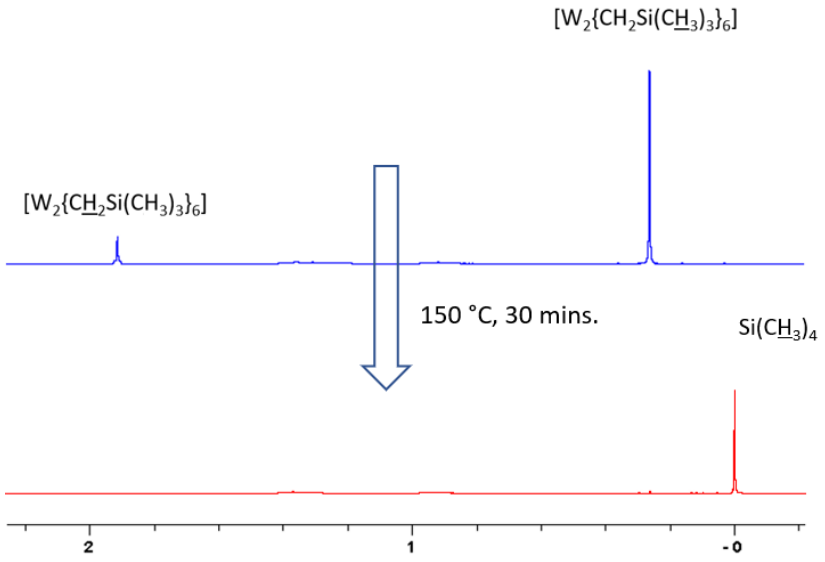

Figure 2.7: ^{1}H NMR spectra (C_6D_6, 600 MHz) of $[W_2(CH_2SiMe_3)_6]$ **(5)** before heating (top, blue) and after heating at 150 °C for 30 minutes (bottom, red).

2.5 Phosphine Appended Metal Alkyl Complexes

The less-than-ideal thermal stability exhibited by all the previously mentioned homoleptic transition metal alkyl complexes led to the investigation of heteroleptic transition metal alkyl complexes bearing 1,2-bis(dimethylphosphino)ethane ligands. The electron donation from L-type phosphine ligands should help stabilize electron deficient metal centers. Also, occupancy of additional coordination sites has been proven to enhance thermal stability by preventing certain low energy decomposition pathways (*vide supra*). The envisioned reactivity is analogous to that of the homoleptic complexes, occurring at the alkyl ligands, with the neutral phosphine ligands dissociating from the metal center upon reduction of the metal.

2.5.1 Synthesis and study of $[Cr(Me)_2(dmpe)_2]$ (7)

Wilkinson and Girolami synthesized a series of early to mid first row-transition metal chloro- phosphino- complexes including $[MCl_2(dmpe)_2]$ (M= Ti, V, Cr, Mn, Fe).[154] $[Cr(dmpe)_2Cl_2]$ can be easily accessed from the reaction of $CrCl_2$ and dmpe as large green crystals, in high yield (Scheme 2.6).

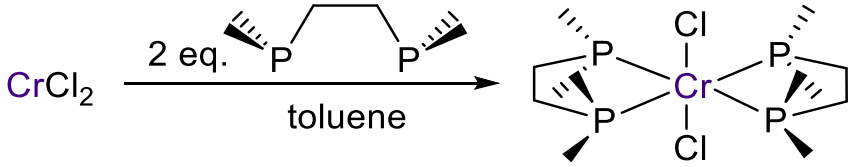

Scheme 2.6: Synthesis of $[Cr(dmpe)_2Cl_2]$.

Alkyl complex **6** was synthesized through the reaction of $[Cr(dmpe)_2Cl_2]$ and methyllithium (Scheme 2.7). The published procedure reports the use of 2 equivalents of

methyllithium in the synthesis.[21] However, when the reaction was carried out, an excess of methyllithium was required to push the reaction to completion. This is likely due to the insolubility of the solid methyllithium which was used, as opposed to a freshly prepared methyllithium solution as stated in the original article.

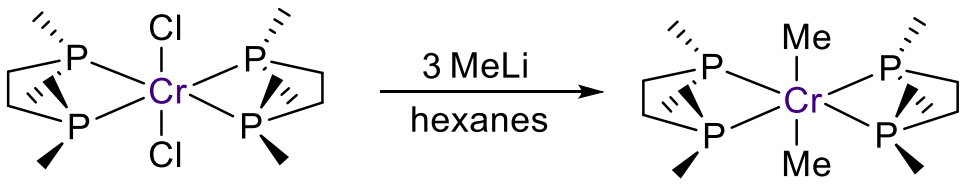

Scheme 2.7: Synthesis of $[Cr(dmpe)_2(Me)_2]$ **(7).**

The volatility and thermal stability of paramagnetic **7** were evaluated. The orange-red complex sublimes without decomposition at 100 °C (5 mTorr). Moderate decomposition was observed when a solution of the complex in C_6D_6 was heated to 140 °C for 3 days, judged by the appearance of ethane by ^{1}H NMR spectroscopy (Figure 2.8).

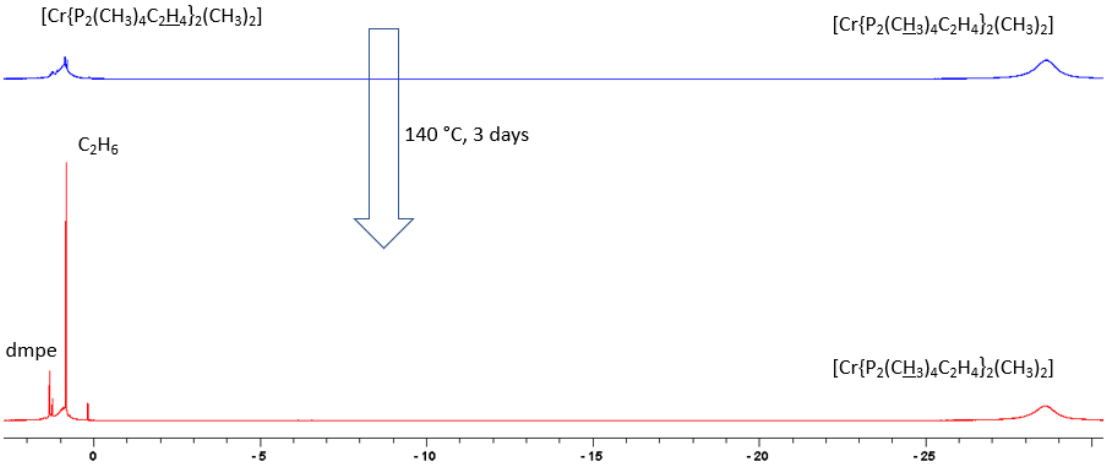

Figure 2.8: ^{1}H NMR spectra (C_6D_6, 600 MHz) of $[Cr(dmpe)_2(Me)_2]$ **(7)** before heating (top, blue) and after heating at 140 °C for 3 days (bottom, red).

The generation of ethane can be rationalized by either bond homolysis to generate methyl radicals, or reductive elimination (bi-molecular or intramolecular, Scheme 2.8). Bi-molecular reductive elimination may take place between two $[Cr(dmpe)_2(Me)_2]$ molecules to yield 2 equivalents of $[Cr(dmpe)_2(Me)]$ and 1 equivalent of ethane. $[Cr(dmpe)_2(Me)]$ may once again undergo bimolecular reductive elimination, releasing another equivalent of ethane, and freeing the neutral dmpe ligands (observable by ^1H NMR spectroscopy). The other pathway involves isomerization of $[Cr(dmpe)_2(Me)_2]$ (only the trans isomer is present in solution by NMR, and Wilkinson reported that the complex selectively crystallizes in the trans configuration), so that concerted intramolecular reductive elimination can take place between cis methyl ligands.

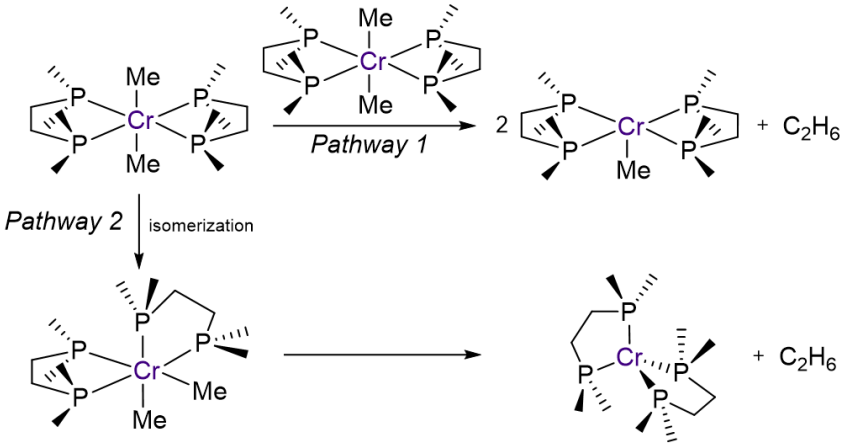

Scheme 2.8: Pathways leading to the thermal decomposition of $[Cr(dmpe)_2(Me)_2]$ **(7)** to ethane and dmpe. Pathway 1: bimolecular reductive elimination to form an unstable $[Cr(dmpe)_2(Me)]$ species which will undergo further bimolecular reductive elimination. Pathway 2: isomerization from a trans to cis isomer followed by reductive concerted elimination.

If chromium metal is indeed formed in the thermal decomposition of $[Cr(dmpe)_2(Me)_2]$, then this complex could make for an effective CVD precursor, which may be used for the deposition of metallic chromium films via thermal decomposition upon a heated substrate. Chromium metal CVD is typically achieved using a simple system of $Cr(C_6H_6)_2$ with a reactive H_2 carrier gas.[155] However, films deposited using bis(benzene)chromium contain significant carbon impurities unless they are deposited at or near atmospheric pressure; conditions which typically lead to poor film uniformity and low growth rates.[155]

2.6 Chapter Summary, Conclusions, and Future Work

While all the alkyl complexes synthesized and evaluated in this chapter were volatile and could be sublimed at 5 mTorr without decomposition, they lacked the thermal stability on a long timescale to be effective as ALD precursors in a typical ALD reactor, assuming that a delivery temperature 40 °C higher than the sublimation temperature at 5 mTorr will be required (Table 2.3). The crystal structure of $[V(CH_2SiMe_3)_4]$ **(3)** has now been reported, as well as an alternative crystal structure for $[Cr(CH_2CMe_3)_4]$ **(2)**. A unique structure, $[\{V(CH_2SiMe_3)_3O\}_2Mg(dme)_2]$ **(4)**, which features a Mg bridged divanadium oxo species was crystallographically characterized and identified as an intermediate in the synthesis of complex **3**. Slightly modified preparations for $[M_2(CH_2SiMe_3)_6]$ (M = Mo **(5)**, W **(6)**) and $[V(CH_2SiMe_3)_4]$ **(3)** are reported. $[Cr(dmpe)_2(Me)_2]$ **(7)** has been shown to sublime without decomposition at 100 °C, and while it may not be useful for ALD due to its long term thermal instability at the anticipated ALD bubbler temperature (≈140 °C), it

could potentially find use as a novel CVD precursor (using a CVD reactor operating at a lower pressure, which would permit a lower bubbler temperature), if it does in fact undergo thermal decomposition to afford metallic chromium.

All homoleptic transition metal alkyl complexes (**1**, **2**, **3**, **5**, **6)** should be analyzed by TGA in order to study their thermal behaviour accurately. A more analytical approach may reveal that one or more of these complexes do in fact possess sufficient thermal stability for ALD.

Given the suggested decomposition route of $[CrMe_2(dmpe)_2]$ **(7)** (*vide supra*), efforts should be made to characterize the thermal decomposition product. If the process leads to the deposition of pure chromium metal, CVD experiments should be undertaken. Related work may also be translated to vanadium if proven successful with chromium, given that no CVD methods for vanadium metal currently exist, and that $[VMe_2(dmpe)_2]$[154] is a known compound.

Synthesis of homoleptic transition metal alkyl complexes with bulkier alkyl or related ligands such as supersilyl ligands ($–Si(SiMe_3)_3$) should be attempted, since this may improve the thermal stability of the resulting complexes by sterically inhibiting certain thermal decomposition pathways. However, these hypothesized complexes may prove to be insufficiently volatile, given that $[Cr(CH(SiMe_3)_2)_3]$,[138] which features ligands more bulky than $–CH_2SiMe_3$ ligands, undergoes thermal decomposition upon heating to 80 °C prior to sublimation.

Table 2.3: Summary of yield, volatility, and thermal stability of metal alkyl precursors.

Complex	Yield	Sublimation Temp. (5 mTorr)	Thermal Stability†
$[Cr(CH_2SiMe_3)_4]$ **(1)**	29%	25 °C	Major decomposition
$[Cr(CH_2CMe_3)_4]$ **(2)**	38%	40 °C	Complete decomposition
$[V(CH_2SiMe_3)_4]$ **(3)**	17%	25 °C	Major decomposition
$[W_2(CH_2SiMe_3)_6]$ **(5)**	18%	120 °C	Complete decomposition
$[Mo_2(CH_2SiMe_3)_6]$ **(6)**	15%	120 °C	Complete decomposition
$[Cr(dmpe)_2(Me)_2]$ **(7)**	72%	100 °C	Moderate decomposition

†At a temperature 40 °C higher than the sublimation temperature (5 mTorr), over the prescribed time period (up to 3 days).

Chapter 3 – Homoleptic Transition Metal Allyl Complexes

3.1 Introduction to Homoleptic Transition Metal Allyl Complexes

Allyl ligands are some of the smallest π-delocalized ligands in organometallic chemistry.[156] The ligand can interact with transition metals via either η^3- or η^1-coordination (Figure 3.1). Due to the compact size, the interconversion between these two bonding modes can be rapid.[156] Homoleptic allyl transition metal complexes are notoriously thermally unstable, owing to the fact that they are typically coordinately unsaturated, allowing several low-energy decomposition pathways to be accessed.[156] Examples include $[Fe(C_3H_5)_3]$ and $[Co(C_3H_5)_3]$ which both decompose above –40 °C, as well as $[V(C_3H_5)_3]$ which is explosive above –30 °C.[157]

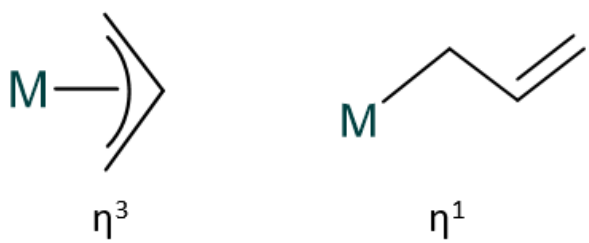

Figure 3.1: η^3- and η^1- bonding modes for allyl ligands.

As mentioned previously, sterically bulky ligands which block decomposition routes through the occupancy of the metal coordination sphere vastly improve the kinetic stability of organometallic complexes. This can be demonstrated by the substituted cyclopentadienyl ligands C_5Me_5[158] and $C_5H_3(SiMe_3)_2$,[159] which have been used to synthesize compounds with far greater thermal stability than those of unsubstituted Cp ligands. This same principle has been applied to allyl ligands.

Alkyl, aryl, silyl, and siloxide groups have all been used as substituents on allyl ligands.[156] In bis(allyl) complexes, the allyl ligands can be found in staggered or eclipsed configurations (Figure 3.2, top), where interconversion by rotation about the M–allyl bond axis is possible. Substituents which are cis to the meso hydrogen on the central allylic carbon are in a syn-position, while those which are trans to the meso hydrogen are in an anti-position (Figure 3.2, bottom).

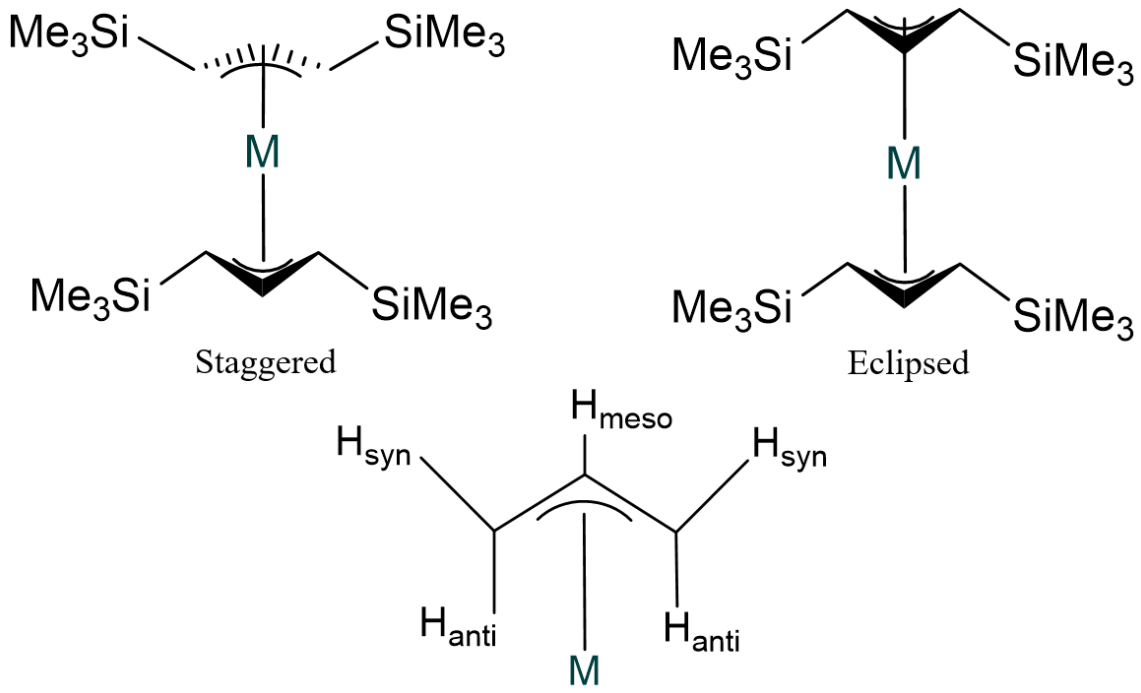

Figure 3.2: Staggered and eclipsed configurations of bis(allyl) complexes (top) and nomenclature for position of the substituents on the ligand (bottom).

In the 1990s, Fraenkel reported the syntheses of lithiated derivatives of $[(SiMe_3)_nC_3H_{5-n}]^-$ anions.[160–162] The trimethylsilyl groups provided a substantial increase in the size and steric demands of the ligands (the *syn*, *syn*-$[1,3\text{-}(SiMe_3)_2C_3H_3]^-$ anion has a space-filling model volume 4 times larger than the $[C_3H_5]^-$ parent ion[156]). This provided

drastic changes in the reactivity and thermal stability of the associated complexes, allowing these and related variants to become the most extensively studied types of ligands in bulky allyl complex chemistry.[156] The differences in reactivity and thermally stability are greatly apparent when comparing pyrophoric $[Ni(C_3H_5)_2]$, versus $[Ni\{1,3\text{-}(SiMe_3)_2C_3H_3\}_2]$ which only slowly decomposes in air (hours–days).[163]

The starting materials for the preparation of $[M\{1,3\text{-}(SiMe_3)_2C_3H_3\}_2]$ complexes are most commonly the potassium salts of the allyl ions. These reagents are prepared from the lithium salts that are generated from reaction of the substituted propene and alkyllithium reagents (Scheme 3.1; 1st reaction arrow).[164] Lithium halide salts are readily solvated by ether; therefore it is common practice to replace the lithium cation with a potassium cation prior to reaction with the metal halide starting material (during the synthesis of the $[M\{1,3\text{-}(SiMe_3)_2C_3H_3\}_2$ complex) to facilitate the separation of the alkali metal halide by-product via filtration (Scheme 3.1; 2nd reaction arrow).

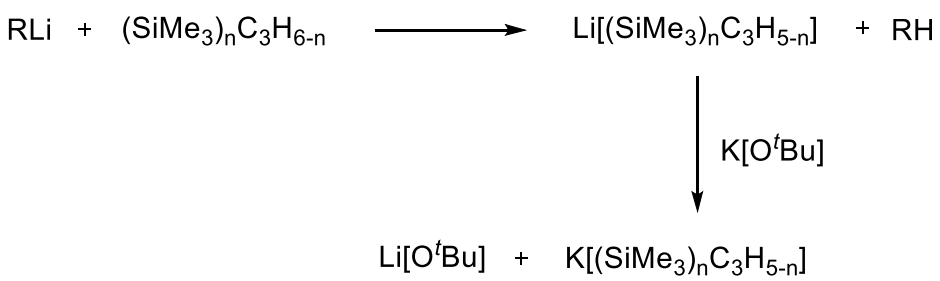

Scheme 3.1: Synthesis of $K[(SiMe_3)_nC_3H_{5-n}]$, the typical starting material for the preparation of transition metal $[M\{1,3\text{-}(SiMe_3)_2C_3H_3\}_2]$ complexes.

3.2 Homoleptic Transition Metal Allyl Complexes as ALD Precursors

To the best of our knowledge, there are no elemental metal ALD processes which utilize homoleptic allyl complexes, and the only example which uses a precursor bearing an allyl ligand is the deposition of metallic cobalt using [^{t}Bu–AllylCo(CO)$_3$] and dimethylhydrazine (Scheme 3.2).[70]

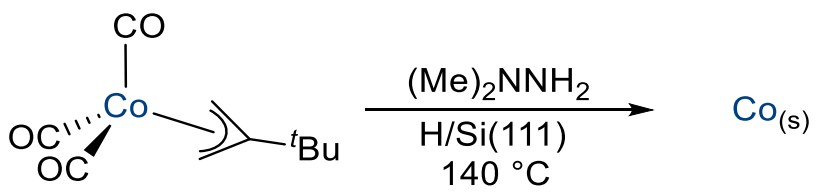

Scheme 3.2: General reaction scheme for the ALD of metallic cobalt using a [(^{t}Bu–Allyl)Co(CO)$_3$] precursor and dimethylhydrazine co-reactant.

Generally, OH-terminated substrates are more reactive than H-terminated silicon surfaces, based on the higher reactivity of hydroxyl groups with metal precursors.[165] An interesting feature of this Co ALD process is that the reverse is true, the [(^{t}Bu–Allyl)Co(CO)$_3$] precursor is substantially more reactive with H-terminated Si substrates than OH-terminated SiO_2 substrates.[165] No deposition was observed on SiO_2 surfaces bearing reactive hydroxyl sites at 140 °C, while ~ 1 monolayer of cobalt was deposited after the first precursor pulse on H-terminated Si.[165] Authors calculated the atomistic details and reaction energetics of the nucleation step with [(^{t}Bu–Allyl)Co(CO)$_3$] towards H/Si(111) versus OH/SiO_2 using density functional theory (DFT).[165] The proposed scheme involves oxidative addition of a surface Si–H bond, accompanied by rearrangement of the allyl ligand from an η^3- to a η^1- coordination mode (Scheme 3.3).[165] The resulting

hydride ligand then undergoes reductive elimination with the allyl ligand to yield the final surface-bound complex (surface-Si)–Co(^{t}BuMeC=CH_2)$(CO)_3$.[165]

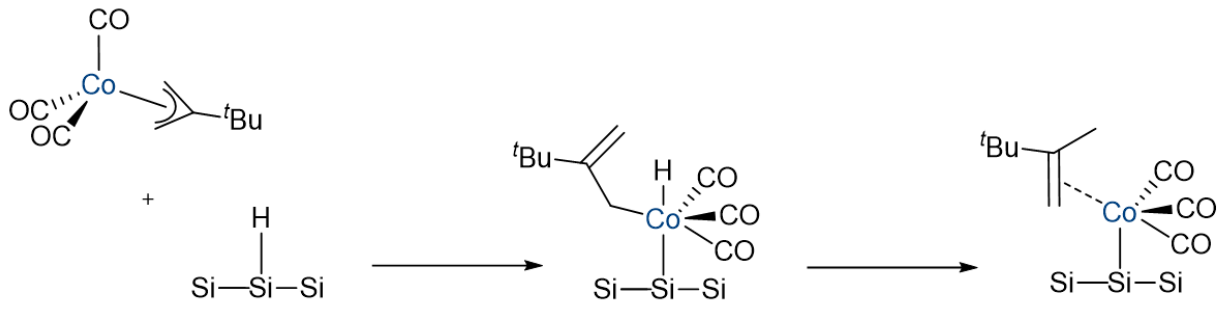

Scheme 3.3: Reaction scheme for the formation of Co–Si bonds on H/Si(111) during the nucleation of Co ALD using [(^{t}Bu–Allyl)Co$(CO)_3$].

The only other report of any class of ALD (oxide, fluoride, nitride, etc.) which utilizes metal precursors bearing allyl ligands is the deposition of molybdenum oxide from [{$(SiMe_3)C_5H_4$}Mo$(CO)_2$(η^3-2-methylallyl)] and ozone.[166]

3.3 Homoleptic Transition Metal Allyl Complexes

Reactivity of [M{1,3-bis(trimethylsilyl)allyl}$_2$] complexes with hydridic reagents should closely mirror that of the homoleptic metal alkyl complexes discussed previously. For example, allyl complexes may react with H_2 or $PhSiH_3$ via σ-bond metathesis, or oxidative addition immediately followed by reductive elimination, to yield an allyl hydride complex through elimination of 1,3-$(SiMe_3)_2C_3H_3E$ (E = H or $PhSiH_2$; Scheme 3.4). The resulting allyl hydride complex can then reductively eliminate one equivalent of $(Me_3Si)HC{=}CH{–}CH_2SiMe_3$ to yield elemental metal.

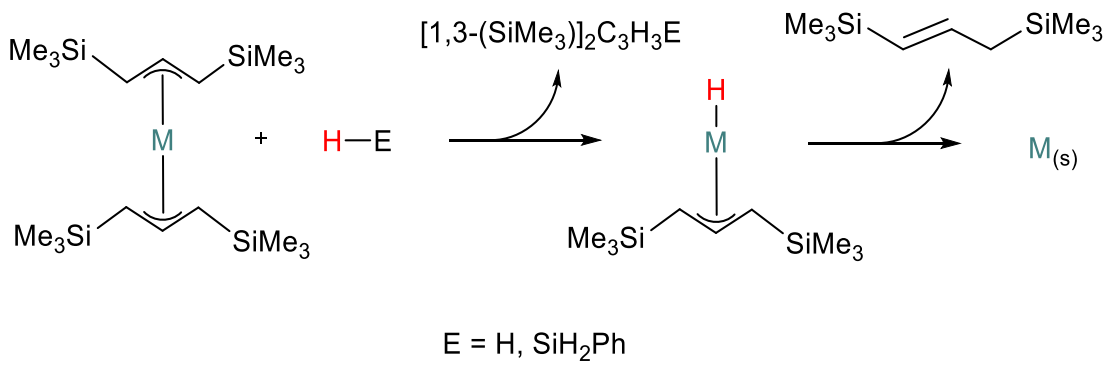

Scheme 3.4: Envisioned reactivity between a [M{1,3-bis(trimethylsilyl)allyl}$_2$] metal precursor and phenylsilane or molecular hydrogen.

Other potential co-reagents which could be used to obtain metallic films from homoleptic allyl precursors include BEt_3 and $AlEt_3$. The mechanisms of these reactions would be mostly analogous to those involving $ZnEt_2$ (**1.7.5**), which would be initiated with ligand transfer between the metal precursor and BEt_3 or $AlEt_3$ to yield [M(Et){1,3-bis(trimethylsilyl)allyl}], followed by β-hydride elimination to afford [MH{1,3-bis(trimethylsilyl)allyl}] with corresponding release of ethylene.

3.3.1 Synthesis and Investigation of [M{1,3-bis(trimethylsilyl)allyl}$_2$] M = Ni (8), Cr (9), Co (10)

[Ni{1,3-bis(trimethylsilyl)allyl}$_2$] is the only complex in this series that was synthesized from a starting material different than MCl_2. Hanusa reported that initial attempts at synthesis using $NiCl_2$ resulted in the isolation of the dimerized ligand: 1,3,4,6-tetrakis(trimethylsilyl)-1,5-hexadiene (Scheme 3.5).[163] Similar results were observed from $NiBr_2$ and NiI_2 starting materials. It was suggested that oxidative coupling of the allyl ion was likely occurring at the surface of the mostly insoluble nickel reagents, as coupling of

allyl ligands on a nickel center has been reported previously.[58] To avoid coupling reactions, [$NiBr_2$(dme)] was used as a much more soluble nickel halide reagent.[163]

Scheme 3.5: Oxidative coupling of allyl ligands on Ni surfaces to form 1,3,4,6-tetrakis(trimethylsilyl)-1,5-hexadiene.

[M{1,3-bis(trimethylsilyl)allyl}$_2$] M = Ni **(8)**, Cr **(9)**, Co **(10)** were each synthesized according to literature procedures.[163,167,168] Compound 8 is diamagnetic, whereas compounds 9 and 10 are paramagnetic. It was difficult to obtain a very pure sample of complex **8** as a small amount of the oxidative coupling by-product (1,3,4,6-tetrakis(trimethylsilyl)-1,5-hexadiene) was always present. The reported sublimation temperature of the organic by-product is 55 °C, so fractional sublimation was attempted at room temperature wherein the nickel complex is readily sublimable. After two repeat sublimations at room temperature the amount of by-product was significantly diminished, but small amounts were still present (Figure 3.3). The complex is extremely soluble in a wide range of solvents (THF, hexanes, toluene, benzene, hexamethyldisiloxane) which made recrystallization attempts from cooled concentrated solutions very low yielding. Complex **8** is present in solution as both eclipsed and staggered configurations, with each

exhibiting two resonances for their trimethylsilyl groups, consistent with syn and anti arrangements of the $SiMe_3$ groups.

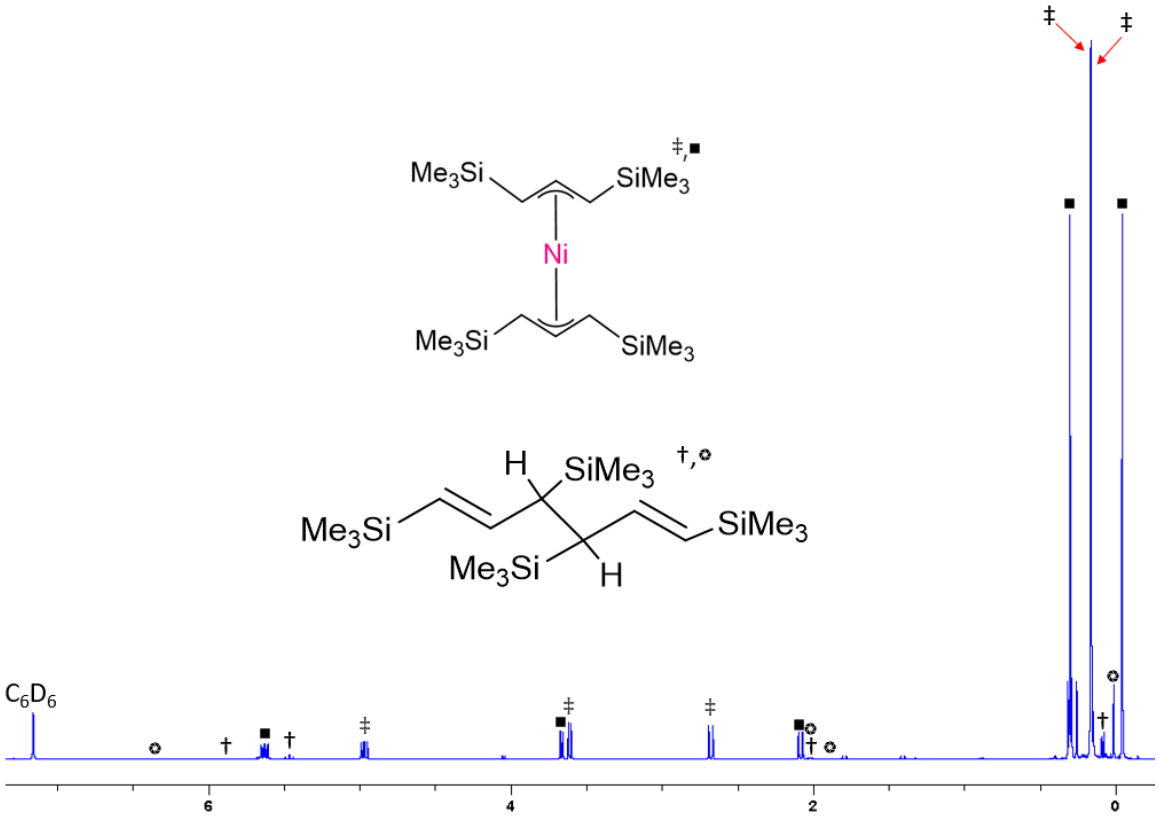

Figure 3.3: ^{1}H NMR spectrum (C_6D_6, 600 MHz) of Ni[1,3-bis(trimethylsilyl)allyl]$_2$ after two sublimations at 25 °C in an attempt to separate the complex from (1,3,4,6-tetrakis(trimethylsilyl)-1,5-hexadiene).

Chromium complex **9** was synthesized from $CrCl_2$ and $K[C_3(SiMe_3)_2H_3]$.[167] The product was again purified by sublimation, and PXRD was used to assess the purity of the sample. The acquired diffractogram did not match the pattern which was calculated from the reported single crystal X-ray structure using Mercury (Figure 3.4). The sole reported crystal structure of the complex has the allyl ligands in a staggered configuration with syn,

anti-trimethylsilyl substituents. The lack of agreement between the experimental and calculated powder diffraction patterns may be an indication of very impure product. However, a more likely explanation is that sublimation yields a mixture of syn and anti (or eclipsed and staggered) products, complicating the powder X-ray diffraction pattern.

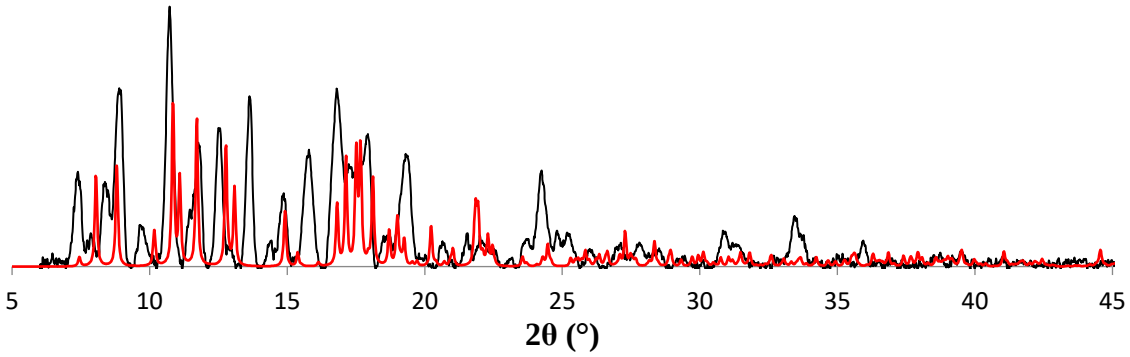

Figure 3.4: Predicted powder X-ray diffractogram of staggered syn, anti [Cr{1,3-bis(trimethylsilyl)allyl}$_2$] (red) overlaid with acquired powder X-ray diffractogram of [Cr{1,3-bis(trimethylsilyl)allyl}$_2$] purified by sublimation (black).

Cobalt complex **10** was synthesized in the same manner, following literature procedures, and purified by sublimation at 50 °C.[168] While the colour and sublimation temperature of the complex aligned with what has been reported, once again the acquired powder diffractogram did not match the calculated pattern for the staggered syn, anti configuration of the product (Figure 3.5).

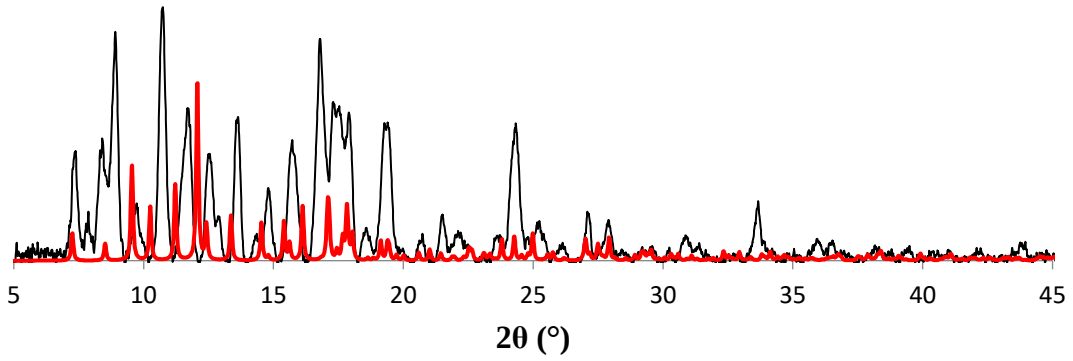

Figure 3.5: Predicted powder X-ray diffractogram of staggered syn, anti [Co{1,3-bis(trimethylsilyl)allyl}$_2$] (red) overlaid with observed powder X-ray diffractogram of [Co{1,3-bis(trimethylsilyl)allyl}$_2$] purified by sublimation (black).

The chromium[167] and nickel[163] complexes are reported to be thermally robust and stable at 100 and 110 °C in solution, respectively, although a timescale was not specified. Since they are both volatile below 60 °C they should be well suited for ALD delivery. Solution-state reactivity of all complexes towards $AlEt_3$, $PhSiH_3$, and BEt_3 was investigated. Four 10 mg samples of each complex were dissolved in approximately 2 mL of toluene, then placed into vials. Three of the four samples of each complex were individually treated with 5 equivalents of either $AlEt_3$, $PhSiH_3$, or BEt_3. Meanwhile, one sample of each complex was left as a blank to be heated alongside the others, ensuring that observations were based on reactivity and not thermal instability. All samples were simultaneously heated in a VWR aluminum block heater, with temperatures held constant for 30 minutes at each temperature (room temp., 50, 75, and 100 °C) before increasing to the next level. Observations were made at the end of the 30-minute period, except in cases

where changes occurred immediately upon addition of the co-reactant. While some promising reactivity was observed (e.g. appearance of a metallic looking film on the vial containing nickel complex **8** and BEt_3 upon heating to 100 °C, or a black solid in the vial containing cobalt complex **10** and BEt_3 upon heating to 100 °C), these results were somewhat negated by observed changes which took place in the blank samples concurrently (Table 3.1).

Table 3.1: Observations for the solution-state reactivity of homoleptic allyl complexes **(8)**, **(9)**, and **(10)** towards $AlEt_3$, BEt_3 and $PhSiH_3$.

		$[Ni(allyl^{TMS2})]_2$ **(8)**	$[Cr(allyl^{TMS2})]_2$ **(9)**	$[Co(allyl^{TMS2})]_2$ **(10)**
	Initial	Orange-red	Deep red sol'n	Orange-red
$AlEt_3$	Rt	Brown yellow after 1hr	No change	Brown immediately
	50 °C	Brown yellow	No change	Brown
	75 °C	Brown yellow	Brown	Near black
	100 °C	Brown	Brown	Black
BEt_3	Rt	No change	No change	No change
	50 °C	No change	No change	No change
	75 °C	Brown/yellow	Deep red/brown	Dark orange brown
	100 °C	Orange yellow, black solid	Deep red/brown	Brown yellow, metallic film
$PhSiH_3$	Rt	No change	No change	Brown sol'n immediately
	50 °C	No change	No change	Brown
	75 °C	Brown	Brown red	Brown
	100 °C	Brown	Brown w/ ppt	Dark brown, near black
Blank	Rt	No change	No change	No change
	50 °C	No change	No change	No change
	75 °C	Brown yellow	Deep red, solid ppt	Yellow brown
	100 °C	Brown yellow, feint metallic film	Red brown, solid ppt	Yellow brown

The thermal stability of the complexes was evaluated to justify the observations shown above. After heating a neat sample of nickel complex **8** at 70 °C for 24 hours, major decomposition was observed, indicated by the appearance of the coupling product (1,3,4,6-

tetrakis(trimethylsilyl)-1,5-hexadiene) by ^{1}H NMR spectroscopy and a metallic film forming on the walls of the J-Young tube. After several days at this temperature, a film thick enough to be analyzed by PXRD was obtained (Figure 3.6). The film was sonicated into the C_6D_6 solution before being collected, washed with hexanes (3x), toluene (1x), and dried. The material matched mainly with nickel metal, aside from one uncharacterized peak at 40 °C.

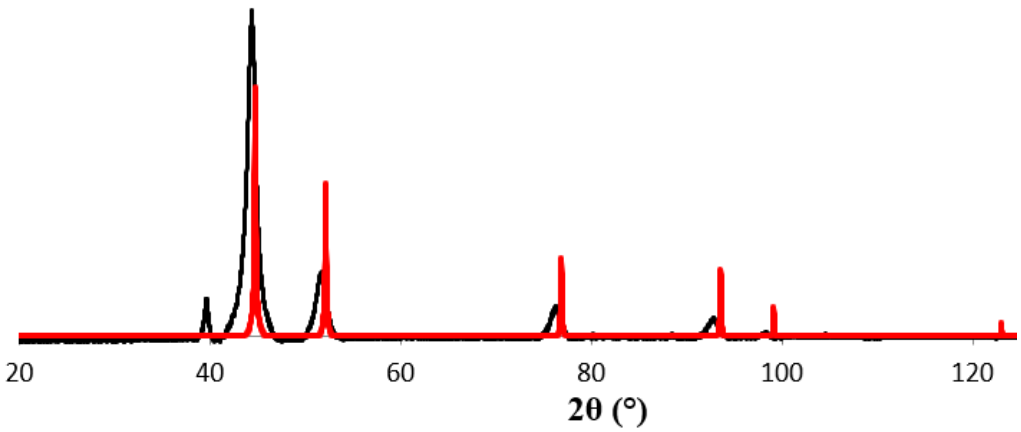

Figure 3.6: Diffractogram of the metallic film deposited during the thermal stability studies of [Ni{1,3-bis(trimethylsilyl)allyl}$_2$] (black). Calculated powder X-ray diffractogram for nickel metal using Mercury (red).

The thermal stability of chromium complex **9** was then assessed (neat; with heating in the absence of solvent). The ^{1}H NMR spectrum provides very little information due to its paramagnetism, making the results difficult to interpret. Nevertheless, the complex was determined to have undergone significant decomposition after heating to 90 °C for 24 hours, evident from the growth of new diamagnetic peaks in the ^{1}H NMR spectrum (Figure 3.7). Close inspection revealed that the main decomposition product was the same coupling

by-product observed during the synthesis of the nickel complex: 1,3,4,6-tetrakis(trimethylsilyl)1,5-hexadiene. The emergence of this organic product can be rationalized as the result of reductive elimination of the two allyl ligands. Heating was continued for 5 days at this temperature, but no solids (either precipitate or film deposition) were observed.

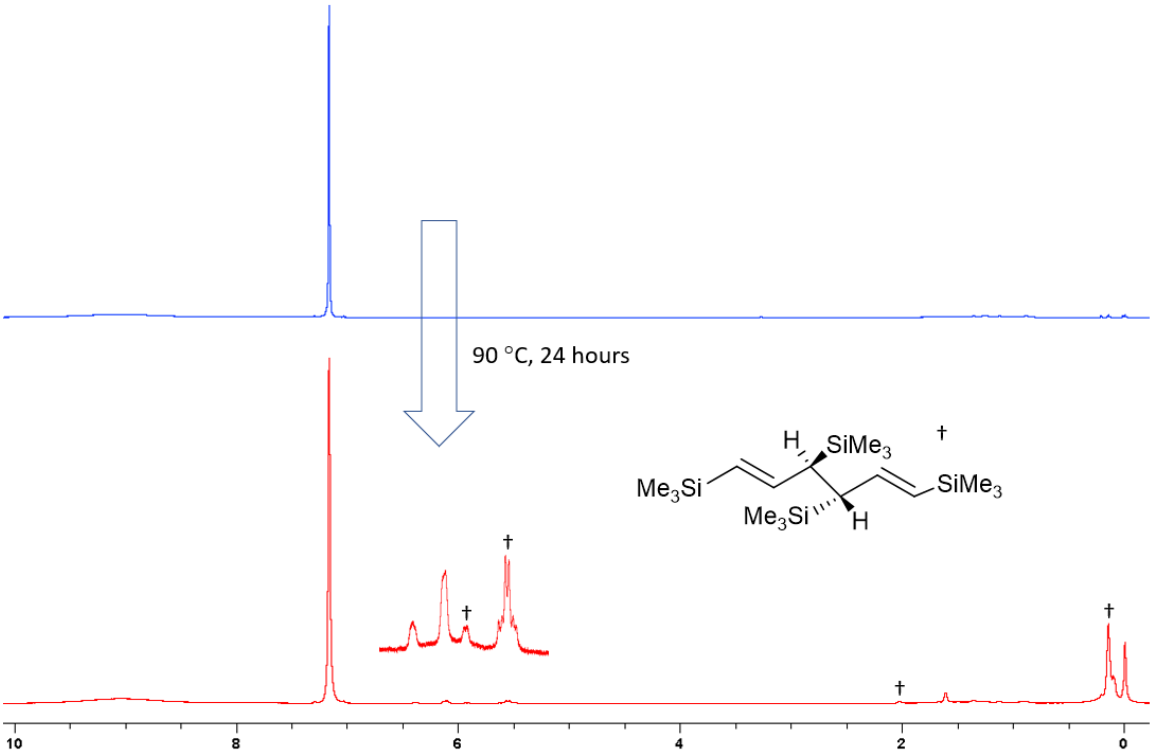

Figure 3.7: ^{1}H NMR spectra (C_6D_6, 600 MHz) of [Cr{1,3-bis(trimethylsilyl)allyl}$_2$] before heating (top, blue) and after heating at 90 °C for 24 hours (bottom, red).

Cobalt complex **10** was deemed thermally unstable after being heated to 90 °C for 24 hours. The red crystals melted upon heating, and the oil produced was dark brown in colour upon completion of the 24 hours period. ^{1}H NMR spectroscopy revealed the same

thermal decomposition by-products as with the chromium analogue: 1,3,4,6-tetrakis(trimethylsilyl)1,5-hexadiene.

3.4 Chapter Summary, Conclusions, and Future Work

While some promising reactivity was observed during solution-state studies of the homoleptic allyl complexes [M{1,3-bis(trimethylsilyl)allyl}$_2$] M = Ni **(8)**, Cr **(9)**, Co **(10)**, it may not be possible to translate this to ALD reactor experiments due to the poor thermal stability displayed by each complex 40 °C above the sublimation temperature (5 mTorr). The deposition of nickel metal during the decomposition of complex **8** suggests that it may be a candidate for nickel metal CVD, contingent upon characterization of the minor unidentified reflection observed by PXRD.

While nickel CVD is easily achievable with [Ni(CO)$_4$][169], the extreme toxicity of nickel tetracarbonyl is a major concern in some industries. Therefore, CVD with [Ni{1,3-(SiMe$_3$)$_2$C$_3$H$_3$}$_2$] should be explored, and may prove useful if effective.

Table 3.2: Summary of yield, volatility, and thermal stability of homoleptic metal allyl precursors.

Complex	Yield	Sublimation Temp. (5 mTorr)	Thermal Stability (24 hours)†
[Ni{1,3-(SiMe$_3$)$_2$C$_3$H$_3$}$_2$] **(8)**	41%	25 °C	Major decomposition
[Cr{1,3-(SiMe$_3$)$_2$C$_3$H$_3$}$_2$] **(9)**	60%	50 °C	Moderate decomposition
[Co{1,3-(SiMe$_3$)$_2$C$_3$H$_3$}$_2$] **(10)**	65%	50 °C	Major decomposition

†At a temperature 45 °C (for **8**) or 40 °C (for **9** and **10**) higher than the sublimation temperature (5 mTorr).

Chapter 4 – Mn(I) Hydrides and Borohydrides

Portions of this section have been adapted with permission from Price, J. S.; DeJordy, D. M.; Emslie, D. J. H.; Britten, J. F. Reactions of $[(dmpe)_2MnH(C_2H_4)]$: Synthesis and Characterization of Manganese(I) Borohydride and Hydride Complexes. *Dalton Trans*. **2020**, asap (DOI:10.1039/D0DT01726D) with permission from The Royal Society of Chemistry.

4.1 Introduction to Mn(I) Hydrides and Borohydrides

The first stable molecular manganese hydride complex to be reported was $[(OC)_5MnH]$, in 1957.[170] The majority of manganese hydride complexes are monovalent, neutral, contain carbonyl co-ligands, and feature an octahedral geometry at the metal center. Monodentate phosphine[171–174] and bidentate bis(phosphine)[175–177] ligands are popular co-ligands which can be found in a number of structurally characterized Mn hydride complexes.

When transition metal hydride complexes are allowed to react with hydroboranes, various bonding motifs can result.[178] Notably, these include bidentate borohydride complexes (an anionic ligand with two hydride moieties bridging between B and the metal centre),[179,180] monodentate borohydride complexes (a hydride bridging between the metal and BHR_2),[181] boryl dihydride complexes (two hydrides and a boryl ligand), and hydroborane hydride complexes (an anionic hydride and a neutral σ-hydroborane ligand) (Figure 4.1a, b, c, d).[182] Typically, borohydride complexes are favoured (over hydroborane hydride complexes) in reactions involving significantly lewis acidic boron centres, while boryl dihydride complexes are favoured in reactions with electron-rich metal centres with a readily accessible oxidation state 2 units higher.[183,184] In some cases, metal hydride

complexes will react with hydroboranes to eliminate H_2, affording boryl or borylene hydride complexes (Figure 4.1e, f). Additionally, structures which feature borohydride moieties bridging between multiple metal centres, and tridentate borohydride ligands have been reported, though the latter are generally prepared *via* reactions with hydroborate salts (Figure 4.1g, h).[185] Prior to this work, the only structurally characterized monometallic examples of bidentate borohydride Mn(I) complexes were two isonitrile carbonyl species reported in 2017 by Figueroa.[186] Additionally, a bridging Mn(I) borohydride complex was reported by Riera in the early 1990s.[187]

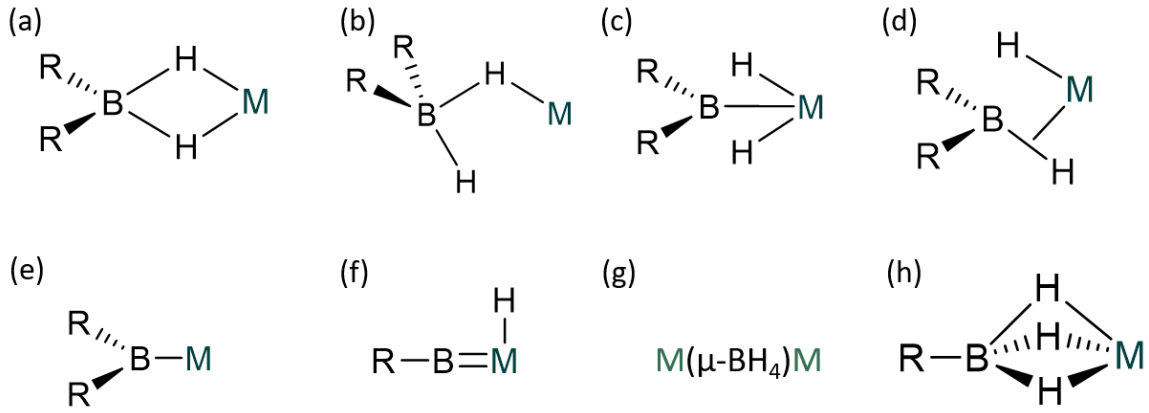

Figure 4.1: Various bonding motifs which may result from reaction of metal hydride complexes and hydroboranes: (a) bidentate borohydride, (b) monodentate borohydride, (c) boryl dihydride, (d) hydroborane hydride, (e) boryl, (f) borylene hydride, (g) bridging borohydride, and (h) tridentate borohydride complexes.

4.1.1 Introduction to $[(dmpe)_2MnH(C_2H_4)]$

Girolami and Wilkinson reported the synthesis of the ethylene hydride Mn(I) complex $[(dmpe)_2MnH(C_2H_4)]$ in the early 1980s.[188] The related complex,

[(dmpe)$_2$MnH(H$_2$)], was also prepared by Wilkinson through the hydrolysis of the AlH$_4$-bridged dimer [(dmpe)$_2$Mn(μ-H)$_2$AlH(μ-H)$_2$AlH(μ-H)$_2$Mn(dmpe)$_2$].[188] A wealth of chemistry was discovered by the Jones group who investigated the reactions of Wilkinson's [(dmpe)$_2$MnH(H$_2$)] with a variety of nucleophiles (CO, N$_2$, isonitriles), observing substitution of the dihydrogen ligand in each case (Scheme 4.1).[189]

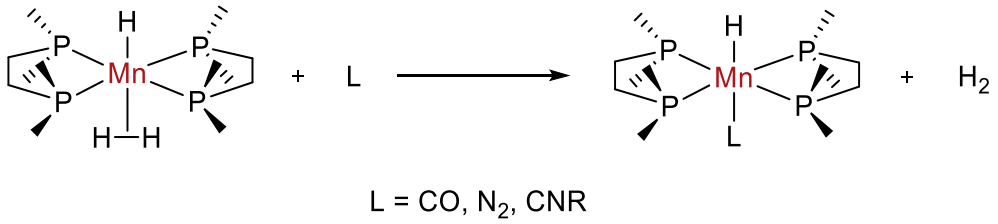

Scheme 4.1: Reactions of [(dmpe)$_2$MnH(C$_2$H$_4$)] with various nucleophiles.

The Emslie group has recently reported reactions of this complex with various hydrosilanes. Reactions with primary hydrosilanes yielded disilyl hydride complexes [(dmpe)$_2$MnH(SiH$_2$R)$_2$] (R = Ph, ^{n}Bu),[190] whereas reactions with secondary hydrosilanes yielded silylene hydride complexes [(dmpe)$_2$MnH(=SiR$_2$)] (R = Ph, Et) as well as the silyl dihydride complex [(dmpe)$_2$MnH$_2$(SiHPh$_2$)] in the case of reaction with H$_2$SiPh$_2$.[191]

These reactions all proceed via initial isomerization of the ethylene hydride complex to a 5-coordinate ethyl species [(dmpe)$_2$MnEt], followed by reactivity to eliminate ethane or an ethylsilane by-product (Scheme 4.2). With the utility of [(dmpe)$_2$MnH(H$_2$)] as a precursor for accessing new manganese-containing species being demonstrated through reactions with hydrosilanes, we set out to investigate reactivity with hydroboranes.

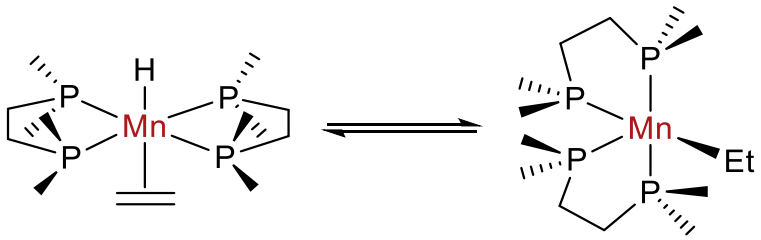

Scheme 4.2: Isomerization of $[(dmpe)_2MnH(C_2H_4)]$ to $[(dmpe)_2MnEt]$.

4.2 Transition Metal Hydride and Borohydride Complexes as ALD and CVD Precursors

To the best of our knowledge, transition metal complexes bearing hydride or borohydride ligands have never been utilized for the growth of thin metal films by ALD. However, there are various examples of borohydride complexes being used as CVD precursors for the deposition of metal boride thin films.

Group 4 diborides, MB_2 (M = Ti, Zr, Hf) have the desirable properties of high hardness, high melting point, moderate strength, resistance to wear and corrosion, and good electrical conductivity.[192] This makes them ideal coatings for metal cutting tools, and coatings for rocket nozzles in the aerospace industry.[193] Transition metal tetrahydroborates are used as CVD precursors for depositing metal borides (Figure 4.2). They are often volatile, and their known thermal decomposition route releases hydrogen and variable amounts of diborane under mild conditions. Low temperature (200 °C) and pressure (10^{-4} Torr) CVD of TiB_2 films was achieved using a $[Ti(BH_4)_3(dme)]$ precursor. The complex sublimes readily without decomposition at 25 °C under vacuum, and AES analysis of the resultant films revealed that titanium and boron were present in a ratio of 1:2.07. Zirconium and hafnium diboride films were prepared in a similar manner using homoleptic

$[M(BH_4)_4]$ complexes, though these required slightly higher temperatures to achieve deposition (250 °C).[194]

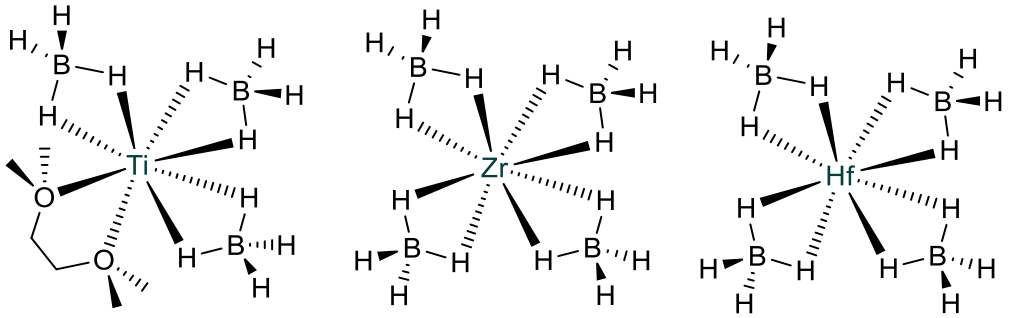

Figure 4.2: Selected CVD precursors for the deposition of MB_2 films.

4.3 Synthesis and Investigation of $[(dmpe)_2Mn(\mu\text{-}H)_2BH_2]$ (11)

Reaction of $[(dmpe)_2MnH(C_2H_4)]$ with the trimethylamine adduct of borane generated the borohydride complex $[(dmpe)_2Mn(\mu\text{-}H)_2BH_2]$ **(11)**, with the corresponding release of ethylene and free NMe_3 by-products (Scheme 4.3). This reactivity contrasts the previously observed mechanism of reaction with hydrosilanes (which proceed via isomerization to a 5-coordinate ethyl intermediate, with subsequent release of ethane or an ethylsilane by-product), instead involving straightforward ethylene elimination. The previously reported aluminum analogue of complex **11,** $[(dmpe)_2Mn(\mu\text{-}H)_2AlH(\mu\text{-}H)_2AlH(\mu\text{-}H)_2Mn(dmpe)_2]$,[188] is a dimer involving 5-coordinate aluminum centers, while complex **11** is monometallic. The purple solid can be sublimed at 80 °C (5 mTorr), and as such was investigated as a potential CVD precursor.

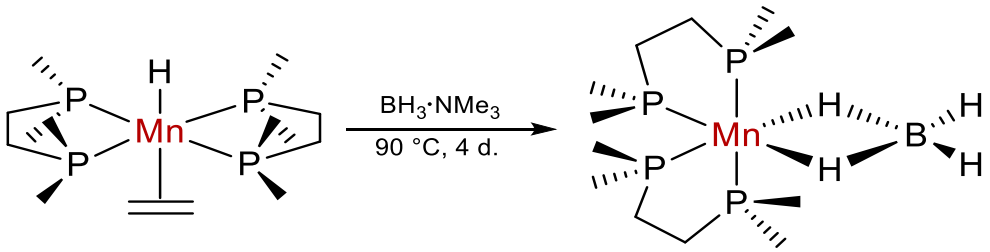

Scheme 4.3: Synthesis of $[(dmpe)_2Mn(\mu\text{-}H)_2BH_2]$ **(11)**.

Upon heating the solid at 120 °C for 48 hours, moderate decomposition was observed. The signals within the alkyl region of the ^{1}H NMR spectrum had all been broadened, while a new signal (–15.7 ppm, † in Figure 4.3) appeared in the hydride region at slightly higher frequency than the $Mn(\mu\text{-}\underline{H})_2BH_2$ signal.

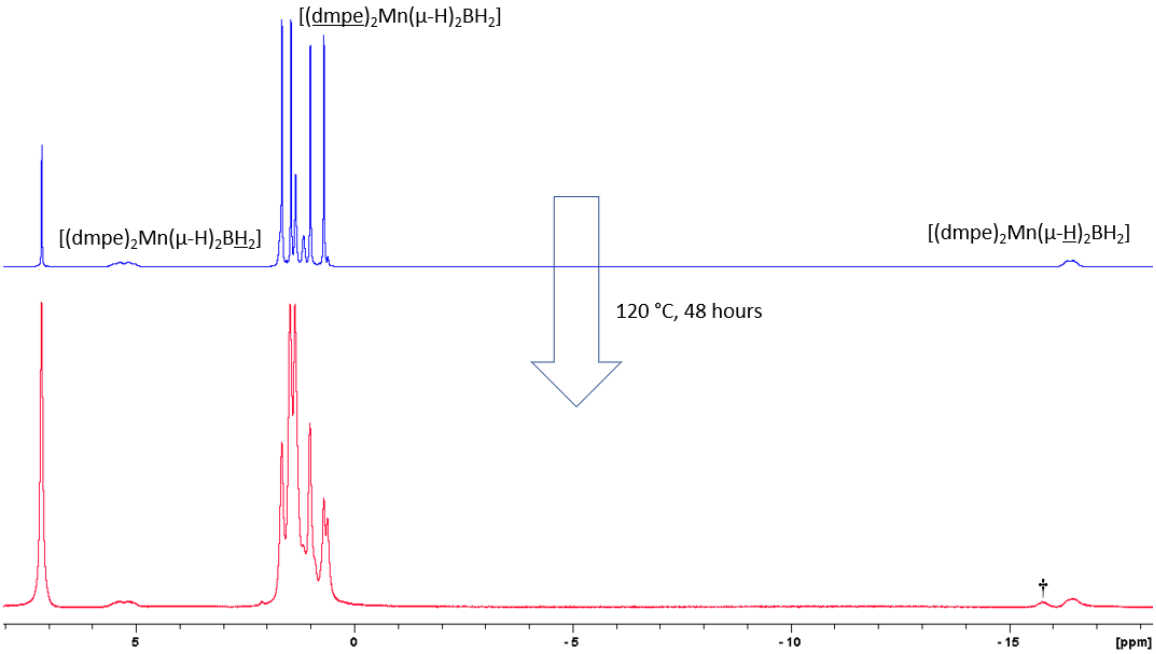

Figure 4.3: ^{1}H NMR spectrum (C_6D_6, 600 MHz) of $[(dmpe)_2Mn(\mu\text{-}H)_2BH_2]$ before heating (top, blue) and after heating at 120 °C for 48 hours (bottom, red).

4.4 Synthesis and Investigation of [{(dmpe)$_2$MnH}$_2$(μ-dmpe)] (12) and [(dmpe)$_2$MnH(κ^1-dmpe)] (13)

During the synthesis of [(dmpe)$_2$Mn(μ-H)$_2$BH$_2$], ^{1}H NMR spectra of crude reaction mixtures contained a set of nearly overlapping MnH signals at –15.72 and –15.74 ppm, which were subsequently assigned to [{(dmpe)$_2$MnH}$_2$(μ-dmpe)] **(12)** and [(dmpe)$_2$MnH(κ^1-dmpe)] **(13)**. The additional dmpe ligand in these complexes is rationalized to be generated from the decomposition of one or more equivalents of either the reaction product or intermediate, as seen in the thermal decomposition of borohydride complex **12** (Figure 4.3).

The identical mixture of hydride complexes (**12** and **13**) can be independently prepared through the reaction of [(dmpe)$_2$MnH(C$_2$H$_4$)] with free 1,2-bis(dimethylphosphino)ethane (dmpe) under an atmosphere of argon (overnight at 105 °C), or more cleanly under an atmosphere of H$_2$ (several days at 60 °C). The formation of bimetallic complex **6** is favoured when using an approximate 1:2 ratio of dmpe to [(dmpe)$_2$MnH(C$_2$H$_4$)], whereas monometallic complex **13** is favoured using a 3:2 ratio. Under argon atmosphere, the syntheses of **12** and **13** proceed *via* ethylene substitution, whereas those under H$_2$ atmosphere involve initial reaction of [(dmpe)$_2$MnH(C$_2$H$_4$)] with one equiv. of H$_2$ to generate [(dmpe)$_2$MnH] and ethane. The [(dmpe)$_2$MnH] intermediate can then coordinate to a free phosphine donor to form **12** or **13**, or a second equivalent of H$_2$ to generate [(dmpe)$_2$MnH(H$_2$)] (observed by NMR spectroscopy as the reaction progresses) which then converts to complex **12** or **13** by direct phosphine substitution of

the H_2 ligand (Jones *et al.* have shown that the H_2 ligand in [(dmpe)$_2$MnH(H_2)] can undergo dissociative substitution with a range of neutral donors: CO, isonitriles, ethylene, and N_2).

Bimetallic complex **12** is practically insoluble in hexanes, while monometallic complex **13** is very soluble, allowing **12** to be isolated as a yellow powder by washing the crude reaction mixture with hexanes (Figure 4.4). While complex **12** is non-volatile, complex **13** sublimes with no decomposition at 100 °C (5 mTorr) and was therefore separated from the crude reaction mixture through sublimation (Scheme 4.4). Even when considering the vast amount of transition metal dmpe complexes, **13** is only the second crystallographically characterized example with a κ^1-coordinated terminal dmpe ligand.

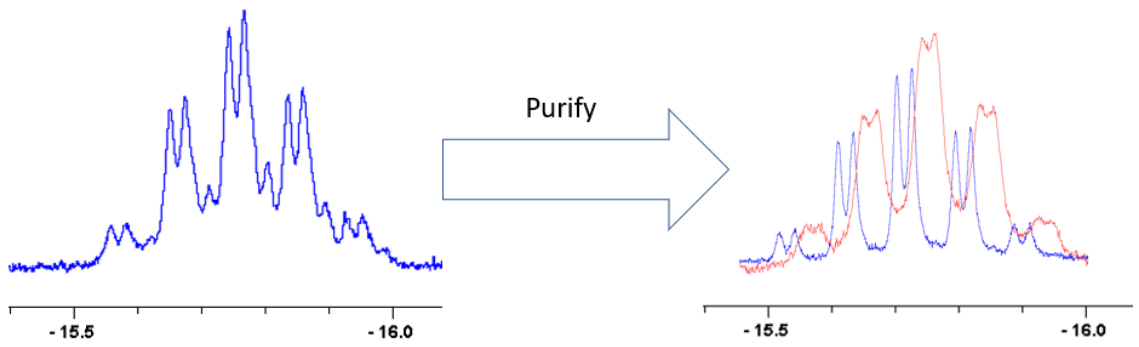

Figure 4.4: Left: ^{1}H NMR (C_6D_6, 600 MHz) spectrum showcasing hydride signals of crude reaction mixture obtained during synthesis of [{(dmpe)$_2$MnH}$_2$(μ-dmpe)] **(12)**. Right: ^{1}H NMR spectra (C_6D_6, 600 MHz) showcasing hydride signals of purified [{(dmpe)$_2$MnH}$_2$(μ-dmpe)] (**12**, red) and [(dmpe)$_2$MnH(κ^1-dmpe)] (**13**, blue).

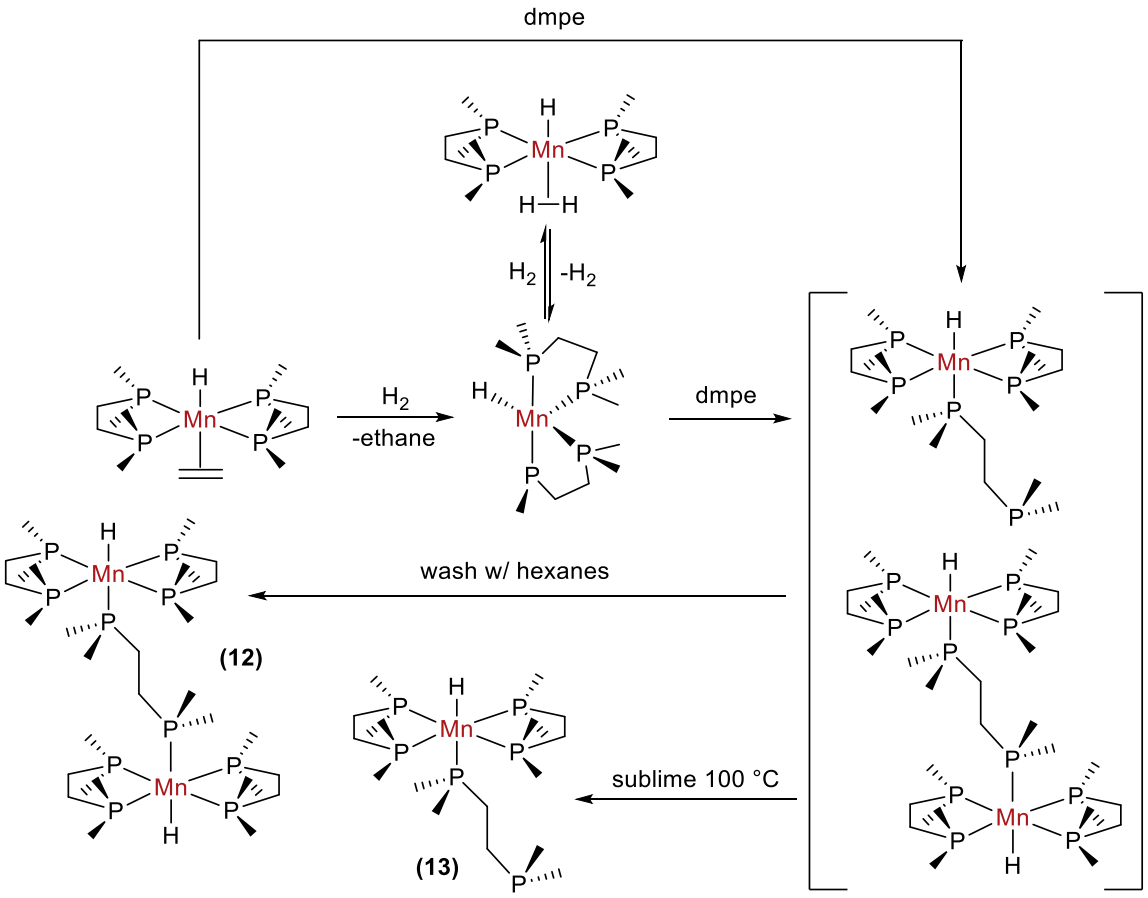

Scheme 4.4: Synthesis of [{(dmpe)$_2$MnH}$_2$(μ-dmpe)] **(12)** and [(dmpe)$_2$MnH(κ^1-dmpe)] **(13)**. The reaction leads to a mixture of the two complexes, which can then be purified independently either through washing with hexanes (in the case of **12**) or subliming at 100 °C (in the case of **13**).

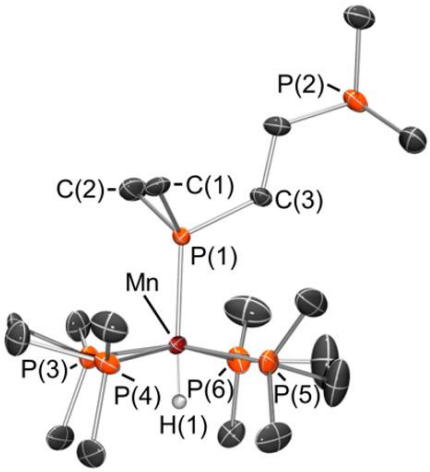

Figure 4.5: X-ray crystal structure of *trans*-[(dmpe)$_2$MnH(κ^1-dmpe)] **(13)**. Most hydrogen atoms have been omitted for clarity, with ellipsoids drawn at 50% probability. Space group P2$_1$, R^1 = 8.88. Hydrogen atoms on Mn were located from the difference map, with the exception of H on Mn(1C), and refined isotropically. Distances (Å) and angles (deg): (atoms with a letter suffix are related to those with the same identifying number without a suffix, but are located in one of the isostructural molecules in the unit cell) Mn(1)–P(1) 2.231(4), Mn(1A)–P(1A) 2.230(4), Mn(1B)–P(1B) 2.232(4), Mn(1C)–P(1C) 2.234(4), Mn(1)–P(3) 2.211(4), Mn(1A)–P(3A) 2.201(5), Mn(1B)–P(3B) 2.190(4), Mn(1C)–P(3C) 2.228(4), Mn(1)–P(4) 2.212(4), Mn(1A)–P(4A) 2.222(5), Mn(1B)–P(4B) 2.220(4), Mn(1C)–P(4C) 2.216(4), Mn(1)–P(5) 2.214(4), Mn(1A)–P(5A) 2.213(5), Mn(1B)–P(5B) 2.224(4), Mn(1C)–P(5C) 2.211(4), Mn(1)–P(6) 2.213(4), Mn(1A)–P(6A) 2.203(4), Mn(1B)–P(6B) 2.211(4), Mn(1C)–P(6C) 2.203(4), Mn(1)–H(1) 1.16(6), Mn(1A)–H(1A) 1.16(7), Mn(1B)–H(1B) 1.16(6), P(1)–Mn(1)–H(1) 161(4), P(1A)– Mn(1A)–H(1A) 173(4), P(1B)–Mn(1B)–H(1B) 166(3), Σ(P–Mn(1)–P) (*cis*, equatorial) 355.1(4), Σ(P–Mn(1A)–P) (*cis*, equatorial) 355.0(4), Σ(P–Mn(1B)–P) (*cis*, equatorial) 355.6(4), Σ(P–Mn(1C)–P) (*cis*, equatorial) 355.0(4)

In solution, [{(dmpe)$_2$MnH}$_2$(μ-dmpe)] and [(dmpe)$_2$MnH(κ^1-dmpe)] exist as both high (apparent C_{2v}) and low (C_1) symmetry isomers (Figure 4.6). Interestingly, the relative concentration of the low symmetry isomer increases drastically from < 5 % upon initial isolation to > 50 % after several weeks in light at room temperature (*cis* to *trans* isomerization was not observed in the dark).

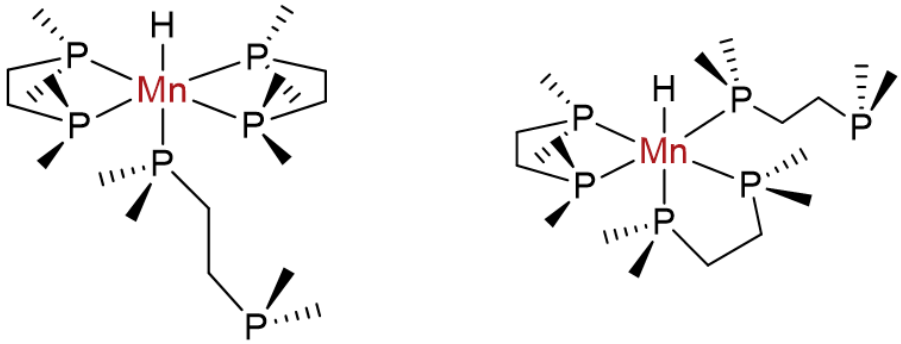

Figure 4.6: High (apparent C_{2v}) symmetry isomer of [(dmpe)$_2$MnH(κ^1-dmpe)] (left) and low (C_1) symmetry isomer of [(dmpe)$_2$MnH(κ^1-dmpe)] (right).

4.5 Synthesis and Investigation of [(dmpe)$_2$MnH(PMe$_3$)] (14)

Interested to see if these results could be extended to other phosphine ligands, [(dmpe)$_2$MnH(C$_2$H$_4$)] was exposed to a large excess of PMe$_3$, then placed under an atmosphere of H$_2$ to yield [(dmpe)$_2$MnH(PMe$_3$)] **(14)** after heating the reaction mixture for 4 days at 60 °C (Scheme 4.5). The novel complex can be obtained in very high yields and requires no purification other than exposure to vacuum to remove excess PMe$_3$. Crystals of the complex were grown from a concentrated solution of hexanes at –30 °C (Figure 4.7).

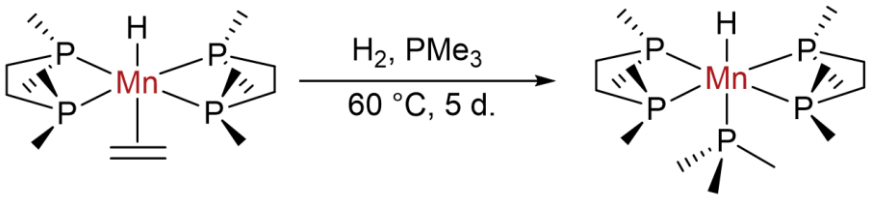

Scheme 4.5: Synthesis of [(dmpe)$_2$MnH(PMe$_3$)] **(14)**.

In a similar fashion to [{(dmpe)$_2$MnH}$_2$(μ-dmpe)] and [(dmpe)$_2$MnH(κ^1-dmpe)], [(dmpe)$_2$MnH(PMe$_3$)] exists in solution as two isomers with either *trans*- or *cis*- disposed

PMe_3 and hydride ligands. Once again, solutions of $[(dmpe)_2MnH(PMe_3)]$ contained almost entirely *trans*- isomer initially (> 95%), which slowly converts to the *cis*- isomer over time in light at room temperature. This isomerization was monitored over time by ^1H, ^2H, and $^{31}P\{^1H\}$ NMR spectroscopy through the preparation of four NMR samples with equivalent concentrations of $[(dmpe)_2MnH(PMe_3)]$: one solution with and one without excess PMe_3 were covered in aluminum foil between NMR experiments to prevent exposure to light, and one solution with and one without excess PMe_3 were left in a fumehood with the light turned on between NMR experiments. Resultant photochemical *trans*-*cis* isomerization was observed after 1 week at room temperature, with the *cis*:*trans* ratio increasing to > 3:1, and deuterium incorporation into the alkyl and hydride environments from C_6D_6 activation. Conversion back to the *trans* isomer was observed when the solution of *cis* and *trans* isomers was left in the dark (the *trans* isomer becoming the dominant species in solution once again after 5 days at room temperature). Additionally, heating the *cis*/*trans* mixture at 60 °C for 3 hours resulted in nearly complete conversion back to the *trans* isomer. The presence of excess PMe_3 (~10 eq.) had no significant inhibiting effect in either the photochemical or thermally induced isomerization processes, although activation of C_6D_6 was supressed.

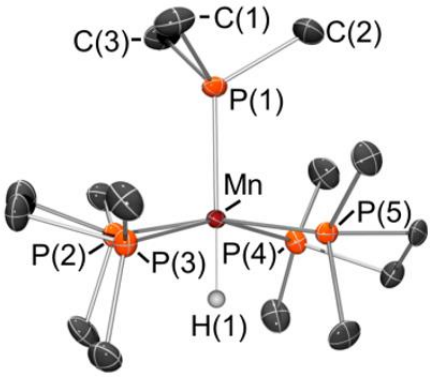

Figure 4.7: X-ray crystal structure of [(dmpe)$_2$MnH(PMe$_3$)] **(14)**. Most hydrogen atoms have been omitted for clarity, with ellipsoids drawn at 50% probability. Space group $P\bar{1}$, R^1 = 6.74. Hydrogen atoms on Mn were located from the difference map and refined isotropically. Distances (Å) and angles (deg): Mn(1)–P(1) 2.234(1), Mn(1)–P(2) 2.216(2), Mn(1)–P(3) 2.218(1), Mn(1)–P(4) 2.225(1), Mn(1)–P(5) 2.215(1), Mn(1)–H(1) 1.35(6), P(1)–Mn(1)–H(1) 179(2), Σ(P–Mn–P) (*cis*, equatorial) 355.3(1).

[(dmpe)$_2$MnH(PMe$_3$)] **(14)** is reasonably volatile and can be sublimed at 60 °C (5 mTorr), leading to its study as a potential ALD precursor or co-reactant (behaving as a metal hydride, due to the extremely electron-rich metal centre which leads to a non-acidic hydride). The complex is reasonably thermally stable, but after 3 days of heating a solid sample at 100 °C there was observable broadening of all peaks corresponding to [(dmpe)$_2$MnH(PMe$_3$)], as well as the growth of a small new doublet in the alkyl region (Figure 4.8). While this thermal stability falls just barely outside of the desirable range for use in ALD, it may be sufficient for CVD experiments in which the reactor is operated under vacuum with no accompanying argon flow.

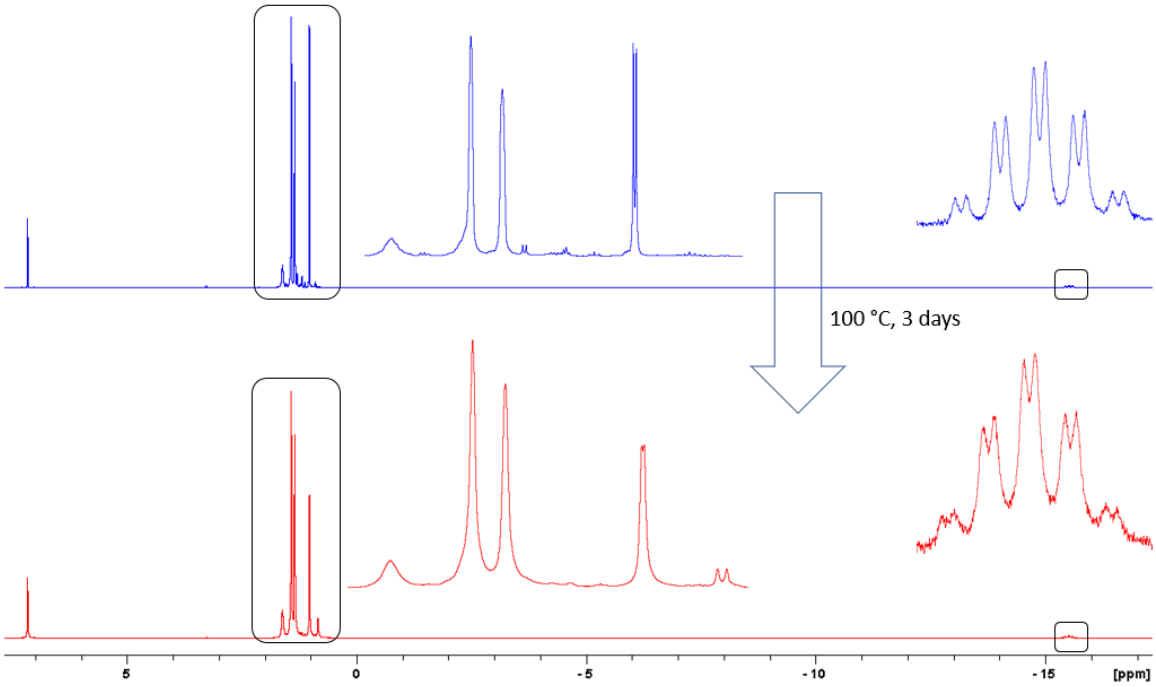

Figure 4.8: ^{1}H NMR spectra of [(dmpe)$_2$MnH(PMe$_3$)] before heating (top, blue) and [(dmpe)$_2$MnH(PMe$_3$)] after heating at 100 °C for 3 days (bottom, red).

4.6 Chapter Summary, Conclusions, and Future Work

The borohydride complex [(dmpe)$_2$Mn(μ-H)$_2$BH$_2$] **(11)** was accessed via the reaction of [(dmpe)MnH(C$_2$H$_4$)] with BH$_3$(NMe$_3$), and the reaction proceeds through straightforward ethylene substitution. The complex sublimes without decomposition at 80 °C, but undergoes thermal decomposition after days in the solid state at 120 °C to form bimetallic [{(dmpe)$_2$MnH}$_2$(μ-dmpe)] **(12)**. Compound **11** therefore lacks the desired thermal stability for ALD usage.

The presence of [(dmpe)$_2$MnH(κ^1-dmpe)] **(13)** was discovered during the independent synthesis of **12**, which prompted the synthesis of [(dmpe)$_2$MnH(PMe$_3$)] **(14)**. These pentaphosphino hydride complexes were independently prepared from

[(dmpe)MnH(C_2H_4)] by exposure to either free dmpe or PMe_3 under an atmosphere of H_2, wherein the reaction proceeds with initial ethane elimination to form [(dmpe)$_2$MnH], allowing for lower reaction temperatures and shorter reaction times, relative to reactions in the absence of H_2. Compounds **12**–**14** exist in solution as isomers with *cis*- or *trans*-disposed hydride and κ^1-PR_3 ligands. Prior to this work, the sole example of a pentaphosphine manganese hydride complex is [$(F_3P)_5$MnH], which differs substantially from these new complexes from an electronic standpoint (PF_3 is a strong pi-acceptor ligand similar to carbon monoxide).

The volatility of [(dmpe)$_2$MnH(PMe_3)] **(14)** lead to its investigation as an ALD precursor. The complex undergoes minor decomposition after being heated 40 °C higher than its sublimation temperature in the solid state, which reduces its usefulness for ALD, but the complex may still prove useful as a CVD precursor. CVD with compound **14** should therefore be attempted.

Table 4.1: Summary of yield, volatility, and thermal stability of [(dmpe)$_2$Mn(μ-H)$_2$BH$_2$] **(11)** and [(dmpe)$_2$MnH(PMe_3)] **(14)**.

Complex	Yield	Sublimation Temp. (5 mTorr)	Thermal Stability†
[(dmpe)$_2$Mn(μ-H)$_2$BH$_2$] **(11)**	32%	80 °C	Moderate decomposition
[(dmpe)$_2$MnH(PMe_3)] **(14)**	94%	60 °C	Minor decomposition

†At a temperature 40 °C higher than the sublimation temperature (5 mTorr), over the prescribed time period (up to 3 days).

Chapter 5 – Experimental Details

5.1 General Experimental Details

5.1.1 Laboratory Equipment and Apparatus

An argon-filled MBraun UNIlab glove box equipped with a –30 °C freezer was employed for the manipulation and storage of all oxygen- and moisture- sensitive compounds. Air-sensitive preparative reactions were performed on a double-manifold high-vacuum line equipped with a two stage Edwards RV 12 rotary vane vacuum pump (ultimate pressure 1×10^{-4} Torr) using standard techniques.[195] Residual oxygen and moisture were removed from the argon stream by passage through an Oxisorb-W scrubber from Matheson Gas Products. The vacuum was measured periodically using a Kurt J. Lesker 275i convection enhanced Pirani gauge. Celite and Alumina were dried for 24 hours in a Blue M (Model M15A-2A) oven set to 400 °C, before being stored in the glovebox prior to use. Commonly used specialty glassware included thick walled flasks equipped with Teflon stopcocks, a swivel frit assembly, Teflon stopcocks, custom designed air-free sublimators, and J-Young NMR tubes. A VWR Clinical 200 Large Capacity Centrifuge (with 28° fixed-angle rotors that hold 12 × 15 mL or 6 × 50 mL tubes, in combination with VWR high performance polypropylene conical centrifuge tubes) located within a glove box was used where indicated. A Branson 2510 ultrasonic bath was used to sonicate reaction mixtures. NMR spectroscopy was performed on Bruker AV-500, and AV-600 spectrometers. All ^{1}H NMR spectra were obtained at 298 K and referenced relative to $SiMe_4$ through a resonance of the protio impurity of the solvent used: C_6D_6 (δ 7.16 ppm). Any ^{31}P or ^{11}B NMR spectra were referenced using an indirect referencing technique as

per Iowa State University.[196] Combustion elemental analyses were performed by Midwest Microlabs (IN, USA).

Single-crystal X-ray crystallographic analyses were performed on crystals coated in Paratone oil and mounted on a SMART APEX II diffractometer with a 3-kW sealed-tube Mo generator and SMART6000 CCD detector in the McMaster Analytical X-Ray (MAX) Diffraction Facility. A semi-empirical absorption correction was applied using redundant data. Raw data sets were processed using XPREP (as part of the APEX v2.2.0 software) and solved by direct (SHELXS-97) methods. The structure was completed by difference Fourier synthesis and refined with full-matrix least-squares procedures based on F2. In all cases, non-hydrogen atoms were refined anisotropically and hydrogen atoms were generated in ideal positions and then updated with each cycle of refinement. Refinement was performed using Olex2.

Powder X-ray diffraction experiments were performed on a Bruker D8 Advance powder diffractometer with Cu Kα radiation ($\lambda = 0.154$ nm) operated at 40 kV and 40 mA. Powders were packed in 0.5 mm special glass (wall thickness 0.01 mm) capillary tubes for X-ray diffraction (purchased from Charles Supper Co.) and sealed by inverting to submerge the open end in a pool of Apiezon H-grease within the glovebox. Calculated powder patterns were generated from the low-temperature single crystal data and a file downloaded from the Cambridge Crystallographic Database using Mercury. Experimental powder diffractograms were generated and viewed using Gadds, Diffrac.eva, and Topaz.

Thermal stability data was obtained by acquiring a ^{1}H NMR spectrum of the sample of interest in a J-Young tube, then (in most cases, unless otherwise noted) removing the NMR solvent *in vacuo*. The solid was heated to the desired temperature for the prescribed length of time, then cooled to room temperature for visual inspection and solubilized (by adding solvent in the glovebox) for ^{1}H NMR spectroscopy.

5.1.2 Solvents

Benzene, diethyl ether, pentane, hexanes, toluene, DME, THF, and hexamethyldisiloxane were purchased from Aldrich. Deuterated solvents were purchased from ACP Chemicals. Benzene, diethyl ether, THF, pentane, hexanes, and toluene were initially dried and distilled at atmospheric pressure from sodium/benzophenone (first five solvents) or sodium (toluene). Hexamethyldisiloxane and benzene were dried over 4 Å molecular sieves. All solvents were stored over an appropriate drying agent (diethyl ether, toluene, THF, C_6D_6 = Na/Ph_2CO; hexanes, pentane = Na/Ph_2CO/tetraglyme) and introduced to reactions or solvent storage flasks via vacuum transfer with condensation at –78 °C.

5.1.3 Starting Materials

Dmpe, H_3SiPh, 1,4-dioxane, trimethylsilylmethylmagnesium chloride solution (1.0 M in diethyl ether), ethylmagnesium chloride solution (2.0 M in diethyl ether), (trimethylsilyl)methyllithium solution (1.0 M in pentane), methyllithium solution (1.6 M in diethyl ether), trimethyl phosphine, $CrCl_3$·3THF, $VOCl_3$, and $NiBr_2$(dme) were purchased from Sigma-Aldrich.

Manganese dichloride, cobalt dichloride, molybdenum pentachloride, tungsten hexachloride, and chromium dichloride were purchased from Strem Chemicals. Argon and hydrogen gas were purchased from PraxAir. Bis(trimethylsilylmethyl)magnesium,[150] and $[(dmpe)_2MnH(C_2H_4)]$[188] were prepared according to literature methods.

5.2 Experimental Procedures

$[Cr(CH_2SiMe_3)_4]$ (1). This paramagnetic compound was prepared via a modification of the literature procedure.[134] To a 100 mL flask was added a suspension of $CrCl_3$•3THF (264 mg, 0.705 mmol) in 25 mL of Et_2O. $Mg(CH_2SiMe_3)_2$ (217 mg, 1.092 mmol) in 10 mL of Et_2O was pipetted into the flask within the glovebox with stirring, resulting in an immediate colour change to deep purple. After 3 hours of stirring the solvent was removed *in vacuo*, while the flask was cooled to ~0 °C using a water/ice bath to prevent sublimation of the product. The residue was extracted with hexanes, and centrifuged. The solvent was removed from the supernatant *in vacuo* (with cooling to ~0 °C using a water/ice bath), giving a deep purple residue. This residue was sublimed at 25 °C to yield a purple crystalline solid (282 mg, 29%). **^{1}H NMR (C_6D_6, 600 MHz, 298 K):** δ –2.16 (broad s, Si<u>Me</u>$_3$).

$[Cr(CH_2CMe_3)_4]$ (2). This paramagnetic compound was prepared via a modification of the literature procedure.[149] To a 100 mL flask was added a suspension of $CrCl_3$•3THF (100 mg, 0.26 mmol) in 25 mL of Et_2O. $Mg(CH_2CMe_3)_2$ (61.2 mg, 0.44 mmol) in 10 mL of Et_2O was pipetted into the flask within the glovebox with stirring, resulting in an immediate colour change to brown. After 3 hours of stirring, the solvent was removed *in*

vacuo. The residue was extracted with hexanes, and centrifuged. The solvent was removed from the supernatant *in vacuo*, giving a brown residue. This residue was sublimed at 50 °C to yield a maroon crystalline solid, suitable for single-crystal X-ray diffraction (42 mg, 43%). **^{1}H NMR (C_6D_6, 600 MHz, 298 K):** δ –6.81 (broad s, C<u>Me</u>$_3$).

[V(CH_2SiMe_3)$_4$] (3). This paramagnetic compound was prepared via a modification of the literature procedure.[134] To a 100 mL flask was added Mg(CH_2SiMe_3)$_2$ (2.52 g, 11.7 mmol) in 25 mL of Et_2O. The solution was cooled to –78°C, and $VOCl_3$ (0.4 mL, 4.2 mmol) in 25 mL of Et_2O was added dropwise to the flask via syringe with stirring, over the course of 30 mins. Initially upon addition, the reaction mixture became blue, then upon completion and warming to room temperature, a deep green colour formed. After stirring for 3 hours the solvent was removed *in vacuo*, while the flask was cooled to ~0 °C using a water/ice bath to prevent sublimation of the product. The residue was extracted with hexanes, and centrifuged. The solvent was removed from the supernatant *in vacuo* at ~0 °C to give a black/green residue. The residue was sublimed at 30 °C using a sublimator equipped with a dry-ice cold finger to yield a deep green solid, which formed an oil upon warming to room temperature (29 mg, 17%). X-ray quality crystals were obtained from a concentrated solution of hexamethyldisiloxane at –30 °C. **^{1}H NMR (C_6D_6, 600 MHz, 298 K):** δ –0.85 (broad s, Si<u>Me</u>$_3$).

Procedure for mounting crystals of **[V(CH_2SiMe_3)$_4$] (3)**. The dish for transporting the crystals from the glove box to the X-ray diffractometer and paratone oil used to coat the crystals were placed in a –30 °C freezer within the glovebox to cool. After removal of solvent from the crystallization vial, the crystals were coated with the cooled paratone oil

then placed onto the cooled transport dish which was held within a bucket filled with dry ice for transport. Selection of crystals under a microscope was made impossible due to the fact that once placed on the goniometer head, the crystals had melted by the time they reached the 100 K N_2 stream within the diffractometer (the adjacent room, ~6 seconds). Instead, a crystal was selected by the naked eye whilst standing directly in front of the diffractometer with the carrying dish remaining in the dry ice bucket, then swiftly (~1 second) mounted in the 100 K N_2 stream to prevent melting.

Procedure for structure solution and refinement of **[V(CH$_2$SiMe$_3$)$_4$] (3)**. The twin law (-1, 0, 0, 0, -1, 0, 0, 0, -1) was applied during refinement. Several extra-large difference map peaks remained after solving one possible molecule orientation. These peaks were resolved by flipping and shifting the entire molecule to adjust for the other possible molecular orientation, which possessed approximately 15% occupancy.

[{V(CH$_2$SiMe$_3$)$_3$O}$_2$Mg(dme)$_2$] (4). To a 100 mL flask was added Mg(CH$_2$SiMe$_3$)$_2$ (1.80 g, 8.35 mmol) in 25 mL of Et$_2$O. The solution was cooled to –78°C, and VOCl$_3$ (0.28 mL, 3.02 mmol) in 25 mL of Et$_2$O was added dropwise to the flask via syringe with stirring, over the course of 15 mins. After 10 minutes of stirring, the solvent was removed *in vacuo*, yielding a blue-green residue. The residue was extracted with DME, and centrifuged. The solvent was removed from the supernatant *in vacuo* to give a blue-green residue. Blue X-ray quality crystals were obtained from a concentrated solution of DME at –30 °C.

$W_2(CH_2SiMe_3)_6$ (5). This diamagnetic compound was prepared via a modification of the literature procedure.[134] To a 100 mL flask was added $Mg(CH_2SiMe_3)_2$ (1.09 g, 5.5 mmol) in 30 mL of Et_2O. A brown solution of WCl_5 (1.00 g, 2.5 mmol) in 25 mL of Et_2O was added over the course of 1 h via syringe, and the mixture was stirred for 3 h. The solvent was removed *in vacuo* and the residue extracted with hexanes, then centrifuged. The supernatant, a deep brown solution, was concentrated *in vacuo* to ca. 5 mL, then transferred to a neutral alumina plug within a small column (approximately 4 inches of alumina) and eluted with hexanes. The orange fraction (first to elute) was collected and the solvent was removed *in vacuo*, leaving an orange solid (303 mg, 14%). **^{1}H NMR (C_6D_6, 600 MHz, 298 K):** δ 0.26 (s, 54H, Si<u>Me</u>$_3$), 1.91 (s, 12H, C<u>H</u>$_2$).

$Mo_2(CH_2SiMe_3)_6$ (6). This diamagnetic compound was prepared via (a modification of) the literature procedure.[134] To a 100 mL flask was added $Mg(CH_2SiMe_3)_2$ (1.00 g, 3.66 mmol) in 30 mL of Et_2O. A brown solution of $MoCl_5$ (2.19 g, 10.0 mmol) in 25 mL of Et_2O was added over the course of 1 h via syringe, and the mixture was stirred for 3 h. The solvent was removed *in vacuo* and the residue extracted with hexanes, then centrifuged. The supernatant, a deep brown solution, was concentrated *in vacuo* to ca. 5 mL, then transferred to a neutral alumina plug within a small column (approximately 4 inches of alumina) and eluted with hexanes. The yellow fraction (first to elute) was collected and the solvent was removed *in vacuo*, leaving a yellow solid (298 mg, 11%). **^{1}H NMR (C_6D_6, 600 MHz, 298 K):** δ 0.25 (s, 54H, Si<u>Me</u>$_3$), 2.02 (s, 12H, C<u>H</u>$_2$).

[$CrCl_2(dmpe)_2$]. This paramagnetic compound was prepared via the literature procedure.[154] To a 50 mL flask was added a grey suspension of $CrCl_2$ (250 mg, 2.03 mmol)

in 25 mL of toluene. A solution of dmpe (620 mg, 4.13 mmol) in 10 mL of toluene was added to the flask, within the glovebox. After 1 hour of stirring, the solution started to become green. The solution was stirred overnight, then concentrated to ca. 10 mL and maintained at –30 °C, yielding large green crystals which were dried *in vacuo* (1.12 g, 92%). **^{1}H NMR (C_6D_6, 600 MHz, 298 K):** δ –13.04 (4H, broad s, PC$\underline{H}_2$), –33.43 (12H, broad s, PC$\underline{H}_3$)

[Cr(dmpe)$_2$(Me)$_2$] (7). This paramagnetic compound was prepared via a slight modification of the literature procedure.[154] To a 100 mL flask was added a suspension of [$CrCl_2$(dmpe)$_2$] (200 mg, 0.47 mmol) in 30 mL of Et_2O. Methyl lithium (28.6 mg, 1.32 mmol) was suspended in 10 mL of Et_2O and added by pipette within the glovebox to the flask over 5 minutes, with stirring. The solution turned orange at the end of the addition and stirring was continued for an additional 48 hours, with intermittent sonication to dissolve the mostly insoluble methyl lithium. The solvent was removed *in vacuo*, and the orange residue was dissolved in 10 mL of hexanes, then passed through celite to remove LiCl salts. The solution was cooled to –30 °C to induce crystallization, and orange crystals were collected which were dried *in vacuo* (69 mg, 72%). **^{1}H NMR (C_6D_6, 600 MHz, 298 K):** δ 0.96 (~4 H, broad s, PC$\underline{H}_2$), –28.60 (~12H, broad s, PC$\underline{H}_3$)

[Ni{1,3-(SiMe$_3$)$_2$C$_3$H$_3$}$_2$] (8). This diamagnetic compound was prepared via the literature procedure.[163] To a 100 mL flask was added a pink suspension of $NiBr_2$•DME (254 mg, 0.82 mmol) in 30 mL of THF. K[1,3-(SiMe$_3$)$_2$C$_3$H$_3$] (370 mg, 1.64 mmol) was dissolved in 10 mL of THF and transferred to a syringe. The flask was cooled to –78 °C, and the K[1,3-(SiMe$_3$)$_2$C$_3$H$_3$] solution was added dropwise over the course of 30 mins, resulting in

a brown solution. The reaction was allowed to warm to room temperature and stir overnight. The solvent was removed *in vacuo* and the residue extracted with hexanes, then centrifuged. The supernatant was collected, and the solvent was removed *in vacuo* to yield a brown/red residue which was sublimed at 40 °C to yield a red solid (170 mg, 41%). Major product diastereomer **^{1}H NMR (500 MHz, C_6D_6, 298 K):** δ 0.15 (s, 18H, $SiMe_3$), 0.15 (s, 18H, $SiMe_3$), 2.67 (d, *J* = 16.0 Hz, 2H, anti C–H), 3.60 (d, *J* = 10.4 Hz, 2H, syn C–H), 4.96 (dd, *J* = 16.0 Hz, *J* = 10.4 Hz, 2H, $C_{(2)}$–H). Minor product diastereomer **^{1}H NMR (500 MHz, C_6D_6, 298 K):** δ –0.05 (s, 18H, $SiMe_3$), 0.29 (s, 18H, $SiMe_3$), 2.07 (d, *J* = 16.4 Hz, 2H, anti C–H), 3.63 (d, *J* = 10.0 Hz, 2H, syn C–H), 5.62 (dd, *J* = 16.4 Hz, *J* = 10.0 Hz, 2H, $C_{(2)}$–H).

[Cr{1,3-$(SiMe_3)_2C_3H_3$}$_2$] (9). This paramagnetic compound was prepared via the literature procedure.[167] To a 100 mL flask was added a grey suspension of $CrCl_2$ (150 mg, 1.22 mmol) in 30 mL of THF. K[1,3-$(SiMe_3)_2C_3H_3$] (550 mg, 2.44 mmol) was dissolved in 10 mL of THF and transferred to a syringe in the glove box. The flask was cooled to –78 °C, and the K[1,3-$(SiMe_3)_2C_3H_3$] solution was added dropwise over a course of 30 mins, giving a brown solution. The solution was warmed to room temperature and stirred for 3 hours. The solvent was removed *in vacuo* and the brown residue extracted with hexanes, then centrifuged. The supernatant was collected, and the solvent removed *in vacuo* to yield a red/orange residue which was sublimed at 50 °C, yielding a red solid (314 mg, 60%). **^{1}H NMR (600 MHz, C_6D_6, 298 K):** δ –0.02 (s, 18H), 0.13 (s, 18H), 0.20 (s, 12H), 1.39 (broad s), 6.04 (broad s), 7.91 (broad s), 9.04 (broad s).

[Co{1,3-(SiMe$_3$)$_2$C$_3$H$_3$}$_2$] (10). This paramagnetic compound was prepared via the literature procedure.[168] To a 100 mL flask was added a bright blue suspension of $CoCl_2$ (110 mg, 0.84 mmol) in 30 mL of THF. K[1,3-(SiMe$_3$)$_2$C$_3$H$_3$] (382 mg, 1.70 mmol) was dissolved in 10mL of THF and transferred to a syringe. The reaction flask was cooled to –78 °C, and the K[1,3-(SiMe$_3$)$_2$C$_3$H$_3$] solution was added dropwise over a course of 30 mins, giving a brown solution. The solution was warmed to room temperature and stirred for 3 hours. The solvent was removed *in vacuo* and the residue was extracted with hexanes, then centrifuged. The supernatant was collected, and the solvent was removed *in vacuo* to yield a brown/orange residue which was sublimed at 50 °C, yielding an orange solid (275 mg, 65%).

[(dmpe)$_2$Mn(μ-H)$_2$BH$_2$] (11). To a yellow solution of (dmpe)$_2$MnH(C$_2$H$_4$) (225 mg, 0.58 mmol) in 40 mL of toluene was added a solution of BH$_3$-NMe$_3$ (64 mg, 0.88 mmol) in 10 mL of toluene, within the glovebox. The resulting solution was added to a sealed 100 mL flask and heated at 90 °C, with stirring. After 2 days of heating, the headspace of the flask was briefly evacuated *in vacuo*, removing some ethylene produced by the reaction. After an additional 2 days at 90 °C, the solvent was removed *in vacuo* leaving a dark purple solid. The solid was dried under vacuum for an additional 60 mins. to remove excess BH$_3$-NMe$_3$. The crude product was recrystallized from hexanes at –30 °C giving deep purple crystals which were dried *in vacuo* (64 mg, 30%). X-ray quality crystals were obtained from a concentrated solution in hexanes at –30 °C. $T_{\text{sublimation}}$ (5 mTorr): 80−85 °C. **^{1}H NMR (d$_8$-toluene, 600 MHz, 298 K):** δ 5.08 (m, 2H, Mn(μ-H)$_2$B$\underline{H}_2$), 1.69, 1.16 (2 × m, 2H, PC$\underline{H}_2$), 1.60, 1.43 (2 × m, 6H, PC$\underline{H}_3$), 1.34 (m, 4H, PC$\underline{H}_2$), 0.97 (d, 6H,

$^{2}J_{H,P}$ 5.8 Hz, PC<u>H</u>3), 0.71 (d, 6H, $^{2}J_{H,P}$ 5.2 Hz, PC<u>H</u>$_3$), −16.52 (m, 2H, Mn(μ-<u>H</u>)$_2$BH$_2$). **^{11}B{1H} NMR (d$_8$-toluene, 192 MHz, 298 K):** δ 25.30 (s). **^{13}C{1H} NMR (d$_8$-toluene, 151 MHz, 298 K):** δ 33.48, 32.78 (2 × m, P<u>C</u>H$_2$), 29.12, 23.25 (2 × m, P<u>C</u>H$_3$), 21.82 (s, P<u>C</u>H$_3$), 20.21 (P<u>C</u>H$_3$). **^{31}P{1H} NMR (d$_8$-toluene, 243 MHz, 298 K):** δ 88.56, 72.54 (2 × s). Anal. found (calcd): C, 38.99 (38.95); H, 9.64 (9.81).

[{(dmpe)$_2$MnH}$_2$(μ-dmpe)] (12). 1,2-Bis(dimethylphosphino)ethane (18.1 mg, 0.12 mmol) was added to a yellow solution of [(dmpe)$_2$MnH(C$_2$H$_4$)] (100 mg, 0.26 mmol) in 25 mL of toluene within the glovebox. The resulting solution was placed in a 100 mL flask with a Teflon stopcock and freeze-pump-thawed (3x). The reaction flask was placed under an atmosphere of hydrogen gas at –131 °C using a liquid nitrogen-pentane bath, then sealed to afford approximately 2 atm of hydrogen gas for reactivity once warmed to room temperature. After stirring the mixture for 4 days at 60 °C, the solvent was removed *in vacuo* leaving a crude yellow solid. The solid was washed with two 4 mL portions of cooled (–30 °C) hexanes, then dried *in vacuo* (29.3 mg, 0.03 mmol, 28%). X-ray quality crystals were obtained from a concentrated solution in toluene at –30 °C. NMR data for *trans,trans*-**12** are as follows: **^{1}H NMR (C$_6$D$_6$, 600 MHz, 298 K):** δ 1.66, 1.50 (2 × m, 8H, PC<u>H</u>$_2$-chelating), 1.48, 1.36 (2 × s, 24H, PC<u>H</u>$_3$-chelating), 1.30 (br. s, 4H, PC<u>H</u>$_2$-κ^1), 1.02 (d, $^{2}J_{H,P}$ 3.5 Hz, 12H, PC<u>H</u>$_3$-κ^1), −15.74 (quin. of d, 2H, $^{2}J_{H,P}$ 48.8 Hz, $^{2}J_{H,P}$ 12.5 Hz, Mn<u>H</u>). **^{13}C{1H} NMR (C$_6$D$_6$, 126 MHz, 298 K):** δ 36.70 (m, P<u>C</u>H$_2$-κ^1), 34.34 (app. quin., $J_{C,P}$ 11.8 Hz, P<u>C</u>H$_2$-chelating), 32.07 (br. s, P<u>C</u>H$_3$-chelating), 24.68 (s, P<u>C</u>H$_3$-chelating), 24.61 (s, P<u>C</u>H$_3$-κ^1). **^{31}P{^{1}H} NMR (C6D6, 243 MHz, 298 K):** δ 78.82 (s, 8P, chelating P), 26.37 (s, 2P, κ^1-P). Selected NMR data for *cis* containing **12** are as follows: **^{1}H NMR (C$_6$D$_6$, 600 MHz,**

298 K): δ −11.61 (m, Mn$\underline{H}$). **^{31}P{^{1}H} NMR (C_6D_6, 243 MHz, 298 K):** δ 76.22, 75.07, 73.66, 63.73, 41.81 (5 × s). Anal. found (calcd): C, 41.69 (41.77); H, 9.52 (9.58). Anal. Found (calcd): C, 41.69 (41.77); H, 9.52 (9.58).

[(dmpe)$_2$MnH(κ^1-dmpe)] (13). To a yellow solution of (dmpe)$_2$MnH(C_2H_4) (170 mg, 0.44 mmol) in 50 mL of benzene was added a solution of dmpe (100 mg, 0.67 mmol), in 10 mL of the same solvent. The resulting solution was added to a 250 mL flask with a Teflon stopcock and freeze-pump-thawed (3x). The reaction flask was placed under an atmosphere of hydrogen gas at –131 °C using a liquid nitrogen pentane bath and sealed to afford approximately 2 atm of H_2 after warming. After stirring the mixture for 6 days at 60 °C, the solvent was removed *in vacuo* leaving a yellow oil. The oil was heated at 50 °C *in vacuo* for 24 hours to remove volatile impurities, then sublimed at 100 °C to yield yellow solid (77.4 mg, 35%). X-ray quality crystals were obtained from a concentrated solution in hexamethyldisiloxane at –30 °C. NMR data for *trans*-**13** are as follows: **^{1}H NMR (C_6D_6, 600 MHz, 298 K):** δ 1.62, 1.47 (2 × m, 4H, PC$\underline{H}_2$-chelating), 1.45, 1.34 (2 × s, 12H, PC$\underline{H}_3$-chelating), 1.38, (m, 2H, MnP (Me)$_2$CH$_2$C$\underline{H}_2$PMe$_2$), 1.28 (m, 2H, MnP(Me)$_2$C$\underline{H}_2$CH$_2$PMe$_2$), 0.96 (d, 6H, $^{2}J_{H,P}$ 3.8 Hz, MnP(PC$\underline{H}_3$)$_2$CH$_2$CH$_2$PMe$_2$), 0.89 (d, 6H, $^{2}J_{H,P}$ 2.8 Hz, MnP(Me)$_2$CH$_2$CH$_2$P(PC$\underline{H}_3$)$_2$), −15.72 (quin. of d, 1H, $^{2}J_{H,P}$ 48.8 Hz, $^{2}J_{H,P}$ 12.9 Hz, Mn$\underline{H}$). **^{13}C{^{1}H} NMR (C_6D_6, 151 MHz, 298 K):** δ 38.09 (s, MnP(Me)$_2$CH$_2$$\underline{C}H_2PMe_2$), 34.33 (app. quin., $^{1}J_{H,P}$ 11.9 Hz, P$\underline{C}$H$_2$-chelating), 32.02, 24.62 (2 × s, P$\underline{C}$H$_3$-chelating), 26.50 (d of d, $^{1}J_{H,P}$ 13.4 Hz, $^{2}J_{H,P}$ 7.3 Hz, MnP (Me)$_2$$\underline{C}H_2CH_2PMe_2$), 24.84 (d, $^{1}J_{H,P}$ 9.4 Hz, MnP (P$\underline{C}$H$_3$)$_2$CH$_2$CH$_2$PMe$_2$), 13.95 (d, $^{1}J_{H,P}$ 16.0 Hz, MnP (Me)$_2$CH$_2$CH$_2$P(P$\underline{C}$H$_3$)$_2$). **^{31}P{^{1}H} NMR (C_6D_6, 243 MHz, 298 K):** δ 78.63

(s, 4P, chelating P), 27.64 (s, 1P, Mn<u>P</u>(Me)$_2$CH$_2$CH$_2$PMe$_2$), −49.61 (d, 1P, $^3J_{P,P}$ 14.1 Hz, MnP (Me)$_2$CH$_2$CH$_2$<u>P</u>Me$_2$). Selected NMR data for *cis*-**13** are as follows: **^{1}H NMR (C$_6$D$_6$, 600 MHz, 298 K):** δ −11.66 (m, Mn<u>H</u>). **^{31}P{^{1}H} NMR (C$_6$D$_6$, 243 MHz, 298 K):** δ 76.00, 75.04, 73.38, 63.74, 43.10 (5 × s), −49.15 (d, $^3J_{P,P}$ 18.7 Hz, MnP(Me)$_2$CH$_2$CH$_2$<u>P</u>Me$_2$). Anal. found (calcd): C, 42.84 (42.70); H, 9.82 (9.75). Anal. Found (calcd): C, 42.84 (42.70); H, 9.82 (9.75).

[MnH(dmpe)$_2$(PMe$_3$)] (14). Trimethylphosphine (1.54 g, 20.2 mmol) was distilled into a 250 mL flask with a Teflon stopcock containing a yellow solution of (dmpe)$_2$MnH(C$_2$H$_4$) (2.03 g, 5.28 mmol) in 75 mL of benzene. The resulting solution was freeze-pump-thawed (3x). The reaction flask was placed under an atmosphere of hydrogen gas at –94 °C using a liquid nitrogen-acetone bath, then sealed to afford approximately 2 atm. of hydrogen gas for reactivity once warmed to room temperature. After stirring the mixture for 4 days at 60 °C, the solution was freeze-pump-thawed (1x). Additional trimethyl phosphine (0.62 g, 8.15 mmol) was distilled into the reaction flask, which was once again placed under an atmosphere of hydrogen gas, as before. The mixture was stirred for an additional 48 hours at 60 °C, then the solvent was removed *in vacuo* leaving a yellow solid (2.10 g, 94%). X-ray quality crystals were obtained from a concentrated solution in hexanes at –30 °C. $T_{\text{sublimation}}$ (5 mTorr) = 60 °C. NMR data for *trans*-**14** are as follows: **^{1}H NMR (C$_6$D$_6$, 600 MHz, 298 K):** δ 1.61, 1.42 (2 × m, 4H, PC<u>H</u>$_2$), 1.42, 1.34 (2 × s, 12H, dmpe-PC<u>H</u>$_3$), 1.02 (d, $^2J_{H,P}$ 4.2 Hz, 9H, PMe$_3$-PC<u>H</u>$_3$), −15.52 (quin. of d, $^2J_{H,P}$ 48.7 Hz, $^2J_{H,P}$ 13.7 Hz, 1H, Mn<u>H</u>). **^{13}C{^{1}H} NMR (C$_6$D$_6$, 126 MHz, 298 K):** δ 34.19 (app. quin., $J_{C,P}$ 12.2 Hz, dmpe-P<u>C</u>H$_2$), 31.84, 24.35 (2 × m, dmpe-P<u>C</u>H$_3$), 30.90 (d, $^1J_{C,P}$ 12.0 Hz, PMe$_3$-P<u>C</u>H$_3$). **^{31}P{^{1}H}**

NMR (C_6D_6, 243 MHz, 298 K): δ 79.13 (s, 4P, dmpe-P), 19.01 (s, 1P, PMe$_3$). NMR data for *cis*-**14** are as follows: **^{1}H NMR (C_6D_6, 600 MHz, 298 K):** δ 1.74, 1.62 (2 × m, 2H, PCH$_2$), 1.53 (d, $^2J_{H,P}$ 5.4 Hz, 3H, dmpe-PCH$_3$), 1.43, 1.42 (2 × m, 3H, dmpe-PCH$_3$), 1.37, 1.22 (2 × d, $^2J_{H,P}$ 4.7 Hz, 3H, dmpe-PCH$_3$), 1.34, 1.22, 1.20, 0.90 (4 × m, 1H, PCH$_2$), 1.29 (d, $^2J_{H,P}$ 5.0 Hz, 9H, PMe$_3$PCH$_3$), 1.20 (d, $^2J_{H,P}$ 4.3 Hz, 3H, dmpe-PCH$_3$), 1.18 (d, $^2J_{H,P}$ 4.4 Hz, 3H, dmpe-PCH$_3$), 1.04 (d, $^2J_{H,P}$ 4.1 Hz, 3H, dmpe-PCH$_3$), –11.73 (m, 1H, MnH). **^{13}C{^{1}H} NMR (C_6D_6, 126 MHz, 298 K):** δ 36.70, 35.13, 34.54 (3 × m, PCH$_2$), 31.97 (m, dmpe-PCH$_3$), δ 30.32 (d, $^1J_{C,P}$ 13.9 Hz, PMe$_3$-PCH$_3$), 28.10, 27.79, 26.09, 24.84, 24.51 (5 × m, dmpe-PCH$_3$), 25.02 (s, dmpe-PCH$_3$). **^{31}P{^{1}H} NMR (C_6D_6, 243 MHz, 298 K):** δ 76.23 (s, 2P, dmpe-P), 74.85, 63.90 (2 × s, 1P, dmpe-P), 31.23 (s, 1P, PMe$_3$). Anal. found (calcd): C, 41.54 (41.67); H, 9.67 (9.79).

Table A.1: Crystal and structure refinement data for $[Cr(CH_2CMe_3)_4]$ (2)

Identification code	DD01
Empirical formula	$C_{20}H_{40}Cr$
Formula weight	332.52
Temperature/K	100
Crystal system	orthorhombic
Space group	$Pca2_1$
a/Å	15.709(4)
b/Å	15.745(4)
c/Å	17.797(5)
α/°	90
β/°	90
γ/°	90
Volume/Å^3	4402(2)
Z	8
ρ_{calc}g/cm^3	1.004
μ/mm^{-1}	0.515
F(000)	1472.0
Crystal size/mm^3	0.3 × 0.1 × 0.04
Radiation	MoKα (λ = 0.71073)
2Θ range for data collection/°	2.586 to 56.964
Index ranges	$-21 \leq h \leq 21$, $-21 \leq k \leq 20$, $-23 \leq l \leq 21$
Reflections collected	66510
Independent reflections	10573 [R_{int} = 0.1995, R_{sigma} = 0.1652]
Data/restraints/parameters	10573/1/379
Goodness-of-fit on F^2	1.062
Final R indexes [I>=2σ (I)]	R_1 = 0.0869, wR_2 = 0.1851
Final R indexes [all data]	R_1 = 0.1965, wR_2 = 0.2318
Largest diff. peak/hole/eÅ^{-3}	0.93/–0.65
Flack parameter	0.00(3)

Table A.2: Crystal and structure refinement data for $[V(CH_2SiMe_3)_4]$ (3)

Identification code	Cc
Empirical formula	$C_{16}H_{37}Si_4V$
Formula weight	392.75
Temperature/K	100
Crystal system	monoclinic
Space group	Cc
a/Å	18.7000(10)
b/Å	8.3194(5)
c/Å	18.7076(14)
α/°	90
β/°	116.653(2)
γ/°	90
Volume/Å^3	2601.1(3)
Z	4
ρ_{calc}g/cm^3	1.003
μ/mm^{-1}	0.561
F(000)	848.0
Crystal size/mm^3	0.5 × 0.2 × 0.2
Radiation	MoKα (λ = 0.71073)
2Θ range for data collection/°	4.872 to 66.28
Index ranges	$-28 \leq h \leq 28$, $-12 \leq k \leq 12$, $-28 \leq l \leq 28$
Reflections collected	28210
Independent reflections	9761 [R_{int} = 0.0409, R_{sigma} = 0.0663]
Data/restraints/parameters	9761/332/267
Goodness-of-fit on F^2	1.151
Final R indexes [I>=2σ (I)]	R_1 = 0.0726, wR_2 = 0.1876
Final R indexes [all data]	R_1 = 0.0836, wR_2 = 0.1929
Largest diff. peak/hole/eÅ^{-3}	1.44/–1.97
Flack parameter	0.25(6)

Table A.3: Crystal and structure refinement data for [{V(CH_2SiMe_3)$_3$O}$_2$Mg(dme)$_2$] (4)

Identification code	DD26b
Empirical formula	$C_{23}H_{32}OSi_2VMg_{0.13}$
Formula weight	434.64
Temperature/K	296.15
Crystal system	orthorhombic
Space group	$Pca2_1$
a/Å	19.446(16)
b/Å	14.695(12)
c/Å	18.791(15)
α/°	90
β/°	90
γ/°	90
Volume/Å3	5370(7)
Z	8
ρcalcg/cm3	1.075
μ/mm-1	0.470
F(000)	1844.0
Crystal size/mm3	0.02 × 0.01 × 0.01
Radiation	MoKα (λ = 0.71073)
2Θ range for data collection/°	2.772 to 34.784
Index ranges	$-16 \leq h \leq 16$, $-12 \leq k \leq 12$, $-15 \leq l \leq 15$
Reflections collected	24277
Independent reflections	3306 [Rint = 0.2703, Rsigma = 0.1951]
Data/restraints/parameters	3306/1/446
Goodness-of-fit on F2	1.062
Final R indexes [I>=2σ (I)]	R1 = 0.0795, wR2 = 0.1158
Final R indexes [all data]	R1 = 0.1751, wR2 = 0.1418
Largest diff. peak/hole / e Å-3	0.23/–0.21
Flack parameter	0.07(6)

Table A.4: Crystal and structure refinement data for *trans*-[(dmpe)$_2$MnH(κ^1-dmpe)] (13)

Identification code	MnHdmpe3_trans
Empirical formula	$C_{18}H_{49}MnP_6$
Formula weight	506.36
Temperature/K	100
Crystal system	monoclinic
Space group	$P2_1$
a/Å	20.562(4)
b/Å	9.4569(18)
c/Å	28.035(5)
α/°	90
β/°	90.843(4)
γ/°	90
Volume/Å^3	5451.0(18)
Z	8
ρ_{calc}g/cm^3	1.234
μ/mm^{-1}	0.839
F(000)	2176.0
Crystal size/mm^3	0.020 × 0.020 × 0.020
Radiation	MoKα (λ = 0.71073)
2Θ range for data collection/°	3.492 to 56.508
Index ranges	$-27 \leq h \leq 27$, $-21 \leq k \leq 12$, $-37 \leq l \leq 37$
Reflections collected	85573
Independent reflections	26856 [R_{int} = 0.2398, R_{sigma} = 0.5649]
Data/restraints/parameters	26856/910/959
Goodness-of-fit on F^2	0.644
Final R indexes [I>=2σ (I)]	R_1 = 0.0888, wR_2 = 0.0771
Final R indexes [all data]	R_1 = 0.2458, wR_2 = 0.1006
Largest diff. peak/hole/eÅ^{-3}	0.98/–0.78
Flack parameter	0.46(3)

Table A.5: Crystal and structure refinement data for *trans*-[(dmpe)$_2$MnH(PMe$_3$)] (14)

Identification code	MnHPMe3_trans
Empirical formula	$C_{15}H_{42}MnP_5$
Formula weight	432.27
Temperature/K	100
Crystal system	triclinic
Space group	P–1
a/Å	9.2251(10)
b/Å	9.4251(10)
c/Å	15.1932(16)
α/°	91.032(3)
β/°	106.889(3)
γ/°	113.056(3)
Volume/Å3	1150.0(2)
Z	2
ρcalcg/cm3	1.248
μ/mm-1	0.916
F(000)	464.0
Crystal size/mm$_3$	0.02 × 0.02 × 0.01
Radiation	MoKα (λ = 0.71073)
2Θ range for data collection/°	2.834 to 52.618
Index ranges	$-11 \leq h \leq 11$, $-11 \leq k \leq 11$, $-18 \leq l \leq 18$
Reflections collected	19746
Independent reflections	4659 [R_{int} = 0.1174, R_{sigma} = 0.1203]
Data/restraints/parameters	4659/0/205
Goodness-of-fit on F2	1.034
Final R indexes [I>=2σ (I)]	R_1 = 0.0674, wR_2 = 0.1023
Final R indexes [all data]	R_1 = 0.1237, wR_2 = 0.1159
Largest diff. peak/hole/eÅ^{-3}	0.85/–0.75

References

(1) Cremers, V.; Puurunen, R. L.; Dendooven, J. Conformality in Atomic Layer Deposition: Current Status Overview of Analysis and Modelling. *Appl. Phys. Rev.* **2019**, *6*, 021302.

(2) Emslie, D. J. H.; Chadha, P.; Price, J. S. Metal ALD and Pulsed CVD: Fundamental Reactions and Links with Solution Chemistry. *Coord. Chem. Rev.* **2013**, *257*, 3282–3296.

(3) Vidjayacoumar, B.; Emslie, D. J. H.; Clendenning, S. B.; Blackwell, J. M.; Britten, J. F.; Rheingold, A. Investigation of $AlMe_3$, BEt_3, and $ZnEt_2$ as Co-Reagents for Low-Temperature Copper Metal ALD/Pulsed-CVD. *Chem. Mater.* **2010**, *22*, 4844–4853.

(4) Moore, G. E. Cramming More Components Onto Integrated Circuits. *Proc. IEEE* **1998**, *86*, 82–85.

(5) International Roadmap for Devices and Systems; 2018. https://irds.ieee.org (Accessed Feb 5, 2020).

(6) Slater, J. C. Atomic Radii in Crystals. *J. Chem. Phys.* **1964**, *41*, 3199.

(7) Samsung Electronics Announces Second Quarter 2019 Results; 2019. https://news.samsung.com/global/samsung-electronics-announces-second-quarter-2019-results. (Accessed Feb 23, 2020).

(8) Broekhuijsen, N. Samsung Prototypes First Ever 3nm GAAFET Semiconductor. https://www.tomshardware.com/news/samsung-prototypes-first-ever-3nm-gaafet-semiconductor (Accessed Jan 27, 2020).

(9) Kim, J.-M.; Lee, H.-B.-R.; Lansalot, C.; Dussarrat, C.; Gatineau, J.; Kim, H. Plasma-Enhanced Atomic Layer Deposition of Cobalt Using Cyclopentadienyl Isopropyl Acetamidinato-Cobalt as a Precursor. *Jpn. J. Appl. Phys.* **2010**, *49*, 05FA10.

(10) 13 Sextillion & Counting: The Long & Winding Road to the Most Frequently Manufactured Human Artifact in History. https://computerhistory.org/blog/13-sextillion-counting-the-long-winding-road-to-the-most-frequently-manufactured-human-artifact-in-history (Accessed Feb 8, 2020).

(11) Zeghbroeck, B. V. *Principles of Electronic Devices* [Online]; Colorado, 2011. http://ecee.colorado.edu/~bart/book/ (accessed Feb 13, 2020).

(12) Ytterdal, T.; Cheng, Y.; Fjeldly, T. A. *Device Modeling for Analog and RF CMOS Circuit Design.* John Wiley & Sons, Ltd, 2003.

(13) Wilk, G. D.; Wallace, R. M.; Anthony, J. M. High-κ Gate Dielectrics: Current Status and Materials Properties Considerations. *J. Appl. Phys.* **2001**, *89*, 33.

(14) MOSFETs. http://www.rignitc.com/mosfets/ (Accessed Mar 12, 2020).

(15) Mallick, B. C.; Hsieh, C.-T.; Yin, K.-M.; Gandomi, Y. A.; Huang, K.-T. Review—On Atomic Layer Deposition: Current Progress and Future Challenges. *ECS J. Solid State Sci. Technol.* **2019**, *8*, N55–N78.

(16) Hagen, D. J.; Pemble, M. E.; Karppinen, M. Atomic Layer Deposition of Metals: Precursors and Film Growth. *Appl. Phys. Rev.* **2019**, *6*, 041309.

(17) Roule, A.; Amuntencei, M.; Deronzier, E.; Haumesser, P. H.; Da Silva, S.; Avale, X.; Pollet, O.; Baskaran, R.; Passemard, G. Seed Layer Enhancement by Electrochemical Deposition: The Copper Seed Solution for beyond 45nm. *Microelectron. Eng.* **2007**, *84*, 2610–2614.

(18) Rossnagel, S. M.; Sherman, A.; Turner, F. Plasma-Enhanced Atomic Layer Deposition of Ta and Ti for Interconnect Diffusion Barriers. *J. Vac. Sci. Technol. B.* **2000**, *18*, 2016.

(19) Kim, H.; Rossnagel, S. M. Growth Kinetics and Initial Stage Growth during Plasma-Enhanced Ti Atomic Layer Deposition. *J. Vac. Sci. Technol. A.* **2002**, *20*, 802–808.

(20) Barmak, K.; Cabral, C.; Rodbell, K. P.; Harper, J. M. E. On the Use of Alloying Elements for Cu Interconnect Applications. *J. Vac. Sci. Technol. B.* **2006**, *24*, 2485.

(21) Bernal Ramos, K.; Saly, M. J.; Chabal, Y. J. Precursor Design and Reaction Mechanisms for the Atomic Layer Deposition of Metal Films. *Coord. Chem. Rev.* **2013**, *257*, 3271–3281.

(22) Mistry, H.; Behafarid, F.; Reske, R.; Varela, A. S.; Strasser, P.; Cuenya, B. R.; Tuning Catalytic Selectivity at the Mesoscale via Interparticle Interactions. *ACS Catal*. **2016**, 6, 1075–1080.

(23) Dendooven, J.; Ramachandran, R. K.; Solano, E.; Kurttepeli, M.; Geerts, L.; Heremans, G.; Rongé, J.; Minjauw, M. M.; Dobbelaere, T.; Devloo-Casier, K.; Martens, J. A.; Vantomme, A.; Bals, S.; Portale, G.; Coati, A.; Detavernier, C. Independent Tuning of Size and Coverage of Supported Pt Nanoparticles Using Atomic Layer Deposition. *Nat. Commun.* **2017**, *8*, 1074.

(24) Jiang, X.; Huang, H.; Prinz, F. B.; Bent, S. F. Application of Atomic Layer Deposition of Platinum to Solid Oxide Fuel Cells. *Chem. Mater.* **2008**, *20*, 3897–3905.

(25) Senkevich, J. J.; Tang, F.; Rogers, D.; Drotar, J. T.; Jezewski, C.; Lanford, W. A.; Wang, G.-C.; Lu, T.-M. Substrate-Independent Palladium Atomic Layer Deposition. *Chem. Vap. Depos.* **2003**, *9*, 258–264.

(26) Rossnagel, S. M. Thin Film Deposition with Physical Vapor Deposition and Related Technologies. *J. Vac. Sci. Technol. A.* **2003**, *21*, S74–S87.

(27) Gladfelter, W. L. Selective Metallization by Chemical Vapor Deposition. *Chem. Mater.*, **1993**, *5*, 1372–1388.

(28) George, S. M. Atomic Layer Deposition: An Overview. *Chem. Rev.* **2010**, *110*, 111–131.

(29) Jones, A. C.; Hitchman, M. *Chemical Vapour Deposition: Precursors, Processes and Applications* [Online]. RSC Publishing: Cambridge, 2009. https://pubs.rsc.org/en/content/chapter/bk9780854044658-00001/978-0-85404-465–8 (accessed Feb 23, 2020).

(30) Norman, J. A. T.; Muratore, B. A.; Dyer, P. N.; Roberts, D. A.; Hochberg, A. K.; Dubois, L. H. A New Metal-Organic Chemical Vapor Deposition Process for Selective Copper Metallization. *J. Mater. Sci. Eng.* **1993**, *B17*, 87–92.

(31) Gates, S. M. Surface Chemistry in the Chemical Vapour Deposition of Electronic Materials. *Chem. Rev.* **1996**, *96*, 1519–1532.
(32) Puurunen, R. L. Surface Chemistry of Atomic Layer Deposition: A Case Study for the Trimethylaluminum/Water Process. *J. Appl. Phys.* **2005**, *97*, 121301.
(33) Graugnard, E.; Gaillot, D. P.; Dunham, S. N.; Neff, C. W.; Yamashita, T.; Summers, C. J. Photonic Band Tuning in Two-Dimensional Photonic Crystal Slab Waveguides by Atomic Layer Deposition. *Appl. Phys. Lett.* **2006**, *89*, 181108.
(34) Parsons, G. N.; Elam, J. W.; George, S. M.; Haukka, S.; Jeon, H.; (Erwin) Kessels, W. M. M.; Leskelä, M.; Poodt, P.; Ritala, M.; Rossnagel, S. M. History of Atomic Layer Deposition and Its Relationship with the American Vacuum Society. *J. Vac. Sci. Technol. A.* **2013**, *31*, 050818.
(35) Kim, H.; Lee, H.-B.-R.; Maeng, W.-J. Applications of Atomic Layer Deposition to Nanofabrication and Emerging Nanodevices. *Thin Solid Films.* **2009**, *517* (8), 2563–2580.
(36) Profijt, H. B.; Potts, S. E.; Van de Sanden, M. C. M.; Kessels, W. M. M. Plasma-Assisted Atomic Layer Deposition: Basics, Opportunities, and Challenges. *J. Vac. Sci. Technol. A.* **2011**, *29*, 050801.
(37) Leskelä, M.; Ritala, M. Atomic Layer Deposition Chemistry: Recent Developments and Future Challenges. *Angew. Chem. Int. Ed.* **2003**, *42*, 5548–5554.
(38) Groner, M. D.; Fabreguette, F. H.; Elam, J. W.; George, S. M. Low-Temperature Al_2O_3 Atomic Layer Deposition. *Chem. Mater.* **2004**, *16*, 639–645.
(39) Kalutarage, L. C.; Heeg, M. J.; Martin, P. D.; Saly, M. J.; Kuiper, D. S.; Winter, C. H. *Inorg. Chem.* **2013**, *52*, 1182–1184.
(40) Knisley, T. J.; Kalutarage, L. C.; Winter, C. H. Precursors and Chemistry for the Atomic Layer Deposition of Metallic First Row Transition Metal Films. *Coord. Chem. Rev.* **2013**, *257*, 3222–3231.
(41) Haynes, W. M.; Lide, D. R. *Handbook of Chemistry and Physics, 92nd Ed.;* CRC Press: Boca Raton, FL, 2011–2012.
(42) Kalutarage, L. C.; Martin, P. D.; Heeg, M. J.; Winter, C. H. Volatile and Thermally Stable Mid to Late Transition Metal Complexes Containing α-Imino Alkoxide Ligands, a New Strongly Reducing Coreagent, and Thermal Atomic Layer Deposition of Ni, Co, Fe, and Cr Metal Films. *J. Am. Chem. Soc.* **2013**, *135*, 12588–12591.
(43) Values to 1 decimal place can be found in: Pauling, L. *The Nature of the Chemical Bond, Third Ed.;* Cornell University Press, New York, 1960.
(44) Values to 2 decimal places can be found in table 5.6 on pages 188–190 of: Huheey, J. E; Keiter, E. A.; Keiter, R. L. *Inorganic Chemistry: Principles of Structure and Reactivity, Fourth Ed.;* HarperCollins College Publishers, New York, 1993.
(45) Cheon, J.; Rogers, D. M.; Girolami, G. S. Mechanistic Studies of the Thermolysis of Tetraneopentyltitanium(IV). 1. Solution Evidence that Titanium Alkylidenes Activate Saturated Hydrocarbons. *J. Am. Chem. Soc.* **1997**, *119*, 6804–6813.

(46) Ravindranathan, P.; Patil, K. C. Thermal Reactivity of Metal Formate Hydrazinates. *Thermochim. Acta.* **1983**, *71*, 53–57.
(47) Knisley, T. J.; Ariyasena, T. C.; Sajavaara, T.; Saly, M. J.; Winter, C. H. Low Temperature Growth of High Purity, Low Resistivity Copper Films by Atomic Layer Deposition. *Chem. Mater.* **2011**, *23*, 4417–4419.
(48) Vidjayacoumar, B.; Ramalingam, V.; Emslie, D. J. H.; Blackwell, J.M.; Clendening, S.B. Solution Reactivity Studies for Identification of Promising New ALD and Pulsed CVD Reaction Chemistries. *ECS Trans*. **2012**, *50*, 53–66.
(49) Aaltonen, T.; Alen, P.; Ritala, M.; Leskelä, M. Ruthenium Thin Films Grown by Atomic Layer Deposition. *Chem. Vap. Depos.* **2003**, *9*, 45–49.
(50) Hamalainen, J.; Sajavaara, T.; Puukilainen, E.; Ritala, M.; Leskelä, M. Atomic Layer Deposition of Osmium. *Chem. Mater*. **2012**, *24*, 55–60.
(51) Aaltonen, T.; Ritala, M.; Leskela, M. ALD of Rhodium Thin Films from $Rh(acac)_3$ and Oxygen. *Electrochem. Solid-State Lett*. **2005**, *8*, C99–C101.
(52) Christensen, S. T.; Elam, J. W. Atomic Layer Deposition of Ir–Pt Alloy Films. *Chem. Mater.* **2010**, *22*, 2517–2525.
(53) Hamalainen, J.; Kemell, M.; Munnik, F.; Kreissig, U.; Ritala, M.; Leskela, M. Atomic Layer Deposition of Iridium Oxide Thin FIlms from $Ir(acac)_3$ and Ozone. *Chem. Mater*. **2008**, *20*, 2903–2907.
(54) Hamalainen, J.; Munnik, F.; Ritala, M.; Leskela, M. Atomic Layer Deposition of Platinum Oxide and Metallic Platinum Thin Films from $Pt(acac)_2$ and Ozone. *Chem. Mater.* **2008**, *20*, 6840–6846.
(55) Elam, J. W.; Zinovev, A.; Han, C. Y.; Wang, H. H.; Welp, U.; Hryn, J. N.; Pellin, M. J. Atomic Layer Deposition of Palladium Films on Al_2O_3 Surfaces. *Thin Solid Films.* **2006**, *515*, 1664–1673.
(56) Solanki, R. Atomic Layer Deposition of Copper Seed Layers. *Electrochem. Solid-State Lett.* **1999**, *3*, 479.
(57) Lim, B. S.; Rahtu, A.; Gordon, R. G. Atomic Layer Deposition of Transition Metals. *Nat. Mater.* **2003**, *2*, 749–754.
(58) Igumenov, I. K.; Semyannikov, P. P.; Trubin, S. V.; Morozova, N. B.; Gelfond, N. V.; Mischenko, A. V.; Norman, J. A. Approach to Control Deposition of Ultra Thin Films from Metal Organic Precursors: Ru Deposition. *Surf. Coat. Technol*. **2007**, *201*, 9003–9008.
(59) Lim, B. S.; Rahtu, A.; Park, J. S.; Gordon, R. G. Synthesis and Characterization of Volatile, Thermally Stable, Reactive Transition Metal Amidinates *Inorg. Chem.* **2003**, *42*, 7951–7958.
(60) Mártensson, P.; Carisson, J. Atomic Layer Epitaxy of Copper: Growth and Selectivity in the Cu(II)-2,2,6,6-Tetramethyl-3,5-Heptanedionate/H_2 Process. *J. Electrochem. Soc.* **1998**, *145*, 2926–2931.
(61) Thompson, J. S.; Zhang, L.; Wyre, J. P.; Brill, D. J.; Lloyd, K. G. Vapor Phase Deposition of Copper Films with a Cu(I) β-Diketiminate Precursor. *Thin Solid Films.* **2009**, *517*, 2845–2850.

(62) Seghete, D.; Rayner, G. B.; Cavanagh, A. S.; Anderson, V. R.; George, S. M. Molybdenum Atomic Layer Deposition Using MoF_6 and Si_2H_6 as the Reactants. *Chem. Mater.* **2011**, *23*, 1668–1678.

(63) Klaus, J. W.; Ferro, S. J.; George, S. M. Atomic Layer Deposition of Tungsten Using Sequential Surface Chemistry with a Sacrificial Stripping Reaction. *Thin Solid Films.* **2000**, *360*, 145−153.

(64) Kim, S.-H.; Hwang, E.-S.; Kim, B.-M.; Lee, J.-W.; Sun, H.-J.; Hong, T. E.; Kim, J.-K.; Sohn, H.; Kim, J.; Yoon, T.-S. Effects of B_2H_6 Pretreatment on ALD of W Film Using a Sequential Supply of WF_6 and SiH_4. *Electrochem. Solid-State Lett.* **2005**, *8*, C155–C159.

(65) Ludviksson, A.; Nooney, M.; Bruno, R.; Bailey, A.; Kodas, T. T.; Hampden-Smith, M. J. Low-Temperature Thermal CVD of Ti–Al Metal Films Using a Strong Reducing Agent. *Chem. Vap. Depos.* **1998**, *4*, 129–132.

(66) Yutani, A.; Ichinose, K.; Maekawa, K.; Asai, K.; Kojima, M. Novel Contact-Plug Process with Low-Resistance Nucleation Layer Using Diborane-Reduction Tungsten Atomic-Layer-Deposition Method for 32 Nm Complementary Metal–Oxide–Semiconductor Devices and Beyond. *Jpn. J. Appl. Phys.* **2008**, *47*, 2464–2467.

(67) Vidjayacoumar, B.; Emslie, D. J. H.; Blackwell, J. M.; Clendenning, S. B.; Britten, J. F. Solution Reactions of a bis(pyrrolylaldiminate) Copper(II) Complex with Peralkyl Zinc, Aluminum, and Boron Reagents: Investigation of the Pathways Responsible for Copper Metal Deposition. *Chem. Mater.* **2010**, *22*, 4854–4866.

(68) Knisley, T. J.; Ariyasena, T. C.; Sajavaara, T.; Saly, M. J.; Winter, C. H.; Low Temperature Growth of High Purity, Low Resistivity Copper FIlms by Atomic Layer Deposition. *Chem. Mater.* **2011**, *23*, 4417–4419.

(69) Väyrynen, K.; Mizohata, K.; Räisänen, J.; Peeters, D.; Devi, A.; Ritala, M.; Leskelä, M. Low-Temperature Atomic Layer Deposition of Low-Resistivity Copper Thin Films Using $Cu(Dmap)_2$ and Tertiary Butyl Hydrazine. *Chem. Mater.* **2017**, *29*, 6502–6510.

(70) Kwon, J.; Saly, M.; Halls, M. D.; Kanjolia, R. K.; Chabal, Y. J. Substrate Selectivity of (^{t}Bu–Allyl)$Co(CO)_3$ during Thermal Atomic Layer Deposition of Cobalt. *Chem. Mater.* **2012**, *24*, 1025–1030.

(71) German, E. D.; Sheintuch, M. Relationship Between Kinetic and THermodynamic CHaracteristics of Oxygen Dissociative Adsorption on Close-packed Metal Surfaces. *J. Phys. Chem. A.* **2005**, *109*, 7957–7966.

(72) Goldstein, D. N.; George, S. M.; Enhancing the Nucleation of Palladium Atomic Layer Deposition on Al_2O_3 Using Trimethylaluminum to Prevent Surface Poisoning by Reaction Products. *Appl. Phys. Lett.* **2009**, *95*, 143106.

(73) Dai, M.; Kwon, J.; Halls, M. D.; Gordon, R. G.; Chabal, Y. J. Surface and Interface Processes During Atomic Layer Deposition of COpper on Silicon Oxide. *Langmuir*. **2010**, *26*, 3911–3917.

(74) Holland, P. L.; Andersen, R. A.; Bergman, R. G.; Huang, J. K.; Nolan, S. P. Monomeric Cylopentadienylnickel Methoxo and Amido Complexes: Synthesis,

Characterization, Reactivity, and Use for Exploring the Relationship between H–X and M–X Bond Energies. *J. Am. Chem. Soc.* **1997**, *119*, 12800–12814.

(75) Hoskin, A. J.; Stephan, D.W. Early Transition Metal Hydride Complexes: SYnthesis and Reactivity. *Coord. Chem. Rev*. **2002**, *233*, 107–129.

(76) Park, K.-H.; Marshall, W. J. Remarkably Volatile Copper(II) Complexes of *N,N'*-Unsymmetrically Substituted 1,3-Diketimines as Precursors for Cu Metal Deposition via CVD or ALD. *J. Am. Chem. Soc.* **2005**, *127*, 9330–9331.

(77) Blakeney, K. J.; Winter, C. H. Atomic Layer Deposition of Aluminum Metal Films Using a Thermally Stable Aluminum Hydride Reducing Agent. *Chem. Mater*. **2018**, *30*, 1844–1848.

(78) Mäkelä, M.; Hatanpää, T.; Mizohata, K.; Meinander, K.; Niinistö, J.; Räisänen, J.; Ritala, M.; Leskelä, M. Studies on Thermal Atomic Layer Deposition of Silver Thin Films. *Chem. Mater*. **2017**, *29*, 2040–2045.

(79) Lee, B. H.; Hwang, J. K.; Nam, J. W.; Lee, S. U.; Kim, J. T.; Koo, S. M.; Baunemann, A.; Fischer, R. A.; Sung, M. M. Low-temperature Atomic Layer Deposition of Copper Metal Thin Films: Self-limiting Surface Reaction of Copper Dimethylamino-2-propoxide with Diethylzinc. *Angew. Chem. Int. Ed*. **2009**, *48*, 4536–4539.

(80) Rowlette, P.C.; Allen, C. G.; Bromley, O. B.; Dubetz, A. E.; Wolden, C. A. Plasma-Enhanced Atomic Layer Deposition of Semiconductor Grade ZnO Using Dimethyl Zinc. *Chem. Vap. Deposition*, **2009**, *15*, 15–20.

(81) Whitehorne, T. J. J.; Coyle, J. P.; Mahmood, A.; Monillas, W. H.; Yap, G. P. A.; Barry, S. T. Group 11 Amidinates and Guanidinates: Potential Precursors for Vapour Deposition. *Eur. J. Inorg. Chem.* **2011**, *21*, 3240–3247.

(82) Veloso, A.; Chew, S. A.; Higuchi, Y.; Ragnarsson, L.-Å.; Simoen, E.; Schram, T.; Witters, T.; Ammel, A. V.; Dekkers, H.; Tielens, H.; Devriendt, K.; Heylen, N.; Sebaai, F.; Brus, S.; Favia, P.; Geypen, J.; Bender, H.; Phatak, A.; Chen, M. S.; Lu, X.; Ganguli, S.; Lei, Y.; Tang, W.; Fu, X.; Gandikota, S.; Noori, A.; Brand, A.; Yoshida, N.; Thean, A.; Horiguchi, N. Effective Work Function Engineering for Aggressively Scaled Planar and Multi-Gate Fin Field-Effect Transistor-Based Devices with High-*k* Last Replacement Metal Gate Technology. *Jpn. J. Appl. Phys.* **2013**, *52*, 04CA02.

(83) Klesko, J. P.; Thrush, C. M.; Winter, C. H. Thermal Atomic Layer Deposition of Titanium Films Using Titanium Tetrachloride and 2-Methyl-1,4-Bis(Trimethylsilyl)-2,5-Cyclohexadiene or 1,4-Bis(Trimethylsilyl)-1,4-Dihydropyrazine. *Chem. Mater*. **2015**, *27*, 4918–4921.

(84) Saito, T.; Nishiyama, H.; Tanahashi, H.; Kawakita, K.; Tsurugi, H.; Mashima, K. 1,4-Bis(Trimethylsilyl)-1,4-Diaza-2,5-Cyclohexadienes as Strong Salt-Free Reductants for Generating Low-Valent Early Transition Metals with Electron-Donating Ligands. *J. Am. Chem. Soc.* **2014**, *136*, 5161–5170.

(85) McCafferty, E.; Wightman, J. P. An X-Ray Photoelectron Spectroscopy Sputter Profile Study of the Native Air-Formed Oxide Film on Titanium. *Appl. Surf. Sci.* **1999**, *143*, 92–100.

(86) Wagner, C. D.; Riggs, W. M.; Davis, L. E.; Moulder, J. F.; Murlenberg, G. E. *Handbook of X-Ray Photoelectron Spectroscopy;* Perkin-Elmer Corporation: Eden Prairie, MN, 1979.

(87) Kritikos, L.; Zambelis, L.; Papadimitropoulos, G.; Davazoglou, D. Structure and Electrical Properties of Selectively Chemically Vapor Deposited Vanadium Oxide Films from Vanadium Tri-*i*-Propoxy Oxide Vapors. *Surf. Coat. Technol.* **2007**, *201*, 9334–9339.

(88) Granqvist, C. G. Window Coatings for the Future. *Thin Solid Films.* **1990**, *194*, 730–741.

(89) Richardson, M. A.; Coath, J. A. Infrared Optical Modulators for Missile Testing. *Opt. Laser Technol.* **1998**, *30*, 137–140.

(90) Zhu, Z.; Liu, Z.; Liu, S.; Niu, H. A Novel Carbon-Supported Vanadium Oxide Catalyst for NO Reduction with NH_3 at Low Temperatures. *Appl. Catal.* **1999**, *23*, L229–L233.

(91) Biette, L.; Carn, F.; Maugey, M.; Achard, M.-F.; Maquet, J.; Steunou, N.; Livage, J.; Serier, H.; Backov, R. Macroscopic Fibers of Oriented Vanadium Oxide Ribbons and Their Application as Highly Sensitive Alcohol Microsensors. *Adv. Mater.* **2005**, *17*, 2970–2974.

(92) Whittingham, M. S.; Song, Y.; Lutta, S.; Zavalij, P. Y.; Chernova, N. A. Some Transition Metal (Oxy)Phosphates and Vanadium Oxides for Lithium Batteries. *J. Mater. Chem.* **2005**, *15*, 3362.

(93) Field, M. N.; Parkin, I. P. J. Atmospheric pressure chemical vapour deposition of vanadium(V) oxide films on glass substrates from reactions of $VOCl_3$ and VCl_4 with water. *Mater. Chem.* **2000**, *10*, 1863–1866.

(94) Manning, T. D.; Parkin, I. P.; Clark, R. J. H.; Sheel, D.; Pemble, M. E.; Vernadou, D. J. Intelligent Window Coatings: Atmospheric Pressure Chemical Vapour Deposition of Vanadium Oxides. *Mater. Chem.* **2002**, *12*, 2936–2939.

(95) Beardslee, J. A.; Mebust, A. K.; Chaimowitz, A. S.; Davis-VanAtta, C. R.; Leonard, H.; Moersch, T. L.; Afridi, M. Y.; Taylor, C. J. Using Precursor Chemistry to Template Vanadium Oxide for Chemical Sensing. *Chem. Vap. Depos.* **2010**, *16*, 206–210.

(96) Chang, H. L. M.; Gao, Y.; Zhang, T. J.; Lam, D. J. Heteroepitaxy of TiO_2, VO_2 films and TiO_2/VO_2 multilayers grown on sapphire (1120) by metallo-organic chemical vapor deposition. *Thin Solid Films.* **1992**, *216*, 4–7.

(97) Crociani, L.; Carta, G.; Natali, M.; Rigato, V.; Rossetto, G. MOCVD of Vanadium Oxide Films with a Novel Vanadium(III) Precursor. *Chem. Vap. Depos.* **2011**, *17*, 6–8.

(98) Piccirillo, C.; Binions, R.; Parkin, I. P. Synthesis and Functional Properties of Vanadium Oxides: V_2O_3, VO_2, and V_2O_5 Deposited on Glass by Aerosol-Assisted CVD. *Chem. Vap. Depos.* **2007**, *13*, 145–151.

(99) Saeli, M.; Binions, R.; Piccirillo, C.; Parkin, I. P. Templated growth of smart coatings: Hybrid chemical vapour deposition of vanadyl acetylacetonate with tetraoctyl ammonium bromide. *Appl. Surf. Sci.* **2009**, *255*, 7291–7295.

(100) Barreca, D.; Depero, L. E.; Franzato, E. Rizzi, G. A. Sangaletti, L.; Tondello, E. Vettoria, U. J. Vanadyl Precursors Used to Modify the Properties of Vanadium Oxide Thin Films Obtained by Chemical Vapour Deposition. *Electrochem. Soc.* **1999**, *146*, 551–558.

(101) Boscher, N. D.; Blackman, C. S.; Carmalt, C. J.; Parkin, I. P.; Prieto, A. G. Atmospheric Pressure Chemical Vapour Deposition of Vanadium Diselenide Thin Films. *Appl. Surf. Sci.* **2007**, *253*, 6041–6046.

(102) Blanquart, T.; Niinistö, J.; Gavagnin, M.; Longo, V.; Heikkilä, M.; Puukilainen, E.; Pallem, V. R.; Dussarrat, C.; Ritala, M.; Leskelä, M. Atomic Layer Deposition and Characterization of Vanadium Oxide Thin Films. *RSC Adv.* **2013**, *3*, 1179–1185.

(103) Wang, X.; Guo, Z.; Gao, Y.; Wang, J. Atomic Layer Deposition of Vanadium Oxide Thin Films from Tetrakis(Dimethylamino)Vanadium Precursor. *J. Mater. Res.* **2017**, *32*, 37–44.

(104) Weimer, M. S.; Kim, I. S.; Guo, P.; Schaller, R. D.; Martinson, A. B. F.; Hock, A. S. Oxidation State Discrimination in the Atomic Layer Deposition of Vanadium Oxides. *Chem. Mater.* **2017**, *29*, 6238–6244.

(105) Vial, A.; Laroche, T. Description of Dispersion Properties of Metals by Means of the Critical Points Model and Application to the Study of Resonant Structures Using the FDTD Method. *J. Phys. D: Appl. Phys.* **2007**, *40*, 7152.

(106) Rajani, K. V.; Daniels, S.; McNally, P. J.; Olabanji, L. F.; Alam, M. M. Ultrathin Chromium Transparent Metal Contacts by Pulsed DC Magnetron Sputtering. *Phys. Status Solidi A*, **2010**, *207*, 1586.

(107) Hecht, D. S; Hu; Irvin, G. Emerging Transparent Electrodes Based on Thin Films of Carbon Nanotubes, Graphene and Metallic Nanostructures. *Adv. Mater.* **2011**, *23*, 1482–1513.

(108) Klauk, H.; Huang, J. R.; Nichols, J. A.; Jackson, T. N. Ion-Beam-Deposited Ultrathin Transparent Metal Contacts. *Thin Solid Films*. **2000**, *366*, 272.

(109) Ghosh, D. S.; Martinez, L.; Giurgola, S.; Vergani, P.; Pruneri, V. Widely Transparent Electrodes Based on Ultrathin Metals. *Opt. Lett.* **2009**, *34*, 325-327.

(110) Grubbs, R. K.; Steinmetz, N. J.; George, S. M. Gas Phase Reaction Products During Tungsten Atomic Layer Deposition Using WF_6 and Si_2H_6. *J. Vac. Sci. Technol. B.* **2004**, *22*, 1811-1821.

(111) Fabreguette, F. H.; Sechrist, Z. A.; Elam, J. W.; George, S. M. Quartz Crystal Microbalance Study of Tungsten Atomic Layer Deposition Using WF_6 and Si_2H_6. *Thin Solid Films*. **2005**, *488*, 103–110.

(112) Wind, R. W.; Fabreguette, F. H.; Sechrist, Z. A.; George, S. M. Nucleation Period, Surface Roughness, and Oscillations in Mass Gain Per Cycle During W Atomic Layer Deposition on Al_2O_3. *J. Appl. Phys.* **2009**, *105*, 074309.

(113) Elam, J. W.; Nelson, C. E.; Grubbs, R. K.; George, S. M. Kinetics of the WF_6 and Si_2H_6 Surface Reactions During Tungsten Atomic Layer Deposition. *Surf. Sci.* **2001**, *479*, 121.

(114) Callister, W. D. *Materials Science and Engineering: An Introduction*; Wiley, 1997.

(115) Choudhary, V. R.; Rajput, A. M.; Prabhakar, B. NiO/CaO-Catalyzed Formation of Syngas by Coupled Exothermic Oxidative Conversion and Endothermic CO_2 and Steam Reforming of Methane. *Angew. Chem. Int. Ed.* **1994**, *33*, 2104.
(116) Koike, J.; Wada, M. Self-forming Diffusion Barrier Layer in Cu-Mn Alloy Metallization. *Appl. Phys. Lett.* **2005**, *87*, 041911.
(117) Du, L.; Yu, S.; Liu, X.; Ding, Y. An Aminopyridinato Mn(II) Compound as a Novel CVD Precursor for Manganese-Containing Films, *New J. Chem.* **2018**, *42*, 45534558.
(118) Au, Y.; Lin, Y.; Kim, H.; Beh, E.; Liu, Y.; Gordon, R. G. Selective Chemical Vapor Deposition of Manganese Self-Aligned Capping Layer for Cu Interconnections in Microelectronics. *Electrochem. Soc.* **2010**, *157*, D341–D345.
(119) Kurokawa, A.; Sutou, Y.; Koike, J.; Hamada, T.; Matsumoto, K.; Nagai, H.; Maekawa, K.; Kanato, H. Simultaneous Formation of a Metallic Mn Layer and a MnOx/MnSixOy Barrier Layer by Chemical Vapor Deposition at 250 °C. *Jpn. J. Appl. Phys.* **2013**, *52*, 05FA02/01–05FA02/03.
(120) Neishi, K.; Aki, S.; Matsumoto, K.; Sato, H.; Itoh, H.; Hosaka, S.; Koike, J. Formation of a Manganese Oxide Barrier Layer with Thermal Chemical Vapor Deposition for Advanced Large-Scale Integrated Interconnect Structure. *Appl. Phys. Lett.* **2008**, *93*, 032106/032101–032106/032103.
(121) Sun, H.; Zaera, F. Chemical Vapor Deposition of Manganese Metallic Films on Silicon Oxide Substrates. *J. Phys. Chem. C.* **2012**, *116*, 23585–23595.
(122) Nilsen, O.; Fjellvåg, H.; Kjekshus, A. Growth of Manganese Oxide Thin Films by Atomic Layer Deposition. *Thin Solid Films.* **2003**, *444*, 44–51.
(123) Kalutarage, L. C.; Clendenning, S. B.; Winter, C. H. Manganese Precursor Selection and the Thermal Atomic Layer Deposition of Copper/Manganese Alloy Films. *ECS Trans*. **2014**, *64*, 147–157.
(124) Qin, X.; Zaera, F. Oxidizing versus Reducing Co-Reactants in Manganese Atomic Layer Deposition (ALD) on Silicon Oxide Surfaces. *ECS J. Solid State SC.* **2014**, *3*, Q89–Q94.
(125) Lima, L. P. B.; Dekkers, H. F. W.; Lisoni, J. G.; Diniz, J. A.; Van Elshocht, S.; De Gendt, S. Metal Gate Work Function Tuning by Al Incorporation in TiN. *J. Appl. Phys*. **2014**, *115*, 074504.
(126) Adams, D. P. Reactive Multilayers Fabricated by Vapor Deposition: A Critical Review. *Thin Solid Films.* **2015**, *576*, 98–128.
(127) Seayad, A. M.; Antonelli, D. M. Recent Advances in Hydrogen Storage in Metal-Containing Inorganic Nanostructures and Related Materials. *Adv. Mater.* **2004**, *16*, 765−777.
(128) Chan, G. H.; Zhao, J.; Schatz, G. C.; Van Duyne, R. P. Localized Surface Plasmon Resonance Spectroscopy of Triangular Aluminum Nanoparticles. *J. Phys. Chem. C.* **2008**, *112*, 13958−13963.
(129) Rumble, J. *CRC Handbook of Chemistry and Physics, 98th Ed.;* CRC Press/Taylor & Francis: Boca Raton, FL, 2018.

(130) Gladfelter, W. L.; Boyd, D. C.; Jensen, K. F. Trimethylamine Complexes of Alane as Precursors for the Low-Pressure Chemical Vapor Deposition of Aluminum. *Chem. Mater.* **1989**, *1*, 339–343.
(131) Lee, Y. J.; Kang, S.-W. Atomic Layer Deposition of Aluminum Thin Films Using an Alternation Supply of Trimethylaluminum and a Hydrogen Plasma. *Electrochem. Solid-State Lett*. **2002**, *5*, C91−C93.
(132) Spessard, G. O.; Miessler, G. L. *Organometallic Chemistry*, 2nd ed.; Oxford University Press: New York, 2010.
(133) Calderazzo, F. *Synthesis and Properties of Transition Metal to Carbon Bonds*, Plenary Lecture Presented at the XIVth International Conference on Coordination Chemistry, Toronto, Canada, **1972**, 453–474.
(134) Mowat, W.; Shortland, A.; Yagupsky, G.; Hill, N. J.; Yagupsky, M.; Wilkinson, G. Elimination Stabilized Alkyls. Part I. Chromium, Molybdenum, Tungsten, and Vanadium. *J. Chem. Soc. Dalton Trans.* **1972**, *4*, 533.
(135) Davidson, P. J.; Lappert, M. F.; Pearce, R. Stable Homoleptic Metal Alkyls. *Acc. Chem. Res.* **1974**, *7*, 209–217.
(136) Shortland, A. J.; Wilkinson, G. Preparation and Properties of Hexamethyltungsten. *J. Chem. Soc. Dalton Trans.* **1973**, 872–876.
(137) Collier, M. R.; Lappert, M. F.; Pearce, R. Silylmethyl and Related Complex. Part 1. Kinetically Stable Alkyls of Titanium(IV), Zirconium(IV), and Halfnium(IV). *J. Chem. Soc. Dalton Trans.* **1973**, 445–451.
(138) Barker, G. K.; Lappert, M. F. Stabilisation of Transition Metals in a Low Coordinate Environment using the Bis(trimethylsilyl)methyl Ligand; a Monomeric Cr^{III} Alkyl, $Cr[CH(SiMe_3)_2]_3$, and Related Complexes. *J. Organomet. Chem.* **1974**, *76*, C45–C46.
(139) Jarvis, J. A. J.; Pearce, R.; Lappert, M. F. Silylmethyl and Related Complexes. Part 4. l Preparation, Properties, and Crystal and Molecular Structure of Tetrakis[(Trimethylsilylmethyl)-Copper(i)], an Alkyl-Bridged, Square-Planar, Tetranuclear Copper(I) Cluster. *J. Chem. Soc. Dalton Trans.* **1977**, 999–1003.
(140) Schulzke, C.; Enright, D.; Sugiyama, H.; LeBlanc, G.; Gambarotta, S.; Yap, G. P. A.; Thompson, L. K.; Wilson, D. R.; Duchateau, R. The Unusual Stability of Homoleptic Di- and Tetravalent Chromium Alkyls. *Organometallics* **2002**, *21*, 3810–3816.
(141) Hong, T. E.; Choi, S.-K.; Kim, S.-H.; Cheon, T. Growth of Highly Conformal TiC_x Films Using Atomic Layer Deposition Technique. *J. Am. Ceram. Soc.* **2013**, *96*, 1060–1062.
(142) Cheon, J.; Rogers, D. M.; Girolami, G. S. Mechanistic Studies of the Thermolysis of Tetraneopentyltitanium(IV). 1. Solution Evidence That Titanium Alkylidenes Activate Saturated Hydrocarbons. *J. Am. Chem. Soc.* **1997**, *119*, 6804–6813.
(143) Kim, T.-H.; Eom, T.-K.; Kim, S.-H.; Kang, D.-H.; Kim, H.; Yu, S.; Lim, J. M. Plasma-Enhanced Atomic Layer Deposition of TaCx Films Using Tris(Neopentyl) Tantalum Dichloride and H_2 Plasma. *Electrochem. Solid-State Lett.* **2011**, *14*, D89.

(144) Hong, T. E.; Kim, T.-H.; Jung, J.-H.; Kim, S.-H.; Kim, H. TaC_x Thin Films Prepared by Atomic Layer Deposition as Diffusion Barriers for Cu Metallization. *J. Am. Ceram. Soc.* **2014**, *97*, 127–134.

(145) Griffiths, M. B. E.; Pallister, P. J.; Mandia, D. J.; Barry, S. T. Atomic Layer Deposition of Gold Metal. *Chem. Mater.* **2016**, *28*, 44–46.

(146) Mäkelä, M.; Hatanpää, T.; Mizohata, K.; Räisänen, J.; Ritala, M.; Leskelä, M. Thermal Atomic Layer Deposition of Continuous and Highly Conducting Gold Thin Films. *Chem. Mater.* **2017**, *29*, 6130–6136.

(147) Price, J. S.; Chadha, P.; Emslie, D. J. H. Base-Free and Bisphosphine Ligand Dialkylmanganese(II) Complexes as Precursors for Manganese Metal Deposition. *Organometallics.* **2016**, *35*, 168–180.

(148) Gas Molecules and Gas Flow. https://vacaero.com/information-resources/vacuum-pump-technology-education-and-training/9364-gas-molecules-and-gas-flow.html (accessed May 3, 2020).

(149) Mowat, W.; Shortland, A. J.; Hill, N. J.; Wilkinson, G. Elimination Stabilized Alkyls. Part II. Neopentyl and Related Alkyls of Chromium(IV). *J. Chem. Soc. Dalton Trans.* **1973**, 770–778.

(150) Andersen, R. A.; Wilkinson, G.; Lappert, M. F.; Pearce, R. *Bis[(Trimethylsilyl)Methyl] Magnesium*. Inorganic Syntheses; Shriver, D. F., Ed.; John Wiley & Sons, Inc.: Hoboken, NJ, USA, 2007; pp 262–265.

(151) Edwards, P. G.; Wilkinson, G.; Motevalli, M.; Malik, K. M. A.; Hursthouse, M. B. Oxoalkyls of Rhenium-(V) and-(VI). X-Ray Crystal Structures of $(Me_4ReO)_2Mg(thf)_4$,$[(Me_3SiCH_2)_4ReO]_2Mg(thf)_2$, $Re_2O_3Me_6$ and $Re_2O_3(CH_2SiMe_3)_6$. *J. Chem. Soc. Dalton Trans.* **1985**, 2167–2175.

(152) Raston, C. L.; Lappert, M. F. Synthesis and X-Ray Crystal Structure of a W^V Metallocycle $[\{W(CH_2C_6H_4CH_2\text{-}o)_2O\}_2Mg(tetrahydrofuran)_4]$. *J.C.S. Chem. Comm.* **1981**, 6–8.

(153) Stavropoulos, P.; Wilkinson, G. Oxo Methyls of Molybdenum(V), Tungsten(V) and Rhenium(V): X-Ray Crystal Structure of $(Me_4WO)_2Mg(thf)_4$. *Polyhedron.* **1987**, *6*, 1081–1087.

(154) Girolami, G. S.; Wilkinson, G.; Galas, A. M. R.; Thornton-Pett, M.; Hursthouse, M. B. Synthesis and Properties of the Divalent 1,2-Bis(dimethy1phosphino)ethane (dmpe) Complexes $MCl_2(dmpe)_2$ and $MMe_2(dmpe)_2$ (M = Ti, V, Cr, Mn, or Fe). X-Ray Crystal Structures of $MCl_2(dmpe)_2$ (M = Ti, V, or Cr), $MnBr_2(dmpe)_2$, $TiMe_{1.3}Cl_{0.7}(dmpe)_2$, and $CrMe_2(dmpe)_2$. *J. Chem. Soc. Dalton Trans.* **1985**, 1339–1348.

(155) Maury, F. Low Temperature Metallorganic Chemical Vapor Deposition Routes to Chromium Metal Thin Films Using Bis(Benzene)Chromium. *J. Electrochem. Soc.* **1999**, *146*, 3716.

(156) Chmely, S. C.; Hanusa, T. P. Complexes with Sterically Bulky Allyl Ligands: Insights into Structure and Bonding. *Eur. J. Inorg. Chem.* **2010**, *2010*, 1321–1337.

(157) Wilke, G.; Bogdanovic, B.; Hardt, P.; Heimbach, P.; Keim, W.; Kroner, M.; Oberkirch, W.; Tanaka, K.; Walter, D. Allyl-Transition Metal Systems. *Angew. Chem. Int. Ed.* **1966**, *5*, 151–164.

(158) Jutzi, P.; Burford, N.; Structurally Diverse π-cyclopentadienyl Complexes of the Main Group Elements. *Chem. Rev.* **1999**, *99*, 969–990.

(159) Hanusa, T. P. New Developments in the Cyclopentadienyl Chemistry of the Alkaline-Earth Metals. *Organometallics*. **2002**, *21*, 2559–2571.

(160) Fraenkel, G.; Chow, A.; Winchester, W. R. Dynamics of Solvated Lithium(+) Within exo,exo-[1,3-bis(trimethylsilyl)allyl]lithiun N,N,N',N'-tetramethylethylenediamine Complex. *J. Am. Chem. Soc.* **1990**, *112*, 1382–1386.

(161) Fraenkel, G.; Chow, A.; Winchester, W. R. [1-(Trimethylsilyl)allyl]lithium: Structure in Solution and Rotational barriers. *J. Am. Chem. Soc*. **1990**, *112*, 2582–2585.

(162) Boche, G.; Fraenkel, G.; Cabral, J.; Harms, K.; Van Eikema, N. J. R.; Hommes, J.; Lohrenz, M.; Marsch, P.; Scheleyer, R. J. exo,exo-[1,3-Bis(trimethylsilyl)allyl]lithium-N,N,N',N'-tetramethylethylenediamine Complex: Crystal Structure and Dynamics in Solution. *J. Am. Chem. Soc.* **1992**, *114*, 1562–1565.

(163) Quisenberry, K. T.; Smith, J. D.; Voehler, M.; Stec, D. F.; Hanusa, T. P.; Brennessel, W. W. Trimethylsilylated Allyl Complexes of Nickel. The Stabilized Bis(π-Allyl)Nickel Complex $[\eta^3\text{-1,3-}(SiMe_3)_2C_3H_3]_2Ni$ and its Mono(π-Allyl)NiX (X = Br, I) Derivatives. *J. Am. Chem. Soc.* **2005**, *127*, 4376–4387.

(164) Sudupe, M.; Cano, J. S.; Royo, P.; Herdtweck, E. Studies Related to the Chloro Titanium and Zirconium Complexes with $[\eta^5$-Cyclopentadienyldi(silylamido)] Ligands. *Eur. J. Inorg. Chem.* **2004**, 3074–3083.

(165) Green, M. L.; Ho, M. Y.; Busch, B.; Wilk, G. D.; Sorsch, T.; Conard, T.; Brijs, B.; Vandervorst, W.; Raisanen, P. I.; Muller, D.; Bude, M.; Grazul, J. Nucleation and Growth of Atomic Layer Deposited HfO_2 Gate Dielectric Layers on Chemical Oxide (Si–O–H) and Thermal Oxide (SiO_2 or Si–O–N) Underlayers. *J. Appl. Phys*. **2002**, *92*, 7168.

(166) Nanayakkara, C. E.; Vega, A.; Liu, G.; Dezelah, C. L.; Kanjolia, R. K.; Chabal, Y. J. Role of Initial Precursor Chemisorption on Incubation Delay for Molybdenum Oxide Atomic Layer Deposition. *Chem. Mater.* **2016**, *28*, 8591–8597.

(167) Smith, J. D.; Hanusa, T. P.; Young, V. G. Steric Stabilization of Homoleptic Bis(π-Allyl) Complexes of Chromium(II) and Iron(II). *J. Am. Chem. Soc.* **2001**, *123*, 6455–6456.

(168) Smith, J. D.; Quisenberry, K. T.; Hanusa, T. P.; Brennessel, W. W. Bis[1,3-Bis(Trimethylsilyl)Allyl]Cobalt(II), a Stable Electron-Deficient Allyl Complex. *Acta Crystallogr. C.* **2004**, *60*, m507–m508.

(169) Sun, H.; Fu, S.; Chen, C.; Wang, Z.; Singh, C. V. Kinetics of Annealing-Induced Detwinning in Chemical Vapor Deposited Nickel. *Acta Mater.* **2019**, *178*, 263–274.

(170) Hieber, W.; Wagner, G. Zur Kenntnis Des Mangancarbonyls, *Z. Naturforsch*. **1957**, *12b*, 478–479.
(171) Booth, B. L.; Haszeldine, R. N. Metal Carbonyl Chemistry. Part 1. Reactions of Phosphorus-Containing Ligands with Hydridopentacarbonylmanganese. *Inorg. Phys. Theoret.* **1966**, 157–160.
(172) Weiler, G.; Huttner, G.; Zsolnai, L.; Berke, H. Phosphordonor-Substituierte Formylmangan-Komplexe, *Z. Naturforsch. B* **1987**, *42*, 203–209.
(173) Laing, M.; Singleton, E.; Kruger, G. Crystal and Molecular Structure of *trans*-bis(diphenylmethylphosphine)tricarbonylmanganese Hydride. *J. Organomet. Chem*. **1973**, *54*, C30–C32.
(174) Hayakawa, H.; Nakayama, H.; Kobayashi, A.; Sasaki, Y. Molecular and Crystal Structure of Hydrido(tricarbonyl)-bis(triphenylphosphine)manganese(I), $HMn(CO)_3[P(C_6H_5)_3]_2$, *Bull. Chem. Soc. Jpn.* **1978**, *51*, 2041-2045.
(175) Rausch, M. D.; Ogasa, M.; Ayers, M. A.; Rogers, R. D.; Rollins, A. N. Formation and Molecular Structure of Hydridotricarbonyl{[η5-(diphenylphosphino)cyclopentadienyl][η7-(diphenylphosphino)cycloheptatrienyl]titanium-P,P'}manganese: A New Chelated Titanium–Manganese Heterobimetallic Compound. *Organometallics* **1991**, *10*, 2481–2484.
(176) Welch, K. D.; Dougherty, W. G.; Kassel, W. S.; DuBois, D. L.; Bullock, R. M. Synthesis, Structures, and Reactions of Manganese Complexes Containing Diphosphine Ligands with Pendant Amines. *Organometallics.* **2010**, *29*, 4532–4540.
(177) Hulley, E. B.; Helm, M. L.; Bullock, R. M. Heterolytic Cleavage of H_2 by Bifunctional Manganese(I) Complexes: Impact of Ligand Dynamics, Electrophilicity, and Base Positioning. *Chem. Sci*. **2014**, *5*, 4729–4741.
(178) Marks, T. J.; Kolb, J. R. Covalent Transition Metal, Lanthanide, and Actinide Tetrahydroborate Complexes. *Chem. Rev*. **1977**, *77*, 263–293.
(179) Hartwig, J. F.; De Gala, S. R. A Continuum Resulting from Equilibrium between Two Structural Extremes in Tungstenocene and Niobocene Boryl and Hydridoborate Complexes. π-Bonding in a d2 Boryl System and the First d0 Boryl Complex. *J. Am. Chem. Soc*. **1994**, *116*, 3661–3662.
(180) Liu, X.-Y.; Bouherour, S.; Jacobsen, H.; Schmalle, H. W.; Berke, H. The Interaction of Lewis Acidic Boron Derivatives with $Re(CO)_5$–$NH(PMe_3)_n$ Complexes. *Inorg. Chim. Acta.* **2002**, *330*, 250267.
(181) Rossin, A.; Peruzzini, M.; Zanobini, F. Nickel(II) Hydride and Fluoride Pincer Complexes and Their Reactivity with Lewis Acids BX_3·L (X = H, L = Thf; X = F, L = Et_2O). *Dalton Trans.* **2011**, *40*, 4447–4452.
(182) Lantero, D. R.; Motry, D. H.; Ward, D. L.; Smith, M. R., III Synthesis of Endo-$Cp_2TaH_2(BO_2C_6H_4)$ and Exo-$Cp_2TaH_2(BO_2C_6H_4)$: Regioisomers of the First Tantalum Boryl Complexes. *J. Am. Chem. Soc*. **1994**, *116*, 10811–10812.
(183) Arnold, N.; Mozo, S.; Paul, U.; Radius, U.; Braunschweig, H. Aryldihydroborane Coordination to Iridium and Osmium Hydrido Complexes. *Organometallics*. **2015**, *34*, 5709–5715.

(184) D. Liu, K.-C. Lam and Z. Lin, J. Density Functional Theory Studies on Structural Isomers and Bonding of Catecholborane Adducts of Group 5 Metallocene (Nb, Ta) Hydride Complexes. *Organomet. Chem.* **2003**, *680*, 148–154.

(185) Besora, M.; Lledos, A. *Contemporary Metal Boron Chemistry I, Ed*. T. B. Marder and Z. Lin, Springer, Berlin, 2008, pp.149–202.

(186) Agnew, D. W.; Moore, C. E.; Rheingold, A.; Figueroa, J. S. Controlled Cis Labilization of CO from Manganese(I) Mixed Carbonyl/Isocyanide Complexes: An Entry Point to Coordinatively Unsaturated Metallo-Lewis Acids. *Organometallics.* **2017**, *36*, 363–371.

(187) Carreño, R.; Riera, V.; Ruiz, M. A.; Jeannin, Y.; PhilocheLevisalles, M. Reactivity of the Unsaturated Dihydrides [$Mn_2(MH)_2(CO)_6(\mu\text{-}L_2)$] towards Boron, Silicon, and Tin Hydrides [L2 = $Ph_2PCH_2PPh_2$, $(EtO)_2POP(OEt)_2$)]. X-Ray Crystal Structures of [$Mn_2(\mu\text{-}H)(\mu\text{-}BH_4)(CO)_6(\mu\text{-}Ph_2PCH_2PPh_2)$] and [$Mn_2(MSnPh_2)_2(CO)_6[\mu\text{-}(EtO)]_2POP(OEt)_2$]. *J. Chem. Soc. Chem. Commun*. **1990**, 15–17.

(188) Girolami, G. S.; Wilkinson, G.; Thornton-Pett, M.; Hursthouse, M. B. Hydrido, Alkyl, and Ethylene 1,2-Bis(dimethylphosphino)Ethane Complexes of Manganese and the Crystal Structures of $MnBr_2(dmpe)_2$, $[Mn(AlH_4)(dmpe)_2]_2$ and $MnMe_2(dmpe)_2$. *J. Am. Chem. Soc*. **1983**, *105*, 6752–6753.

(189) Perthuisot, C.; Fan, M.; Jones, W. D. Catalytic Thermal Carbon-Hydrogen Activation with Manganese Complexes: Evidence for $\eta^2\text{-}H_2$ Coordination in a Neutral Manganese Complex and its Role in Carbon-Hydrogen Activation. *Organometallics.* **1992**, *11*, 3622–3629.

(190) Price, J. S.; Emslie, D. J. H.; Vargas-Baca, I.; Britten, J. F. [$(dmpe)_2MnH(C_2H_4)$] as a Source of a Low-Coordinate Ethyl Manganese(I) Species: Reactions with Primary Silanes, H_2, and Isonitriles. *Organometallics.* **2018**, *37*, 3010–3023.

(191) Price, J. S.; Emslie, D. J. H.; Britten, J. F. Manganese Silylene Hydride Complexes: Synthesis and Reactivity with Ethylene to Afford Silene Hydride Complexes. *Angew. Chem. Int. Ed*. **2017**, *56*, 6223–6227.

(192) Matkovich, V. I. *Boron and Refractory Borides Ed.*; Spring-Verlag: New York, 1977.

(193) Murata, Y.; Miccioli, B. R. Inhibition of Grain Growth in Niobium Diboride. *Amer. Ceram. Soc. Bull*. **1971**, *50*, 182–184.

(194) James, B. D.; Smith, B. E. Convenient, High-yield Syntheses of Bis(tetrahydroborato)bis(cyclopentadienyl)zirconium and Tetrakis(tetrahydroborato)zirconium(IV) *Synth. React. Inorg. Metal-Org. Chem.* **1974**, *4*, 461–465.

(195) Burger, B. J.; J., E. B. Vacuum Line Techniques for Handling Air-Sensitive Organometallic Compounds. In Experimental Organometallic Chemistry – A Practicum in Synthesis and Characterization. *J. Am. Chem. Soc.* **1987**, *357*, 79–98.

(196) Indirect Referencing. https://www.cif.iastate.edu/nmr/nmr-tutorials/indirectref. (Accessed Mar 23, 2019).